



Max-Planck-Institut für Metallforschung
Stuttgart

High-temperature spreading kinetics of metals

Nicole Rauch

Dissertation
an der
Universität Stuttgart

Bericht Nr. 167
Mai 2005

High-temperature spreading kinetics of metals

Von der Fakultät Chemie der Universität Stuttgart
zur Erlangung der Würde eines
Doktors der Naturwissenschaften (Dr. rer. nat.)
genehmigte Abhandlung

vorgelegt von
Nicole Rauch
aus Saarbrücken

Hauptberichter:	Prof. Dr. Dr. h. c. M. Rühle
Mitberichter:	Prof. Dr. F. Aldinger
Tag der Einreichung:	21.03.2005
Tag der Prüfung:	13.05.2005

Max-Planck-Institut für Metallforschung Stuttgart

2005

Parts of this thesis were published in the following paper:

- N. Rauch, E. Saiz, A.P. Tomsia,
Spreading of liquid Ag and Ag–Mo alloys on molybdenum substrates,
Zeitschrift für Metallkunde, 2003, 94, [3]: 233

Contents

List of Abbreviations	9
Zusammenfassung	11
1 Introduction	15
2 Fundamentals	21
2.1 General aspects of wetting	21
2.1.1 Young's equation	21
2.1.2 Measurements of the contact angle	25
2.1.3 Definition of advancing and receding angle	29
2.1.4 Low-/ high temperature spreading	32
2.2 Theoretical models of low-temperature spreading	33
2.2.1 Molecular kinetic model	33
2.2.2 Fluid flow model	36
2.3 Factors affecting the wetting process	39
2.3.1 Adsorption	39
2.3.2 Ridge formation	41
2.4 Mullins theory of grooving	48
2.4.1 Summary of Mullins theory of grooving	48
2.4.2 Relation between Mullins grooving theory and ridge formation theory	51
3 Literature overview	55

Contents

3.1 Comparison of the molecular kinetic model and the fluid flow model with experiments in low-temperature systems	55
3.2 Comparison of the molecular kinetic model and the fluid flow model with experiments in high-temperature systems	58
3.3 Triple-line ridging in high-temperature wetting systems	61
3.3.1 Pure Metals (Al, Cu, Ni) on Al ₂ O ₃	61
3.3.2 Liquid glasses on metals	62
3.3.3 Liquid metal alloys on ceramics	64
3.4 Wetting behavior of liquid metals on metals for systems with negligible mutual solubility	65
4 Experimental details	67
4.1 Wetting experiments	67
4.1.1 Wetting furnace	67
4.1.2 Parameters of the wetting experiment	69
4.1.3 Recording and analysis of the dynamic contact angle	70
4.2 Investigations of the microstructure	72
4.2.1 Scanning Probe Microscopy (SPM)	72
4.2.2 Scanning Electron Microscopy (SEM)	75
4.2.3 Transmission Electron Microscopy (TEM)	76
4.2.4 Auger Electron Spectroscopy (AES)	77
5 Sample preparation	79
5.1 Sample preparation of the samples used for the wetting experiment	79
5.1.1 Polycrystalline and single crystalline Mo	79
5.2 Properties of the materials used for the wetting experiment	80
5.2.1 Optical emission spectrometry (ICP-OES) investigations	80
5.2.2 Orientated Imaging (OIM) investigations	80
5.3 Sample preparation for microstructure investigations	81

Contents

5.3.1 Scanning Electron Microscopy	81
5.3.2 Transmission Electron Microscopy	83
6 Experimental results	85
6.1 Spreading kinetics	85
6.1.1 Spreading kinetics of liquid Ag on polycrystalline Mo	85
6.1.2 Spreading kinetics of liquid Ag on single-crystalline Mo	91
6.2 Determination of advancing and receding angles	95
6.3 Effect of equilibration on the final contact angle	97
6.4 Grooving experiments of Mo	102
6.5 Investigations of the microstructure	107
6.5.1 Scanning electron microscopy	107
6.5.2 Atomic Force Microscopy	111
6.5.3 Transmission Electron Microscopy	113
6.5.4 Focussed Ion Beam	119
6.5.5 Auger Spectroscopy	120
7 Interpretation and discussion	125
7.1 Spreading kinetics	125
7.2 Effect of roughness on the spreading kinetics	132
7.3 Effect of equilibration on spreading and the final contact angle	132
7.4 Effect of temperature on the final contact angle	134
7.5 Effect of Mo surface orientation on the final angle	138
7.6 Grooving experiments of Mo	139
7.7 Influence of ridge formation on the spreading kinetics	140
7.8 Interfacial characterizations	145
8 Summary	147
9 Appendix	151

Contents

Bibliography	155
Acknowledgement	163
Curriculum Vitae	165

List of Abbreviations

AES	=	Auger Electron Spectroscopy
AFM	=	Atomic Force Microscopy
EDS	=	Energy Dispersive X-ray Spectroscopy
FIB	=	Focus Ion Beam
ICP	=	Inductively Coupled Plasma
SEM	=	Scanning Electron Microscopy
OES	=	Optical Emission Spectrometry
OIM	=	Orientated Imaging Microscopy
SAD	=	Selected Area Diffraction
SPM	=	Scanning Probe Microscopy
STM	=	Scanning Tunneling Microscopy
TEM	=	Transmission Electron Microscopy

Zusammenfassung

Wegen der großen technologischen Bedeutung der Hochtemperaturbenetzung wurden insbesondere zur Benetzung von flüssigen Metallen und Oxiden auf unterschiedlichen Substraten viele experimentelle Untersuchungen durchgeführt. Die Benetzung bei tiefen Temperaturen kann theoretisch gut beschrieben werden, wogegen die Beschreibung von Hochtemperatursystemen sehr kompliziert ist, da die Substrate nicht mehr als unlöslich und starr angesehen werden können. Zusätzlich müssen Adsorptionseffekte und Grenzflächenreaktionen in Betracht gezogen werden. Experimentell stellen Hochtemperaturrexperimente sehr hohe Anforderungen an die Temperaturregelung und die Reinheit der Atmosphäre. Deshalb kommt es häufig zu widersprüchlichen experimentellen Befunden.

In dieser Arbeit wurde die „Drop-transfer Methode“ angewandt. Dabei wird die Flüssigkeit und das Substrat getrennt aufgeheizt und erst nach Erreichen der Temperatur in Kontakt gebracht. Dadurch wird eine isotherme Benetzung erreicht. Es wurde die Benetzungskinetik von flüssigem Silber auf polykristallinem und einkristallinem Mo ((110)- und (100))-Oberflächen) untersucht. Das Ag–Mo System ist ein einfaches eutektisches System ohne intermetallische Phasen, weswegen keine chemischen Reaktionen während des Benetzungsversuches ablaufen. Es stellt somit ein Modellsystem dar.

Ziel der Arbeit war es, die grundlegenden Phänomene, die die Hochtemperaturbenetzung in Metall–Metall Systemen kontrollieren, zu analysieren. Die Benetzungskinetik des Systems Ag–Mo wurde dazu mit Modellvorhersagen zur Tieftemperaturbenetzung verglichen. Die Dynamik in Tieftemperatursystemen wird üblicherweise durch ein hydrodynamisches Modell („Fluid flow model“) oder durch ein mikroskopisches Modell („Molecular kinetic model“) beschrieben. In dieser Arbeit

wurde gezeigt, dass die Benetzung aller verwendeter Molybdänsubstrate bei allen Temperaturen und experimentellen Bedingungen durch das mikroskopische Modell beschrieben werden kann. Im Rahmen des mikroskopischen Modells ist die Kinetik dominiert durch die Reibungsverluste der Dreiphasengrenzlinie bei ihrer Bewegung über die Substratoberfläche. Viskose Reibung innerhalb der Flüssigkeit spielt demnach eine untergeordnete Rolle. Für die freie Aktivierungsenergie wurde in dieser Arbeit ein Wert von $\Delta G \approx 95 - 145 \text{ kJ/mol}$ ermittelt. Dieser stimmt mit Literaturwerten zur Oberflächendiffusion von Silberatomen überein. Daraus folgt, dass die Kinetik in den Experimenten durch die Oberflächendiffusion von Silber auf Molybdän bestimmt wird. Die Kinetik ist unabhängig von der Temperatur, der Orientierung des Substrates und experimenteller Randbedingungen („equilibrated“ / „non-equilibrated“)¹.

Der Benetzungswinkel im Gleichgewicht ist hingegen abhängig von all diesen Faktoren. Unter „equilibrated“ Versuchsbedingungen ist der Endwinkel immer geringer als unter „non-equilibrated“ Bedingungen, unabhängig von Temperatur und Orientierung des Substrats. Es wird angenommen, dass unter den „non-equilibrated“ Bedingungen trotz der reduzierenden Atmosphäre das Sauerstoffadsorbat auf der Molybdänoberfläche nicht vollständig desorbiert wurde.

Der Abfall des Endwinkels mit ansteigender Temperatur im Falle der Benetzung von Ag auf einkristallinem Mo lässt sich durch einen Anstieg der Löslichkeit (Mo in Ag) von 0.3 auf 1.2 at.% mit ansteigender Temperatur (von 970 °C auf 1290 °C) erklären. Durch diesen Anstieg ändert sich die Grenzflächenenergie $\Delta\gamma_{\text{SL}}$ um 40 mN/m. Bei dem polykristallinen Mo-Substrat wurde bei niedrigen Temperaturen (970 °C-1000 °C) ein stärkerer Winkelabfall beobachtet als bei dem einkristallinen Mo-Substrat. Dies ist weder durch die Änderung der Grenzflächenenergie γ_{SL} noch durch eine Änderung der Oberflächenenergie γ_{LV} mit der Temperatur zu erklären. Es wäre jedoch denkbar, daß trotz der reduzierenden Atmosphäre bei Temperaturen um 970 °C der an der polykristallinen Mo Oberfläche adsorbierte Sauerstoff noch nicht vollständig

¹ Bei Versuchen unter „equilibrated“ Bedingungen wurden die Proben für eine Stunde auf Versuchstemperatur gehalten bevor das eigentliche Benetzungsexperiment stattfand, wohingegen unter „non-equilibrated“ Bedingungen sofort nach Erreichen der Versuchstemperatur das Benetzungsexperiment durchgeführt wurde.

desorbiert ist. Dies würde zu einer kleineren Oberflächenenergie γ_{SV} führen und damit auch zu einem höheren Endwinkel.

Der Endwinkel von Ag auf einkristallinem Mo(100) war bei den untersuchten Temperaturen immer kleiner als der auf einkristallinem Mo(110). Die in dieser Arbeit bestimmten Daten besagen, dass die Beziehung $\Delta\gamma_{SL} = \gamma_{SL}^{100} - \gamma_{SL}^{110} > \Delta\gamma_{SV} = \gamma_{SV}^{100} - \gamma_{SV}^{110}$ erfüllt sein muss. Dies bedeutet, dass entweder die Grenzflächenenergie sich stark mit der Orientierung des Substrates ändert, oder dass unter den experimentellen Bedingungen die Oberflächenenergie von Mo(110) größer als diejenige von Mo(100) sein müsste. Es ist aus der Literatur bekannt, dass eine H-Atmosphäre eine Rekonstruktion der Mo Oberfläche verursacht. Dies könnte zu einer geringeren Oberflächenenergie einer rekonstruierten Mo(100) Oberfläche im Vergleich zu einer rekonstruierten Mo(110) führen.

Untersuchungen zur Furchenbildung an polykristallinem Mo unter den gleichen Versuchsbedingungen wie die Benetzungsexperimente wurden durchgeführt, um die Oberflächendiffusivität von Molybdän zu bestimmen. Lokale Diffusionsprozesse an den Grenzflächen zwischen Gas, Flüssigkeit und Festkörper können zu einer Gratbildung auf dem Substrat führen. Es wurde bei einigen Hochtemperatursystemen wie z.B. Glas auf Mo und Al auf Al_2O_3 beobachtet, dass Gratbildung die Benetzungskinetik beeinflusst {Saiz, E., 1998}, {Lopez-Esteban S., 2004}. Für das Ag–Mo-System wurde in dieser Arbeit gezeigt dass unter der Annahme, dass keine Oberflächenstörungen als Keime für eine Gratbildung auf der Molybdänoberfläche vorhanden sind, bei den beobachteten Benetzungsgeschwindigkeiten keine Gratbildung zu erwarten ist. Selbst bei Vorhandensein solcher Keime auf der Molybdänoberfläche müsste der Grat kleiner als 1 nm sein um sich mit den beobachteten Geschwindigkeiten mitzubewegen. Gratbildung beeinflusst daher die Benetzungskinetik nicht. Dies wurde durch REM-, AFM- und TEM-Untersuchungen bestätigt, die zeigten, dass selbst nachdem das Benetzungsexperiment beendet war und sich der Tropfen noch eine weitere Stunde auf dem Substrat befunden hatte, keine Gratbildung beobachtet werden konnte.

Zusammenfassung

1 Introduction

Wetting is a phenomenon which is part of our daily life as, for example, rain drops on a window or ink on a paper. In some cases one wants to achieve a complete wetting as in the case of the spreading ink on a paper or in the case of coating processes. In other cases as, for example, wetting of water on rain-proof clothes should be avoided {Butt, H.J., 2003}.

Dynamic wetting or spreading is when a liquid moves over a solid surface and replaces a gas or liquid which was initially in contact with the solid surface. Two general situations are possible: either the liquid spreads until the angle between the solid surface and the moving liquid front reaches a finite equilibrium contact angle – a situation which is called *partial wetting* – or the liquid displaces the original fluid or gas completely. The latter case is called *complete wetting* and the contact angle is zero. Young {Young, T.,1805} was able to relate, in thermodynamic equilibrium the contact angle to the surface energies of the interfaces at the triple line (solid–liquid–gas(liquid)) and Gibbs expressed this relationship in mathematical form {Gibbs, W., 1878}.

Besides the movement of a liquid drop over a solid surface, wetting also relates to the penetration of a liquid into a porous medium, a liquid advancing in a capillary, a plate being immersed in a liquid or the displacement of a liquid by another one {Johnson, R.E. 1993}.

In general one differentiates between *forced wetting* and *spontaneous wetting*. In forced wetting an externally imposed force causes the solid–liquid interfacial area to increase (beyond the static equilibrium) {Kistler, S.F 1993}. This is common in industrial coating processes where a thin layer of liquid is deposited continuously onto a moving surface. The speed at which the coating can be applied is limited due to the failure of the liquid to displace sufficient air from the substrate. This entrainment of air

can lead to a patchy or uneven deposition. Other examples of forced wetting are enhanced oil recovery or polymer processing as for example with mold filling, composite manufacture etc. Spontaneous wetting is the migration of a liquid over a solid surface or liquid surface towards thermodynamic equilibrium. The driving force is not externally imposed but comes from the capillary forces that aim towards a decrease in the free energy of the system. Examples of spontaneous wetting are sprays, such as insecticidal sprays that wet the waxy surface of plant leaves, the printing of inks on paper or the application of paints.

Besides the difference between forced and spontaneous wetting one also differentiates between *low-temperature* and *high-temperature spreading*. Low-temperature wetting implies that the wetting experiment is performed at $T \ll T_m$, where T_m is the melting point of the substrate. Examples for low-temperature wetting include insecticidal sprays, inks and paints. The dynamic aspects of low-temperature wetting have been extensively studied for the spontaneous and forced case as well as for the complete and partial-wetting case {Blake, T.D. 1993}, {Kistler, S.F 1993}, {De Ruijter, M. 1999}. Theoretical approaches typically assume that the substrate is smooth, homogeneous, inert, and non-deformable. However Shanahan et al. {Shanahan, M., 1988} incorporated also viscoelastic ridging into the theoretical description. For low-temperature systems, dynamic wetting has been analyzed using a hydrodynamic description {Voinov, O.V., 1976}, {Kistler, S.F 1993},{Cox, R.G., 1986},{Tanner, L.H., 1979},{Gennes de, P.G., 1985} and from a molecular point of view {Blake, T.D. 1993}, {Blake, T.D., 1968}. High-temperature wetting occurs if the wetting experiment is performed at $T > 0.5T_m$. Typical examples are welding and brazing. Despite the importance of high-temperature wetting in many manufacturing processes it remains a largely unexplored field, mainly due to the temperature and chemical environmental controls required and the complexity of the experimental procedure. The current theories of the dynamics of low-temperature wetting are not necessarily valid for high-temperature spreading. This is in part due to the inherent complexity of high-temperature systems in which the substrates cannot be described as rigid and insoluble and spreading is usually accompanied by adsorption, triple-line ridging, interdiffusion

or interfacial reactions. Thus in most of the systems of high-temperature spreading the results are ambiguous and even inconsistent and the theoretical analysis lags far behind the progress made for low-temperature systems {Eustathopoulos, N., 1999}.

The objective of this work is to unveil the basic phenomena controlling spontaneous spreading in a model system at high temperatures. Several authors have investigated high-temperature spreading systems as liquid metals or metal alloys on ceramics and glasses on metals {Lopez-Esteban S., 2004}, {Saiz, E., 1998}, {Levi G., 2003}, {Eustathopoulos N., 1998}, {Saiz, E., 2000}. In these systems spreading was influenced by triple line ridging, adsorption effects or interfacial reactions. In order to avoid reaction and interdiffusion processes the simple eutectic metal–metal system, Ag(liquid) – Mo, with very small mutual solubility has been chosen. The phase diagram is shown in Figure 1.1. Previous studies of metal–metal systems with small mutual solubility did not investigate a possible influence of ridge formation on the kinetics {Tomsia, A.P.,1982},{Pique, D., 1981} {Sugita, T., 1970},{Yupko, V.L., 1991}{Yupko, V.L., 1986}. The focus of the present work is the spreading kinetics, the question whether it is influenced by triple line ridging, and how spreading is influenced by temperature, the equilibration state of the system (adsorption effects) and the orientation of the Mo substrate. The observed spreading kinetic is compared with current theories developed for low-temperature spreading such as the molecular kinetic model {Blake, T.D., 1993}, {Blake, T.D., 1968}, {De Ruijter, M. 1999} and the fluid flow model {Voinov, O.V., 1976}, {Kistler, S.F 1993}.

High-temperature spreading experiments are generally performed using a conventional sessile-drop configuration, where a liquid drop is placed on a substrate and observed in cross-sections through a telescope. Using this method it is difficult to separate the basic spreading process from additional effects (such as melting, equilibration with the atmosphere, oxide skin removal, etc.) {Eustathopoulos, N., 1999}, {Loehman, R.E., 1994}. In this work a drop-transfer setup combined with high-speed photography is used to analyze the spontaneous (high-temperature) spreading of a liquid Ag drop on polycrystalline and single-crystalline Mo substrates. In this method the Ag is placed on a sapphire substrate, which it does not wet. The Mo substrate is

lowered from the top until it touches the liquid Ag drop and thus wets the Mo substrate. The drop transfer setup provides a unique opportunity to systematically analyze isothermal spreading and avoid the complications related to melting and equilibration.

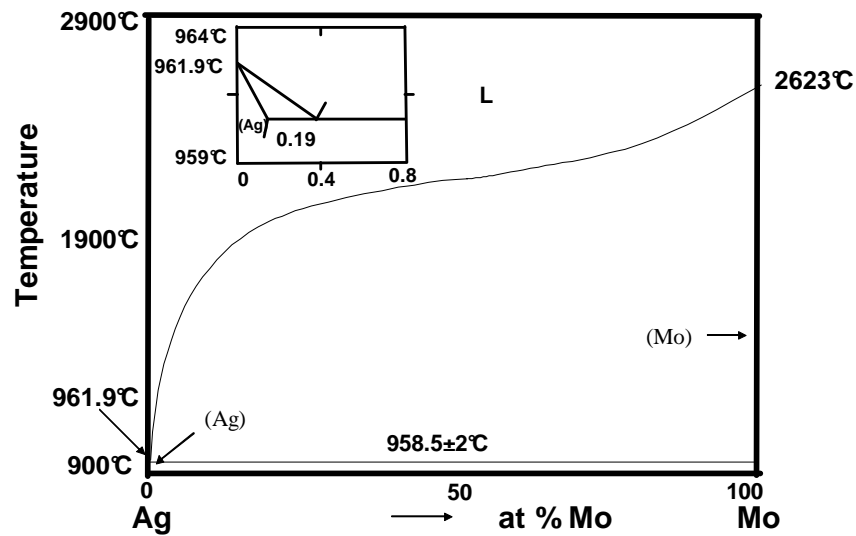


Figure 1.1: Schematic of the Ag-Mo phase diagram after {Massalski, T.B., 1990}. The solubility of Ag in solid Mo is lower than 0.00578 at%

In the next chapter general aspects of wetting are discussed. Two theoretical approaches, based on a molecular kinetic model and a fluid flow model are summarized. Furthermore, two important effects in high temperature systems: ridge formation and adsorption, are discussed in detail. In Chapter 3 a literature survey is given concerning the dynamics of wetting in different low- and high-temperature wetting systems. The experimental details such as the description of the wetting experiment, including the wetting furnace and the parameters of the wetting experiment, as well as the microstructure investigations with Atomic Force Microscopy (AFM), Scanning Electron Microscopy (SEM), Transmission Electron Microscopy (TEM), and Auger Electron Spectroscopy (AES) are reported in Chapter 4. Detailed technical descriptions of the sample preparation for the wetting experiment and of the microstructure investigations

are given in Chapter 5. In Chapter 6 the experimental results of the spreading kinetics of liquid Ag on polycrystalline and single-crystalline Mo substrates are presented. In addition the influence of equilibration, Mo orientation and ridge formation on the spreading kinetics and the final equilibrium contact angle is reported. Finally, the results are discussed in Chapter 7. A short summary is given in Chapter 8.

1 Introduction

2 Fundamentals

2.1 General aspects of wetting

In the present work the spontaneous spreading of a liquid drop over a solid surface is investigated. The liquid moves across a solid surface and displaces the gas which was originally in contact with the solid surface. The movement of the liquid stops if either the liquid reaches a finite equilibrium contact angle with the substrate or if it displaces the original liquid or gas completely. In the latter case, the contact angle is equal to zero which corresponds to complete wetting in contrast to partial wetting which is described by a finite contact angle.

Since wetting depends on the surface properties of a solid and its interactions with the liquid the investigation of wetting allows characterization of surfaces and the interaction of solids with liquids.

This chapter gives an overview of the parameters which characterize wetting and their derivation. In addition, the difference between low- and high-temperature spreading is discussed.

2.1.1 Young's equation

A fundamental parameter characterizing wetting is the equilibrium contact angle. The contact angle represents a macroscopic quantity defined as the angle between the substrate/liquid interface and the tangent to the droplet at the solid/liquid/vapor junction (Figure 2.1). Complete wetting occurs if $\theta_0 = 0^\circ$, $0^\circ < \theta_0 < 180^\circ$ implies partial wetting.

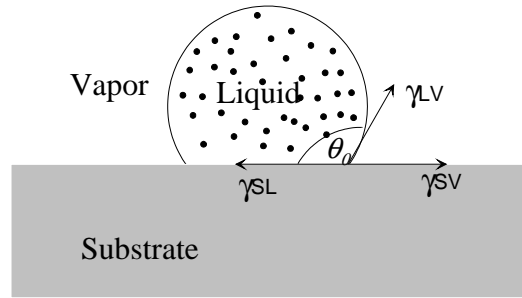


Figure 2.1: Schematic drawing of a liquid drop on a solid substrate. θ_0 is the Young's equilibrium angle; γ_{SV} , γ_{SL} , and γ_{LV} are the equilibrium solid/vapor, solid/liquid and liquid/vapor interfacial energies.

Equilibrium can be described by Young's equation (2.1b), which is the result of balancing the horizontal force components at the three-phase line:

$$\gamma_{SV} = \gamma_{SL} + \gamma_{LV} \cos \theta_0 \quad (2.1a)$$

$$\text{and thus: } \cos \theta_0 = (\gamma_{SV} - \gamma_{SL}) / \gamma_{LV}, \quad (2.1b)$$

where γ_{SV} , γ_{SL} , and γ_{LV} are the equilibrium solid/vapor, solid/liquid, and liquid/vapor interfacial energies per unit area, respectively. The term $\gamma_{SV} - \gamma_{SL}$ in Young's equation (2.1.b) is sometimes called the wetting driving force. Young's equation is only valid when the substrate is flat, homogenous, inert, and non-deformable. In the following a brief derivation of the Young's equation is given using a circular drop on a planar solid surface and assuming that the drop has the shape of a spherical cap. The derivation is done for the two-dimensional case; a three-dimensional calculation leads to equivalent results. Since the mass of the drop is small, gravitation can be neglected.

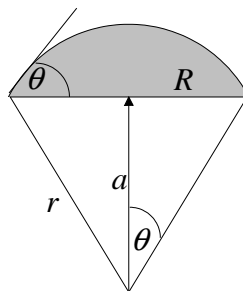


Figure 2.2: A drop with the shape of a spherical segment is shown. θ is the contact angle, R represents the base radius of the drop at the solid-liquid interface.

2 Fundamentals

The area (A_{segment}) of a spherical segment is

$$A_{\text{segment}} = \theta r^2 - Ra \quad (2.2)$$

Given $\sin \theta = \frac{R}{r}$ and $a = R \cot \theta$ (see Figure 2.2) the area A_{segment} is

$$A_{\text{segment}} = R^2 \left(\frac{\theta}{\sin^2 \theta} - \cot \theta \right) \Rightarrow R = \frac{\sin \theta}{\sqrt{A_{\text{segment}} (\theta - \sin \theta \cos \theta)}} \quad (2.3)$$

Since the liquid is incompressible and the mass of the liquid stays constant, the area (A_{segment}) of the spherical segment is constant:

$$A_{\text{segment}} = \text{const.} \quad (2.4)$$

In equilibrium, the total energy E_{tot} of the system has its minimum. The total energy is the sum of the product of γ_{SL} (solid-liquid), γ_{SV} (solid-vapor) and γ_{LV} (liquid-vapor) and the respective interface lines L :

$$E_{\text{tot}} = \gamma_{LV} L_{LV} + \gamma_{SV} L_{SV} + \gamma_{SL} L_{SL} \quad (2.5)$$

With S as the length of the substrate

$$E_{\text{tot}} = \gamma_{LV} \frac{2\theta R}{\sin \theta} + \gamma_{SV} (S - 2R) + \gamma_{SL} 2R \quad (2.6)$$

In equilibrium

$$\left. \frac{\partial}{\partial \theta} E_{\text{tot}} (R(\theta), \theta) \right|_{\theta=\theta_0} = 0 \quad (2.7)$$

$$\frac{\partial}{\partial \theta} E_{\text{tot}} = \left[\gamma_{LV} \frac{\partial}{\partial \theta} \left(\frac{\theta}{\sqrt{\theta - \cos \theta \sin \theta}} \right) + (\gamma_{SL} - \gamma_{SV}) \frac{\partial}{\partial \theta} \left(\frac{\sin \theta}{\sqrt{\theta - \cos \theta \sin \theta}} \right) \right]_{\theta=\theta_0} = 0 \quad (2.8)$$

$$\text{with } f(\theta) = \sqrt{\theta - \cos \theta \sin \theta} \quad (2.9)$$

Equation (2.8) transforms to

$$\begin{aligned} \frac{\partial}{\partial \theta} E_{\text{tot}} &= \left[\gamma_{LV} \frac{\partial}{\partial \theta} \left(\frac{\theta}{f(\theta)} \right) + (\gamma_{SL} - \gamma_{SV}) \frac{\partial}{\partial \theta} \left(\frac{\sin \theta}{f(\theta)} \right) \right]_{\theta=\theta_0} = 0 \quad (2.10) \\ &= \left[\gamma_{LV} \left(\frac{1}{f(\theta)} + \theta \frac{\partial}{\partial \theta} \frac{1}{f(\theta)} \right) + (\gamma_{SL} - \gamma_{SV}) \left(\frac{\cos \theta}{f(\theta)} + \sin \theta \frac{\partial}{\partial \theta} \frac{1}{f(\theta)} \right) \right]_{\theta=\theta_0} = 0 \end{aligned}$$

$$\text{with } \frac{\partial}{\partial \theta} \frac{1}{f(\theta)} = -\frac{1}{f^2(\theta)} \frac{\partial}{\partial \theta} f(\theta) \quad (2.11).$$

Equation (2.10) leads to

$$\left[\gamma_{LV} \left(f(\theta) - \theta \frac{\partial}{\partial \theta} f(\theta) \right) + (\gamma_{SL} - \gamma_{SV}) \left(\cos \theta f(\theta) - \sin \theta \frac{\partial}{\partial \theta} f(\theta) \right) \right]_{\theta=\theta_0} = 0 \quad (2.12)$$

$$\text{and } \frac{\partial}{\partial \theta} f(\theta) = \frac{1}{2} \left(\frac{1 - \cos^2 \theta + \sin^2 \theta}{f(\theta)} \right) \quad (2.13).$$

Equation (2.12) is transformed to

$$\left[\gamma_{LV} [f^2(\theta) - \theta \sin^2(\theta)] + (\gamma_{SL} - \gamma_{SV}) [\cos \theta f^2(\theta) - \sin^3 \theta] \right]_{\theta=\theta_0} = 0 \quad (2.14).$$

$$\text{With } \sin^2 \theta + \cos^2 \theta = 1 \quad (2.15)$$

$$\text{and } \theta \cos \theta - \sin \theta \neq 0 \quad (2.16)$$

equation (2.14) becomes the Young's equation

$$\cos \theta_0 = (\gamma_{SV} - \gamma_{SL}) / \gamma_{LV}. \quad (2.17).$$

Even though the previous derivation was done for a small drop on a substrate, the Young's equation (2.17) is also valid for other wetting situations such as a liquid advancing in a capillary or a plate being immersed into a liquid.

The Young's angle is a macroscopic quantity. In the vicinity of the wetting line, which is named "core region", forces such as van-der-Waals forces or electrostatic forces can change the shape of the drop {de Gennes, P.D. 1985}. These forces affect the shape of the triple line of the drop in a range between 1 and 100 nm. They can be responsible for the difference observed between microscopic and macroscopic contact angles {Borchard-Wyart, F., 1991}, {Yeh, E.K., 1999}, {Butt, HJ., 2003}. If the liquid is attracted by the solid surface (van der Waals, or electrostatic forces) and this attraction is stronger than the attraction among the liquid molecules the core region will extend (Figure 2.3A). On the other hand, if the attraction of the molecules in the liquid is stronger than their attraction to the solid, the core region will shrink (Figure 2.3B) {Butt, HJ., 2003}.

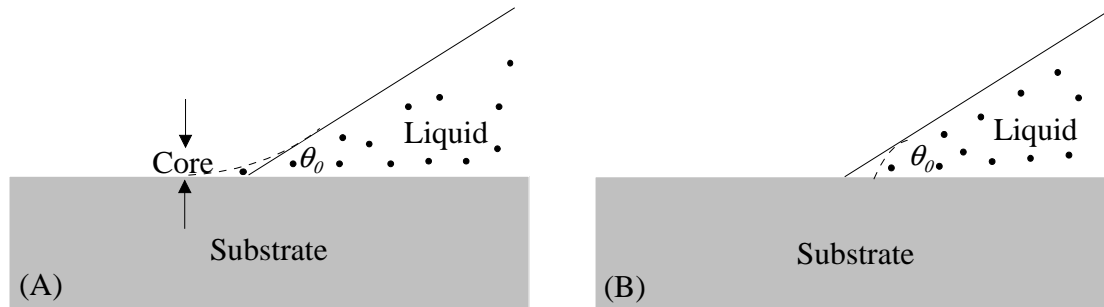


Figure 2.3: Illustration of the core region at the triple line of a solid–liquid–gas interface after {Butt, HJ., 2003}. A) The solid–liquid interactions are stronger than the liquid–liquid interactions. Therefore the core region extends; B) the core region shrinks since the liquid–liquids interactions are stronger than the solid–liquid interactions.

However, Young found that it is possible to relate the equilibrium angle θ_0 to the energies γ_{SV} , γ_{SL} and γ_{LV} without any knowledge of the core region, if the radius of the core region is small compared to the radius of the drop {de Gennes, P.D., 1985}.

2.1.2 Measurements of the contact angle

A common method of measuring the equilibrium contact angle is the sessile drop method, shown in Figure 2.4. A drop is placed on a horizontal surface and observed in cross section through a telescope. A goniometer is used to measure the angle. Several measurements are made on both sides of the drop to obtain an average value.

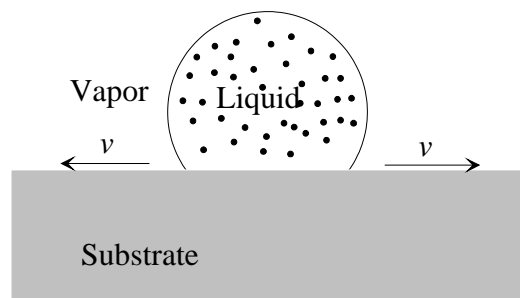


Figure 2.4: Spreading of a liquid drop on a solid substrate using the sessile drop method.

The experimental set up for the sessile drop method is relatively simple compared to other measurement procedures such as the Wilhelmy plate and drop transfer system

which will be explained in more detail below. The sessile drop method is fast and easy to use. However, it is difficult to determine the location of the triple line due to possible reflections of the drop on the polished substrate. Thus, the reproducibility becomes poor and the interpretation of data more difficult. The values obtained by different individual measurements differ typically by 1–2°. For reactive wetting systems, where diffusion or reaction processes occur between the solid and the liquid at high temperatures, the sessile drop method exhibits further disadvantages. Since the liquid is placed on top of the substrate during the heating period, reaction and diffusion processes can occur before the final wetting temperature is reached. Also, since the drop is in contact with the substrate during the heating process and before the final wetting temperature is reached, the wetting process is non-isothermal.

Another method to measure equilibrium contact angles is the Wilhelmy plate method (Figure 2.5) {Wilhelmy, L., 1863}. A thin plate is placed vertically halfway into a liquid. In the case when the liquid wets the plate, the surface tension can exert a downward force. One measures the force required to prevent the plate from being drawn into the liquid. This force is given by {Butt, HJ., 2003}:

$$F = \gamma_{LV} \cos \theta - mg \quad (2.18),$$

where m is the mass of the plate and g the acceleration due to gravity. In determining the force one can calculate the contact angle. The advantages of this method are that the measurements are reproducible since the force measurement is more precise than the measurement of the contact angle with the sessile drop method. In addition the sensitivity of the measurement is high (less than 0.5° error in the contact angle determination). One disadvantage of this method is that the wetting surface must be in the form of a sheet, rod or fiber and all of the surfaces which touch the liquid must have the same wettability {Johnson, R.E., 1993}.

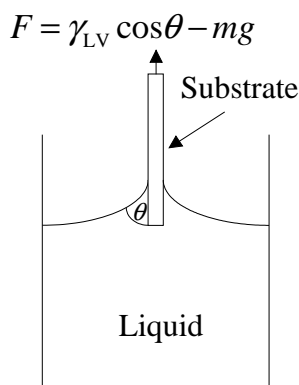


Figure 2.5: A thin plate is placed vertically into a liquid. The force which prevents the plate from being drawn into the liquid (in the case of wetting) is measured. The contact angle is determined by using this measurement. This method of determining contact angles is called the Wilhelmy plate method.

A further method of measuring equilibrium contact angles is the drop transfer method, which is schematically illustrated in Figure 2.6. A liquid drop is placed on a horizontal surface. In order to avoid a retarding force on the drop during the transfer, the liquid must have an obtuse contact angle ($\geq 90^\circ$) with this surface and it must not wet it. A second horizontal plate, the substrate, is then brought into contact with the liquid in order to wet it. The wetting line, which is the triple line at the solid/liquid/vapor interface, moves with a certain velocity and the angle changes with time until the wetting line reaches zero velocity. At this point the contact angle becomes the equilibrium contact angle. This time-dependent angle is called the dynamic contact angle. The time dependence of the dynamic contact angle and the base radius R of the drop is illustrated in Figure 2.7. The contact angle decreases with time until it becomes constant. This constant angle is the equilibrium contact angle. Thus, the wetting process involves the flow of a fluid over a solid and the contact angle cannot be viewed as a static quantity. Therefore the drop transfer method is suitable not only for measuring the equilibrium contact angle but also the spreading kinetics.

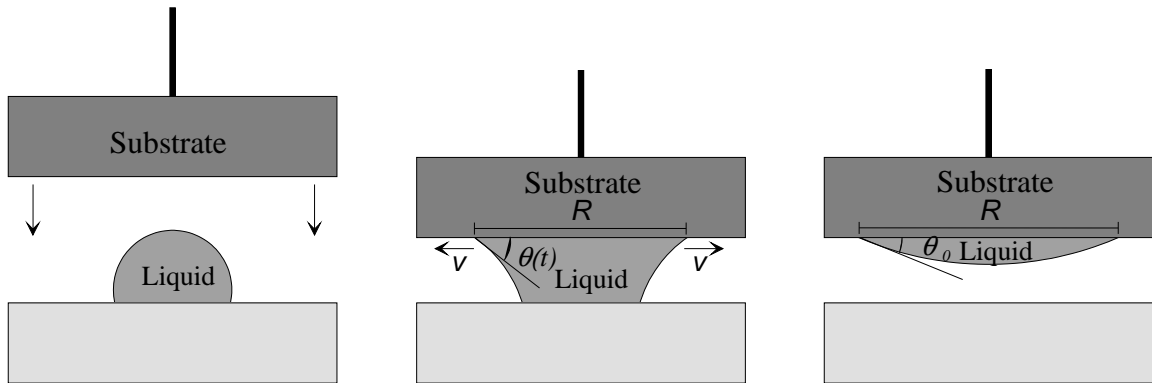


Figure 2.6: Schematic illustration of the drop transfer method. A liquid drop is placed on a horizontal surface which is not wetted. A second plate is brought close to the liquid until it touches the liquid and thus wets this substrate. The contact angle and base radius of the drop change with time.

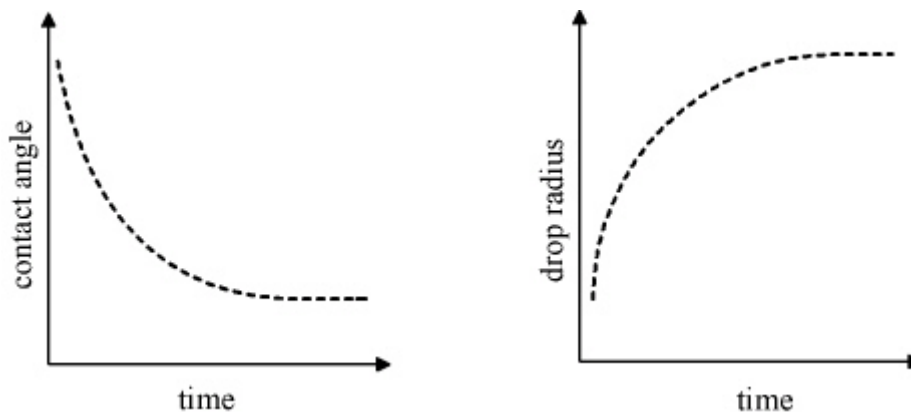


Figure 2.7: Schematic plot of the contact angle and the base radius of the liquid drop versus time.

The advantage of this system is that especially for high-temperature wetting, no reaction or diffusion occur during the heating process since the liquid and substrate are not yet in contact. The disadvantage of the drop transfer method is that it requires a substrate which is not wet by the liquid. In addition vibration of the experimental setup might occur while the second substrate is brought into contact with the liquid, leading to errors in the determination of the dynamic contact angle.

2.1.3 Definition of advancing and receding angle

Young's equation is derived under the condition that the substrate is flat, inert, and non-deformable. Thus the surface of the substrate is treated as an ideal surface. Real surfaces however, show two types of irregularities: surface roughness and chemical inhomogenities. Chemical inhomogenities are spatial variations of atomic or molecular composition. Such surfaces exhibit a hysteresis in contact angle-velocity curves. This means that the equilibrium contact angle measured for a liquid advancing across a surface exceeds that reached by the liquid receding across the surface.

Figure 2.8 illustrates an experimental approach used by Saiz et al. {Saiz, E 1998} to measure equilibrium advancing and receding angles using the sessile drop method in high temperature systems. The sample is shaped either as a tall piece or as a flat plate placed on the substrate. Because, the sample has a lower melting temperature than the substrate, it becomes liquid during heating whereas the substrate remains solid. If the sample is a tall piece, the liquid advances across the surface of the substrate until the velocity of the liquid front becomes zero. The final angle in such a measurement is called "advancing contact angle" (Figure 2.8.A). When the initial sample is a flat plate (Figure 2.8.B), the liquid retracts and the final angle is the "receding contact angle".

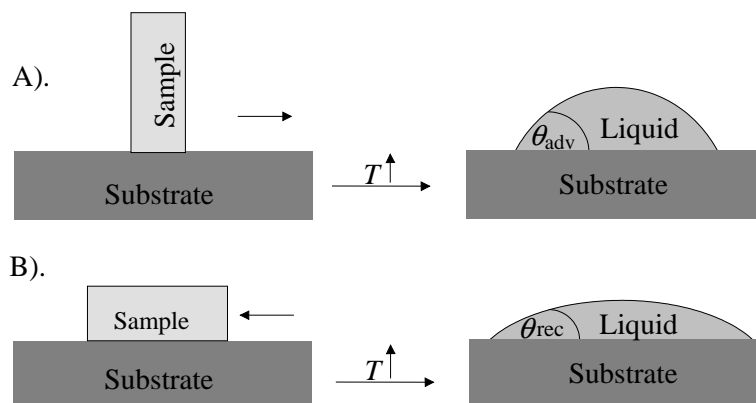


Figure 2.8: Schematic drawing of a sessile drop. Both (A) advancing and (B) receding angle are shown {Saiz, E 1998}.

Other experimental techniques are commonly used to measure advancing and receding contact angles in low temperatures systems. For example, in the Wilhelmy plate method the advancing angle is the stable angle reached when the plate is lowered into the liquid and the receding angle is the stable angle reached after the plate is raised (Figure 2.5).

Due to the hysteresis, the final advancing angle exceeds the final receding angle. The equilibrium angle θ_0 , which would occur if no surface roughness or chemical inhomogeneity on the substrate existed, lies in between these two values {Kistler S.F, 1993}. Figure 2.9 shows the dependence of θ on the velocity of the wetting line. The contact angle varies with speed and direction of motion. In the advancing case, the angle increases with increasing magnitude of the velocity. If the velocity is equal to 0, θ reaches the static advancing contact angle, θ_{adv} . In the receding case the angle decreases with increasing magnitude of velocity. For this case θ reaches the static receding contact angle θ_{rec} if the velocity is equal to zero.

The difference between θ_{adv} and θ_{rec} can be quite large—as much as 50° for water on mineral surfaces. This is generally attributed to surface heterogeneity or surface roughness. The latter effect is illustrated in Figure 2.10. A drop with a contact angle of 90° on top of a substrate is shown. The roughness is illustrated by a microscopically small single spherical distortion of the substrate. The triple line advances from position A to position C. If the liquid drop comes into contact with the distortion it jumps immediately to position B where it has again a contact angle of 90° . This happens on top of the distortion. The drop is hindered from spreading further in order to locally keep a contact angle of 90° . At this stage the macroscopic contact angle appears much larger than 90° . After overcoming the distortion due to the capillary force, the drop continues spreading until it reaches the next distortion. When the liquid recedes, the same effect occurs and a hysteresis can be observed {Butt, H.J., 2003},{Eick, J.D 1975},{Neumann, A.W, 1972}.

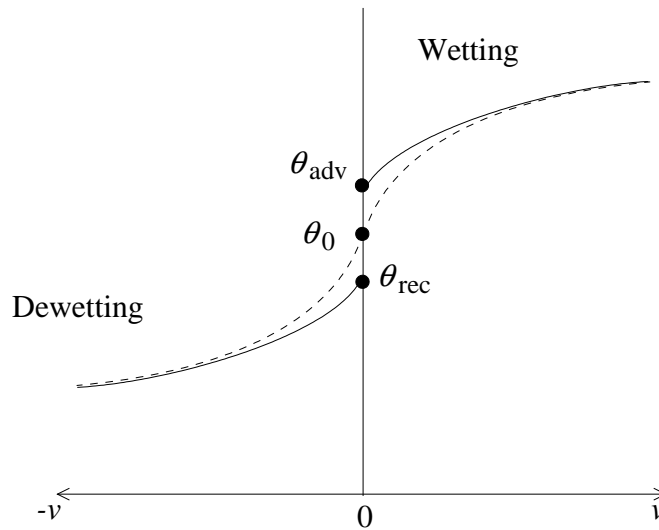


Figure 2.9: Schematic drawing of the advancing and receding contact angle versus the spreading velocity v of the triple line moving along two directions. The advancing angle exceeds the receding angle. This is called contact-angle hysteresis.

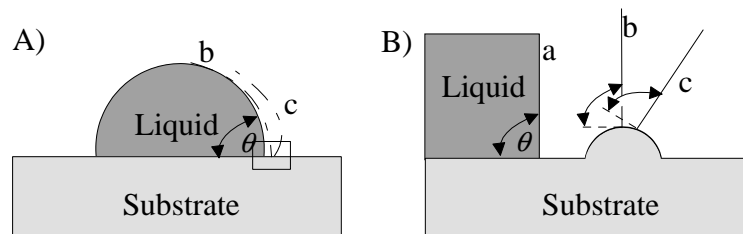


Figure 2.10: A liquid drop is advancing across a substrate possessing a small perturbation. In A) the optically visible situation is illustrated. B shows the microscopic details of the triple line marked in A, {Butt, H.J 2003}. The triple line advances from position A to C.

J. D. Eick et al. {Eick, J.D 1975} studied the hysteresis on an ideal rough surface approximated by a saw-tooth structure with constant surface energy. They used the Wilhelmy plate method to determine the contact angle. The angles β_1 β_2 and the height H were introduced to describe the surface structure and are illustrated in Figure 2.11. Varying β_1 and β_2 and keeping H constant the authors found that as β_1 and β_2 approach 90° , the difference between receding and advancing angle and therefore the hysteresis decreases. If β_1 and β_2 are 90° the difference between receding and advancing angle is

zero and no hysteresis exists. Varying H and keeping β_1 and β_2 constant results in a decrease of the hysteresis with decreasing H {Eick J.D, 1975}. A.W. Neumann et al {Neumann, A.W, 1972}. showed that the hysteresis of the contact angle is a function of the heterogeneity of the surface, i.e. the size and shape of the areas with different surface energies.

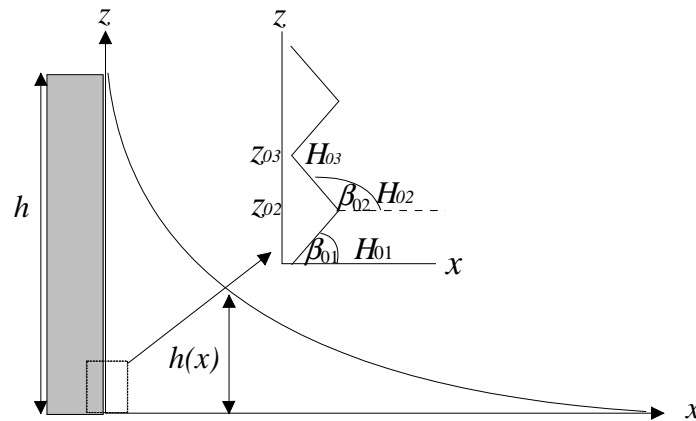


Figure 2.11: Capillary rise of a liquid on a rough surface. The surface is approximated by a saw-tooth structure. The parameters β_1 , β_2 and H describe the rough surface plate, {Eick J. D , 1975}.

2.1.4 Low-/ high temperature spreading

Low-temperature spreading implies that the spreading experiment is performed at $T \ll T_m$, where T_m is the melting point of the substrate. Low-temperature spreading is important in a variety of manufacturing techniques and thus has been extensively studied {Blake, T.D. 1993}, {Kistler, S.F 1993}.

High-temperature spreading occurs if the spreading experiment is performed at $T > 0.5 T_m$. As mentioned earlier (chapter 1), high-temperature wetting remains a largely unexplored field due to the temperature and environmental controls required during the spreading process.

2.2 Theoretical models of low-temperature spreading

The theoretical models of low temperature spreading have been developed for forced and spontaneous spreading as well as for partial and complete wetting systems as is shown in chapter 3. Traditionally the models work better for complete wetting systems.

However, the theoretical models of low-temperature spreading assume that the substrate is smooth, homogeneous, inert, and non-deformable. If a liquid drop contacts a substrate, the system (liquid, solid and vapor) is generally not in its equilibrium state of minimum free energy. Capillary forces drive the system towards its equilibrium by spreading of the liquid over the substrate. During spreading the contact angle θ changes its value from its initial maximum value of 180° (at the moment of contact), towards its equilibrium angle θ_0 in the case of partial wetting, and 0° in the case of complete wetting. As the drop spreads, the radius of the contact area changes from its initial value of 0 mm to its equilibrium base radius R_0 . Since the system changes its energy state from a state of higher energy to a state of minimum energy, energy has to dissipate during spreading. The energy can be dissipated in viscous dissipation in the bulk drop and at the triple line. In principle energy is dissipated in both ways. However a model that treats simultaneously both sources of dissipation has not been developed yet. Consequently there exist two models which consider different main sources of energy dissipation. Both describe the motion of the triple line of the liquid drop while the system equilibrates {De Coninck, J 2001}. The molecular kinetic model considers the friction at the triple line as main source of energy dissipation whereas the fluid flow model considers the viscous dissipation in the bulk drop as main source of energy dissipation.

2.2.1 Molecular kinetic model

The molecular kinetic model describes the motion of the triple line considering only surface effects at the triple line {Blake, T.D., 1993}, {Blake, T.D., 1968}, {De Ruijter, M. 1999}. In its simplest formulation this model neglects hydrodynamic aspects such as viscous dissipation in the liquid drop and at the triple line. Even though the model

neglects these effects, it is capable of linking microscopic quantities such as frequency of the molecular displacement on top of the substrate with macroscopic quantities such as the contact angle. To determine the velocity of the liquid drop as a function of the contact angle, Blake and Heynes {Blake, T.D., 1993} considered only the motion of the atoms or molecules at the triple line, but not in the liquid itself. They assumed that all events relevant for the motion occur at the triple line. The atoms or molecules at the triple line need to overcome an energy barrier to move forward or backward.

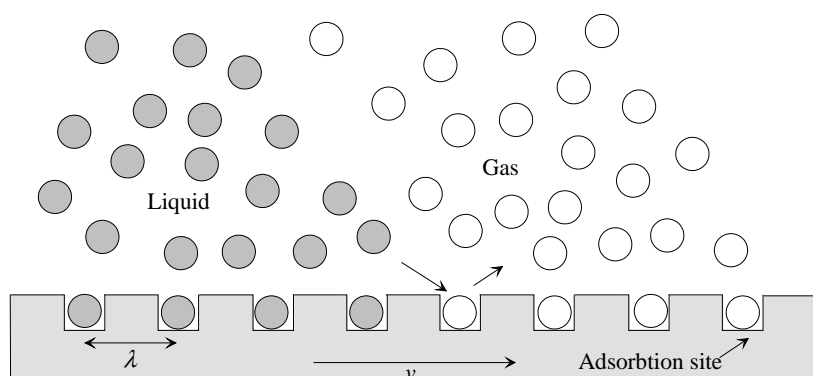


Figure 2.12: Illustration of the molecular kinetic model. The atoms of a liquid advancing across a surface replace the atoms of the gas receding across a surface due to adsorption and desorption. λ is the average distance between adsorption sites after Blake {Blake, T.D., 1968} {Blake, T.D., 1993}.

Atoms moving away from the drop lead to an advancing of the drop (Figure 2.12) whereas the reverse movement makes the drop recede. Molecules or atoms inside the bulk liquid are allowed to move freely without overcoming an energy barrier. If a system is in equilibrium than the wetting line is macroscopically stationary. However, at a molecular level thermal fluctuations appear at the triple line and molecules of the liquid constantly interchange with molecules of the surrounding gas or liquid. On average, the net rate of displacements will be zero and the triple line will fluctuate back and forth about its mean position. Assuming that the frequency of molecular displacements in the forward and backward direction is κ_w^+ and κ_w^- , respectively, the equilibrium is attained if

$$\kappa_w^+ = \kappa_w^- = \kappa_w^0 \quad (2.19).$$

Eyring's theory of absolute reaction rates {Glasstone, S., 1941} relates the equilibrium frequency κ_w^0 to the molar free activation energy of wetting ΔG_w^*

$$\kappa_w^0 = \left(\frac{kT}{h} \right) \exp\left(\frac{-\Delta G_w^*}{NkT} \right) \quad (2.20)$$

where k is the Boltzmann constant, T is the absolute temperature, h is the Planck constant and N the Avogadro number.

Under non-equilibrium conditions, e.g. for an advancing drop, the potential energy barrier away from the drop has to be lower than the potential energy barrier in the backward direction.

Denoting the irreversible work done per unit displacement of unit length of the wetting line by w , the work done per adsorption site is $\frac{w}{2n}$, if n are the sites per unit

area. If the energy barriers for molecular displacements are symmetrical, the work $\frac{w}{2n}$ is

used to lower the barriers in the forward direction and the same for raising the barrier in the backward direction. Then:

$$\kappa_w^+ = \left(\frac{kT}{h} \right) \exp\left(\frac{-\left(\frac{\Delta G_w^*}{N} - \frac{w}{2n} \right)}{kT} \right) \quad (2.21)$$

and

$$\kappa_w^- = \left(\frac{kT}{h} \right) \exp\left(\frac{-\left(\frac{\Delta G_w^*}{N} + \frac{w}{2n} \right)}{kT} \right) \quad (2.22)$$

The net frequency of total displacement is given by

$$\kappa_w = \kappa_w^+ - \kappa_w^- \quad (2.23)$$

$$= \kappa_w^0 \exp\left(\frac{w}{2nkT} \right) - \kappa_w^0 \exp\left(\frac{-w}{2nkT} \right) \quad (2.24)$$

$$= 2\kappa_w^0 \sinh\left(\frac{w}{2nkT}\right) \quad (2.25).$$

If λ is the average distance between the adsorption sites the velocity of the wetting can be written as

$$v = \kappa_w \lambda \quad (2.26)$$

or

$$v = \kappa_w^0 \lambda \sinh\left(\frac{w}{2nkT}\right) \quad (2.27)$$

In order to correlate the velocity with the contact angle, Blake and Heynes assumed that the force required to drive the wetting line is provided by the out-of-balance interfacial tension forces which act at the triple line. This is the result of the change in the contact angle from its equilibrium value θ_0 to the dynamic value $\theta(v)$ {Blake, T.D 1993}:

$$w = \gamma_{LV} (\cos \theta_0 - \cos \theta) \quad (2.28).$$

With (2.27) and (2.28)

$$v = 2\kappa_w^0 \lambda \sinh\left(\frac{\gamma_{LV} (\cos \theta_0 - \cos \theta)}{2nkT}\right) \quad (2.29)$$

In the case of spontaneous spreading of a small drop and vanishing contact angles, it was found that the base radius R and the contact angle θ follow the relationship {De Coninck, J., 2001}:

$$R \sim t^{1/7} \quad \text{and} \quad \theta \sim t^{-3/7} \quad (2.30)$$

It was shown that these relationships work well for some liquid/solid systems {Marmur, A., 1983}, {Dodge, FT, 1988}.

2.2.2 Fluid flow model

In contrast to the molecular kinetic model, which is a microscopic model, the fluid flow model is a macroscopic model. In the fluid flow model the wetting dynamic has been analyzed using continuum mechanics (hydrodynamics). The motion of the triple line in the fluid flow model is derived under the assumption that a capillary force acts as a

driving force and the viscosity of the liquid acts as a retarding force. Thus, the energy is dissipated due to the viscous impedance in the bulk liquid.

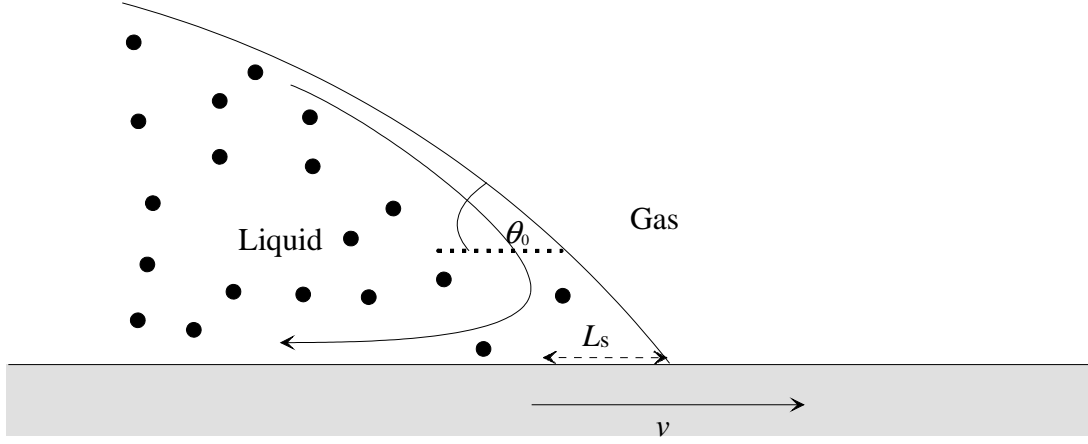


Figure 2.13: A liquid is advancing across a solid surface. Energy is dissipated due to the viscous flow in the liquid. L_S , represents the length of the cutoff region at the triple line, after {Davis, S.H., 1983}.

The relationship between the velocity of the triple line and the macroscopic apparent contact angle can be described by the generalized Hoffmann-Voinov and Tanner law (fluid flow model) {Voinov, O.V., 1976}:

$$Ca = \frac{1}{9 \ln\left(\frac{L}{L_S}\right)} (\theta^3(t) - \theta_0^3) \quad \theta < 135^\circ \quad (2.31),$$

where L is the capillary length, L_S is the slip length, $\theta(t)$ is the dynamic angle and Ca is the capillary number. The slip length L_S is introduced to handle the singularity at the triple line arising from the fluid flow equations. A cutoff region around the triple line is defined in order to cope with this singularity and to determine the angle dependent velocity of the liquid drop. The slip length is the diameter of the cutoff region and will be discussed in more detail later in this chapter. The capillary number Ca is dimensionless and describes a normalized velocity:

$$Ca = \frac{\eta v}{\gamma_{LV}} \quad (2.32)$$

where η is the viscosity of the liquid and γ_{LV} the liquid–vapor interface energy. For spontaneous spreading of a small drop and vanishing contact angles it has been shown that the hydrodynamic regime may be characterized asymptotically by {Gennes de, P.G., 1985}:

$$R \sim t^{1/10} \text{ and } \theta \sim t^{-3/10} \quad (2.33).$$

The assumptions of the hydrodynamic model are that the liquid is incompressible and non-volatile, that there is no-slip of the liquid on a flat and homogeneous substrate, that there is no mass transfer at the fluid/gas interface, and that the local contact angle is in the range between 0° and 180° . Under these assumptions it was found that there are multiple solutions for the velocity field at the triple line derived from the Navier-Stokes equations. The viscous stresses are predicted to increase with $1/d$, where d is the distance from the triple line. Thus the viscous stress would be infinite yielding a singularity at the triple line. However, this singularity of the viscous stress at the triple line does not occur in the experiment otherwise the temperature would rise locally at the triple line. The temperature, and thus the density and viscosity would not be homogeneous over the complete liquid. This would contradict the assumptions of the Navier-Stokes equation. However, it was found that the origin of the singularity is not an artifact of the mathematical approximations, it is rather a result of a failure of one of the assumptions in the traditional hydrodynamic theory {Huh, C 1971}, {Hansen, J 1971}. One of the simplest ways to describe the wetting dynamics with the conventional hydrodynamic theory is to introduce a cutoff length at the triple line and exclude the volume within this cutoff length from the calculations, without identifying a special cutoff mechanism {Kistler, S.F. 1993}. This cutoff length is typically of the order of 10^{-9} – 10^{-8} m {De Coninck, J 2001}. Many researchers tried to introduce special mechanisms in order to cope with the singularity. Some of them neglected viscous effects in the cutoff region {Huh, C., 1971}, {de Gennes, P.G., 1985} {Kistler, S.F., 1993}, other theories introduced slip of the fluid over the solid at the triple line {Kistler, S.F., 1993}. Even though there were many studies done to find an explanation of how to cope with the singularity at the triple line, there is not yet a general explanation which would describe microscopically the dynamic at the triple line {Kistler, S.F., 1993}.

Despite this problem, all investigations and theories predict the same dynamics in the outer cutoff region. Cox {Kistler, S.F., 1993} proved theoretically that the macroscopic contact angle could be calculated without specifying a special cutoff mechanism and that the macroscopic behavior of the liquid could be described with the Hoffmann–Voinov and Tanner law (2.31).

2.3 Factors affecting the wetting process

2.3.1 Adsorption

The adsorption of atoms (as for example, oxygen or carbon) on solid and liquid surfaces and at solid–liquid interfaces leads to a reduction in the surface and interface energies. Figure 2.14 shows the hypothetical dependence of the different surface energies of a solid-liquid-vapor system on the activity of an active element {Saiz, E. 2000}. Since the equilibrium amount of adsorbate depends on the activity, it can be used as a measure of the amount of adsorbate on the surface.

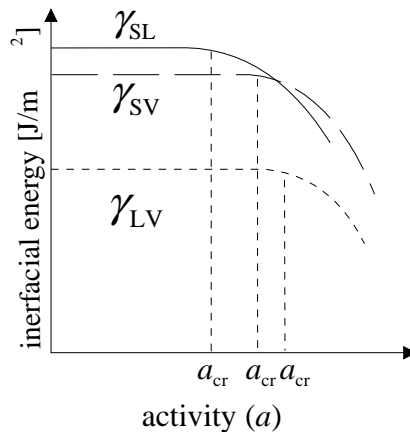


Figure 2.14: Hypothetical variation of the interfacial energies (γ_{SL} , γ_{SV} , γ_{LV}) versus the activity a due to adsorption effects (for example oxygen or carbon adsorption)

A critical activity a_{cr} exists where the surface interface energy decreases with increasing activity. Depending on the amount of adsorbate the equilibrium contact angle decreases or increases. This can be derived from Young's equation (2.1b) by introducing activity dependent surface energies.

A special situation arises if the primary source of the adsorbate for the solid is the liquid itself. 'Dry' spreading occurs when the spreading velocity of the liquid is too fast for adsorption equilibrium to develop on the surface of the substrate ahead of the liquid (Figure 2.15A) {de Gennes, P.G., 1985}{Cannon, R.M. 1995}. Substituting the energy for a pure surface γ_{SV}^0 by γ_{SV} with ($\gamma_{SV}^0 > \gamma_{SV}$) into the Young equation implies a low value of the angle $\theta_{0_{dry}}$. Even when the initial spreading is dry spreading, in most cases the adsorbate tends to reach its equilibrium value, so that with time one can reach a lower γ_{SV} and thus a higher θ . If adsorption equilibrium is reached before spreading, the so called 'equilibrium' wetting occurs (Figure 2.15 B).

Some examples for 'dry' and equilibrium spreading are given by {Cannon, R.M., 1995}{Sharps, P.R., 1981}{Saiz, E., 2000}. Sharps et al. observed that the contact angle of a liquid metal on a metal substrate (Cu-Ag system) was lower in the case of a non-pre-equilibrated substrate than in the case of a pre-equilibrated substrate {Sharps, P.R., 1981}. According to Saiz et al. {Saiz, E., 2000} 'dry' spreading could explain this effect. In the non pre-equilibrated case the spreading velocity may be too fast to obtain adsorption. Thus one could consider this as 'dry'-wetting case.

Cannon et al. {Cannon, R.M., 1995} proposed that, depending on the amount of evaporation of adsorbate from the surface ahead of the triple line, situations with contact angles between those for equilibrium and 'dry' wetting can occur.

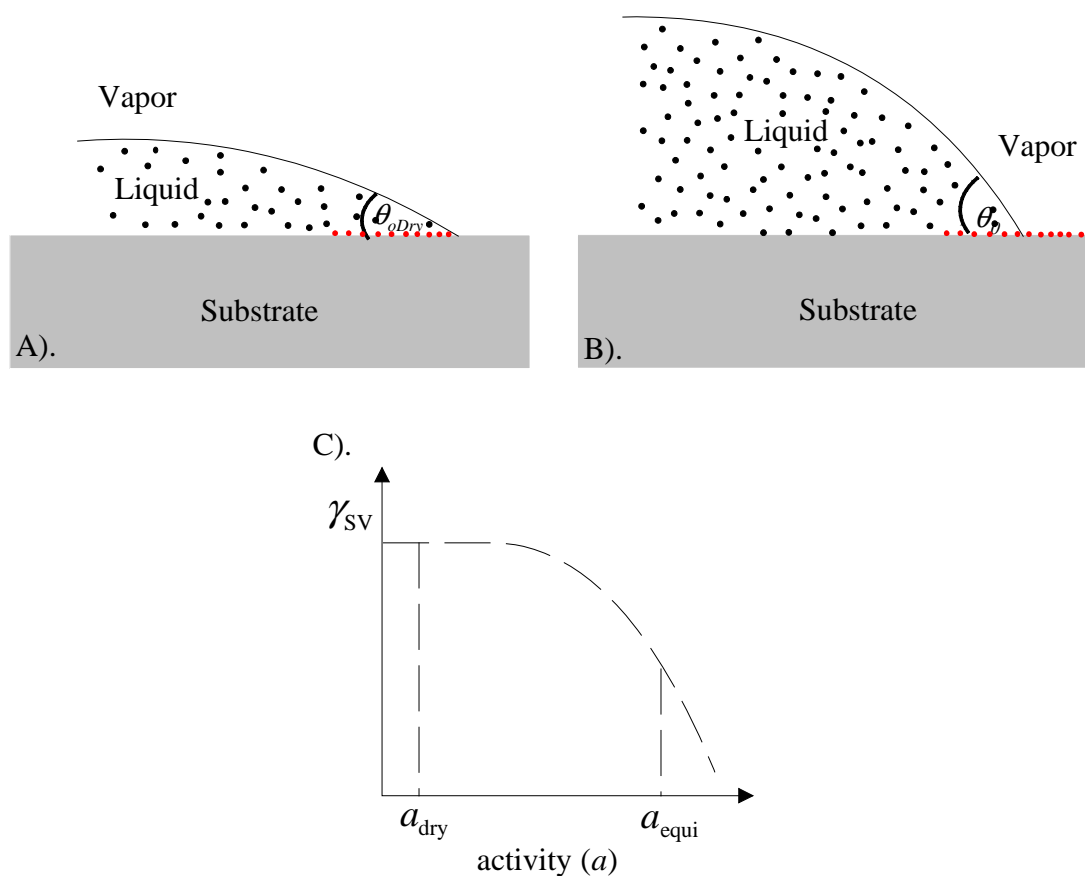


Figure 2.15: Schematic drawing of a liquid drop on a substrate A): In case of ‘dry’ spreading, the substrate is initially clean; B): for equilibrium wetting, atoms of the liquid are adsorbed on the substrate. The diagram C) illustrates the dependency of γ_{SV} on the activity in the dry and equilibrium case.

2.3.2 Ridge formation

Young’s equation only applies to systems where the substrate is perfectly rigid and insoluble, and where the triple line can only move in the direction parallel to the substrate. In this case vertical force components can be neglected and the Young equation is derived by balancing the horizontal force components. This approximation is valid for many low-temperature systems like organic liquids on hard, high-cohesive energy substrates such as most metals or ceramics. In this case the elastic distortions of the solid caused by the vertical components of the interfacial tensions are negligible. However, in the case of soft substrates with a low-cohesive energy (e.g. rubbers, elastomers or gel) elastic distortions are not negligible. When liquids are in contact with

soft solids pronounced local elastic deformation and formation of a triple line ridge on the substrate surface may occur. The ridges can be several tens of nanometers tall and they can affect the dynamics of wetting {Carré, A., 1996},{Carré, A., 1995}.

For most high-temperature systems (e.g., molten metals or oxides on ceramics or metals) the temperatures during the experiment are typically $\geq 0.5 T_m$, and therefore, local atomic diffusion can occur. This provides a mechanism for ridge formation even for hard substrates. In the case of ridge formation, spreading requires motion of the triple line both horizontally and vertically, which leads to two independent relations:

$$\frac{\sin \phi_S}{\gamma_{LV}} = \frac{\sin \phi_L}{\gamma_{SV}} = \frac{\sin \phi_V}{\gamma_{SL}} \quad (2.34),$$

where ϕ_S , ϕ_L , ϕ_V are equilibrium dihedral angles in the solid, liquid and vapor, respectively. These dihedral angles are visualized in Figure 2.16.

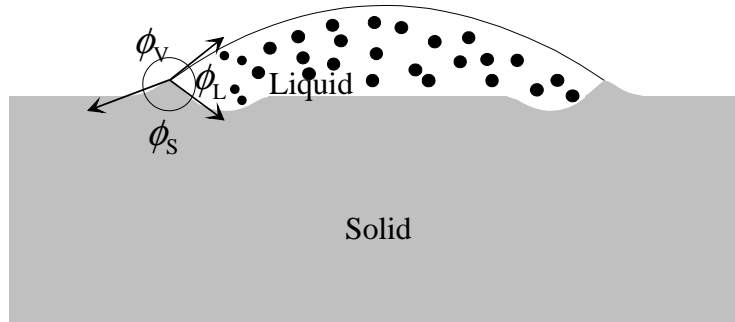


Figure 2.16: Illustration of the dihedral angles in the case of ridge formation, taken from {Saiz, E 1998}

The ridge will evolve until complete equilibrium is reached. If a ridge is present one has to differentiate between microscopic and macroscopic angles. The microscopic angles are the aforementioned dihedral angles ϕ_S , ϕ_L , ϕ_V . The macroscopic angle is the angle between the tangent of the liquid/vapor interface at the triple line and the unperturbed substrate surface. The presence of a ridge can strongly influence the spreading kinetics and the equilibrium angle. The observed spreading rates can be orders of magnitudes lower than for liquids, where the flow is just controlled by

capillarity and viscosity. Saiz et al. {Saiz, E 1998} divided the spreading process into four stages, depending on the degree of ridge growth. The four different regimes are stipulated by the size of the ridge compared to the radius of the drop curvature and the ridge growth velocity compared to the spreading velocity. The geometrical situations corresponding to the different regimes are schematically shown in Figure 2.17. In the first regime, the deformation which occurs at the triple line is due to elastic strains in the solid. In the case of metallic or ceramic substrates this distortion was calculated and found sufficiently small such that no plastic deformation is expected. In this regime the capillary forces drive the contact angle towards the one defined by Young's equation. The first regime is found at short times when the liquid spreads very fast with a high driving force so that a triple line ridge would be unstable, or at such low temperatures that diffusion is very slow so that only elastic ridges can form {Saiz, E., 1998}. In the second regime some diffusion processes or solution precipitation are allowed to occur. The substrate will deform at the triple line. There exists a certain time where the ridge will be small compared to the radius of curvature of the liquid. In this regime capillary forces will drive θ towards a value close to Young's angle but spreading kinetics will be dictated by the velocity at which the attached ridge moves. Microscopically the so called 2D equilibrium of the interfacial forces (in both directions, perpendicular and parallel to the substrate surface) is reached at the triple line ridge (2.34). If the ratio of the height h of the ridge over the curvature R of the liquid exceeds 0.1, capillary forces do not drive the macroscopic contact angle towards the Young's angle {Saiz, E., 1998}. In this case the ridge is large compared to the radius of curvature of the drop. The so called microscopic 2D equilibrium angle is reached microscopically. This is considered as the third regime. The fourth regime describes complete equilibrium, which means macroscopic 2D equilibrium and constant curvature. To reach full 2D equilibrium, times much longer than the experimental ones might be necessary in many practical systems.

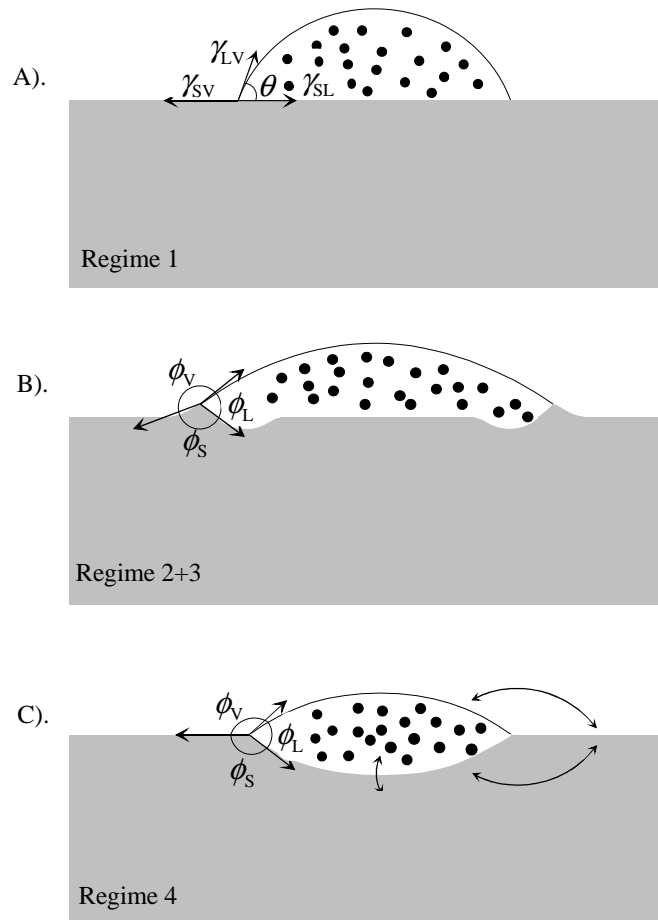


Figure 2.17: The geometry of a liquid drop on a substrate depends on time. In Regime 1 (A) the spreading velocity of the liquid is faster than the ridge formation. The liquid spreads on a flat surface. Regime 2+3 (B): a ridge can form, depending on the ratio of the height of the ridge compared to the curvature of the liquid one differentiates between Regime 2 and 3. Regime 4 (C): full equilibrium is obtained. The curvature of the drop is constant. After {Saiz, E 1998}.

An important question is whether in the case of ridge formation the liquid is going to remain attached or will break away and a new ridge will form. A simple geometrical model was used to derive the attachment range of macroscopic contact angles {Saiz, E., 2001}. If the macroscopic contact angle is in this range the liquid is considered to be pinned at the ridge. Figure 2.18 shows a ridge at the triple line of liquid, solid, and vapor. In the geometrical model the ridge is considered to be a wedge. The ridge exhibits the angles m_- and m_+ with the unperturbed horizontal plane of the substrate, and

θ_i is the angle of incidence of the liquid surface with the unperturbed horizontal substrate.

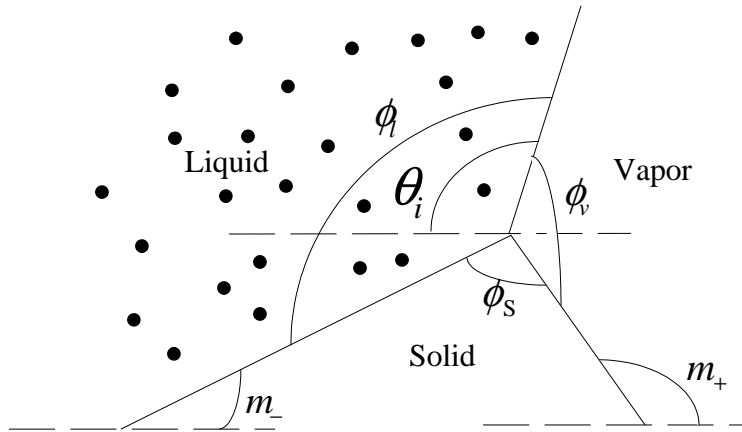


Figure 2.18: Geometrical representation of a triple line ridge. The ridge is idealized as a ramp and its orientation is given by the angle of the apex (m_+ and m_-). θ_i is the angle between the liquid front and the horizontal substrate. ϕ_s , ϕ_l , ϕ_v are the dihedral angles, after {Saiz, E., 2001}.

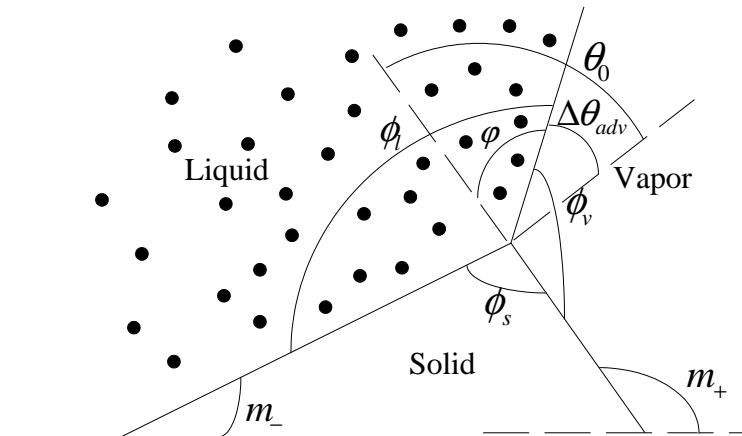


Figure 2.19: Schematic of the triple line ridge, illustrating the attachment range for an advancing liquid front {Saiz, E., 2001}.

Firstly, the movement of a liquid advancing across the surface is considered. Therefore the movement of the liquid along the m_+ plane of the ridge requires closer investigation (Figure 2.19). With φ as the angle between the m_+ plane and the liquid-vapor front, the one-dimensional Young's angle θ_0 may be written as:

$$\theta_0 = \varphi + \Delta\theta_{adv} \quad (2.35)$$

If $\varphi < \theta_0$ the liquid front would be driven by capillary forces to a value close to the Young's angle. Therefore the angle φ has to increase. This would result in a receding movement of the liquid along the imaginary m_+ plane. Thus the spreading front is considered to be pinned by the ridge, in the case where the ridge does not have time to rotate to adjust its position. If $\varphi > \theta_0$ the liquid front would also be driven by capillary forces close to the Young's angle and thus the angle φ has to decrease. However, this would result in an advancing movement of the liquid along the m_+ plane. Thus, the spreading front will jump to $\theta_i + \Delta\theta_{adv}$, i.e. it will break away from the ridge. Hence, the pinning condition for the advancing case can be written as {Saiz, E 2001}:

$$\Delta\theta_{adv} \geq 0 \quad (2.36).$$

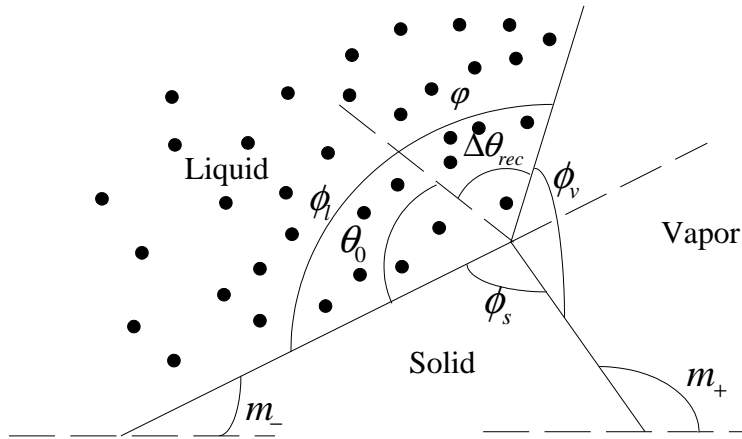


Figure 2.20: Attachment range for a receding liquid front at a triple line ridge {Saiz, E 2001}

Figure 2.20 shows schematically the situation of the receding movement of a liquid over a ridge. In this case, φ is the angle between the m - plane and the liquid-vapor front. The one-dimensional Young's angle θ_0 amounts to:

$$\theta_0 = \varphi - \Delta\theta_{\text{rec}} \quad (2.37)$$

If $\varphi > \theta_0$ the angle φ had to decrease in order to reach equilibrium. Therefore the liquid had to advance along the imaginary m . plane. If the ridge does not have time to rotate to adjust its position, the spreading front is then considered to be pinned by the ridge. If $\varphi < \theta_0$ the liquid front would also be driven by capillary forces close to the Young's angle. In this case the angle φ has to increase. The liquid would recede along the m . plane. Thus, the spreading front will decrease below $\theta_i - \Delta\theta_{\text{rec}}$, i.e. the triple line will break away from the ridge. Therefore, the pinning condition for the receding case becomes {Saiz, E 2001 }:

$$\Delta\theta_{\text{rec}} \geq 0 \quad (2.38).$$

The total pinning range can be written as {Saiz, E 2001 }:

$$\theta_i - \Delta\theta_{\text{rec}} \leq \theta_i \leq \theta_i + \Delta\theta_{\text{adv}} \quad (2.39).$$

If the 2D-equilibrium (2.34) is maintained at the triple line, the angles m . and m_+ can be related to the corresponding dihedral angles as:

$$\phi_1 = \theta_i + m_- \quad (2.40)$$

$$\phi_s = m_+ - m_- \quad (2.41)$$

$$\phi_v = 2\pi - \theta_i - m_+ \quad (2.42).$$

$\Delta\theta_{\text{adv}}$ and $\Delta\theta_{\text{rec}}$ can be written as:

$$\Delta\theta_{\text{rec}} = \phi_1 - \theta_0 \quad (2.43)$$

$$\Delta\theta_{\text{adv}} = \theta_0 + \phi_v - \pi \quad (2.44)$$

Replacing $\Delta\theta_{\text{adv}}$ and $\Delta\theta_{\text{rec}}$ as well as the dihedral angles in equation (2.39) through equations (2.40)-(2.44) the range of macroscopic angles for which the overall energy of the system will increase if the triple line breaks away will be

$$\theta_0 - m_- \leq \theta_i \leq \theta_0 + 2\pi - m_+ \quad (2.45)$$

Equation (2.45) shows that the pinning range depends only on the ridge angles and not on its height. Once a ridge is attached, the movement of the ridge determines the spreading velocity assuming that the ridge is small enough to belong to the second regime. Saiz et al. found that the higher the melting point of the substrate, i.e. the higher the surface energy, the larger the expected attachment range {Saiz, E., 2001}. They observed that in the case of spreading of liquid aluminum on sapphire at 1100 °C in vacuum, a final angle of 80° was reached. After approximately 20 minutes the final angle decreased to 60° and then jumps to the maximum value of 80°. After removing the aluminum from the sapphire substrate, ridges were visible which had formed corresponding to each jump. Many authors postulated for the Young's equilibrium angle of aluminum on sapphire a value of ~80° {Carnahan, R.D., 1958}, {Saiz, E., 1998}. It was claimed that evaporation of the aluminum takes place and that this results in a decrease of the final angle. Thus the contact angle is not within its attachment range (2.45) and the triple line will break away from the ridge. Calculations of Saiz et al. confirm this behavior {Saiz, E. 2001}.

2.4 Mullins theory of grooving

The ridge growth velocity can be controlled by interfacial diffusion. The corresponding differential equations were developed by Mullins in order to describe grain boundary grooving. To determine the ridge growth velocity the Mullins equations must be solved with new boundary conditions. In order to have a better insight into ridge growth a short overview of Mullins theory will be given.

2.4.1 Summary of Mullins theory of grooving

On the surface of an annealed polycrystalline material a groove will form where a stationary grain boundary intersects the surface. Figure 2.21 shows a profile of a grain boundary that ends at the surface. The groove develops such that the sum of the two

surface energies and the grain boundary energy is zero at the root. The equilibrium dihedral angle Φ_{sl} is given by

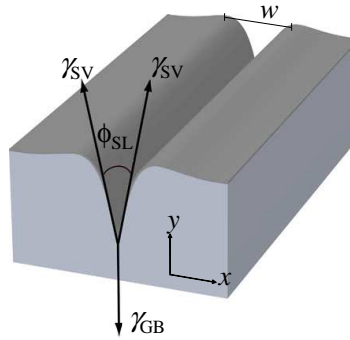


Figure 2.21: Illustration of a grain boundary groove which intersects the surface of a substrate. Φ_{sl} is the equilibrium angle, γ_{sv} the surface energy, and γ_{GB} the grain boundary energy {Mullins, 1956}.

$$2\gamma_{sv}\cos\Phi_{sl}=\gamma_{GB}. \quad (2.46)$$

The formation of the equilibrium angle occurs due to atomic migration in the region of the intersection. Humps appear at both sides of the grain boundary when groove evolution is controlled by diffusion. These humps tend to flatten by either condensation and evaporation or surface diffusion. This flattening upsets the equilibrium angle and forces the groove to deepen {Mullins, 1956}. Mullins used the following assumptions to derive and solve the differential equations which describe the development of the groove profile: The system is closed and contains a poly-crystal in quasi-equilibrium with its vapor. The properties of the interface are independent of its orientation with respect to the adjacent crystals. The only mechanisms operative in the transport of matter are evaporation-condensation and surface or volume diffusion. The process of grooving is described by the use of macroscopic concepts such as surface curvature and surface energy. Effects arising from the atomistic nature of crystals and crystalline imperfections are ignored. With these assumptions the time dependent profile of a groove surface can be calculated for the case of grooving controlled by surface diffusion. One result of the calculation is the time dependence of the groove width w (Figure 2.21), which is the distance between the two maxima in the profile at both sides of the groove. By measuring the groove width as a function of time one can

directly determine the surface diffusion coefficient. Assuming surface diffusion to be the only mass transport mechanism in operation, the grain boundary profile can be derived as follows: with μ (K) as the chemical potential per atom, K the curvature on a surface, Ω as the molecular volume, it was shown that {Mullins, 1956}

$$\mu(K) = K\gamma\Omega \quad (2.47).$$

This equation implies that a gradient in the chemical potential is associated with a gradient in curvature. These gradients in the chemical potential will result in a drift of atoms from areas of high potential energy to areas of lower potential energy. Since the curvature is equal to zero on a flat surface and infinity on the groove root the atoms will drift from the groove root, to the flat surface. The drift will have an average velocity V which is given by the Nernst-Einstein relation,

$$V = -\frac{D_s}{kT} \frac{\partial\mu}{\partial s} = -\frac{D_s\gamma\Omega}{kT} \frac{\partial K}{\partial s} \quad (2.48).$$

D_s is the surface diffusion coefficient, s is the arc length across the profile, k is the Boltzmann constant, and T the temperature. If one multiplies the average velocity by the number of atoms per unit area α the surface current J is obtained:

$$J = -\frac{D_s\gamma\Omega\alpha}{kT} \frac{\partial K}{\partial s}. \quad (2.49)$$

This surface current gives information about the number of atoms which cross a line on the surface per unit time. The derivative of the surface current $\frac{\partial J}{\partial s}$ is equal to the increase in the number of atoms per unit area. Multiplying this derivative by the molecular volume Ω , the speed of movement of a surface element r_n along its normal is obtained,

$$r_n = \frac{D_s\gamma\Omega^2\alpha}{kT} \frac{\partial^2 K}{\partial s^2} \quad (2.50)$$

In the investigation of grooving it is important to determine the velocity of ridge growth along the y -direction (see Figure 2.21). Substituting r_n by $y(x,t)$ and using a small-slope approximation, Mullins derived the differential equation for groove growth:

$$\frac{\partial y}{\partial t} = -B \frac{\partial^4 y}{\partial x^4} \quad (2.51),$$

where B is the Mullins constant

$$B = \frac{D_s \gamma \Omega^2 \alpha}{kT} \quad (2.52).$$

Using the following boundary conditions

$$y(x,0) = 0 \quad (2.53)$$

$$y'(0,t) = m \quad (2.54)$$

$$y'''(0,t) = 0 \quad (2.55)$$

the time-dependent groove width is {Mullins, 1956}

$$w = 4.6(Bt)^{1/4} \quad (2.56).$$

In this section the time dependent profile of a groove surface was calculated for the case of grooving controlled by surface diffusion. Mullins did not only solve the case for surface diffusion but also for volume diffusion. However at any given moment the atoms are traveling along all paths: the surface, the interface, through the solid and through the liquid. Groove evolution is in general controlled by the fastest of these paths for diffusion. Triple line ridging is analyzed under the assumptions that the rate determining step was interfacial diffusion applying Mullins differential equations.

2.4.2 Relation between Mullins grooving theory and ridge formation theory

Mullins equations can not be applied directly to the calculation of the ridge movement because the assumptions (i.e. in the boundary condition) used for grain boundary grooving are not valid for the development of a ridge profile. Using similar assumptions as Mullins assumptions but different boundary conditions, Saiz et al. {Saiz, E., 1998} were able to calculate, under certain conditions, the velocities involved in the formation and movement of a ridge. Mullins considers only identical surface energies and diffusivities at both sides of the groove. These conditions are no longer valid if ridge formation occurs. Asymmetrical surface energies and diffusion along the solid–vapor interface and the solid-liquid interface have to be taken into account (Figure 2.22).

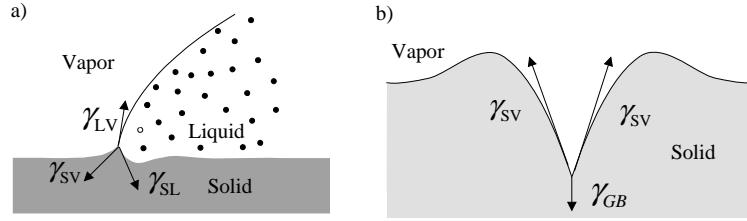


Figure 2.22: The boundary conditions of a ridge at the triple line at a solid liquid interface (a) are compared with the boundary condition of a groove which intersects a surface (b) {Saiz, E 1998}.

E. Saiz {Saiz, E 1998} calculated the ridge-growth velocity considering two special cases. In the first case, the ridge moves at a constant velocity along the surface of the substrate. The ridge does not change its size or shape. With this steady state condition the ridge growth perpendicular to the substrate is therefore zero ($v_{\perp} = 0$). Under the condition that the solid-liquid diffusivity is larger than the diffusivity solid-vapor ($D_{sl} \gg D_{sv}$) the solutions for advancing and receding fronts are {Saiz, E., 1998}:

$$v_{ss}^{adv} = B_{sv} \left(\frac{\tan(\pi - \phi_s)}{h} \right)^3 \quad (2.57),$$

$$v_{ss}^{rec} = B_{sl} e^{\pi/6\sqrt{3}} \left(\frac{2 \tan(\pi - \phi_s)}{h\sqrt{3}} \right)^3 \quad (2.58).$$

B is the Mullins constant, which depends in the case of B_{sl} on the diffusion coefficient D_{sl} and in the case of B_{sv} on the diffusion coefficient D_{sv} . Since $D_{sl} \gg D_{sv}$, the velocity for the advancing front depends on the slower diffusivity and has therefore the smaller coefficient for the same ridge height. Thus, the velocity in the advancing case is slower than in the receding case as can be seen from equations (2.57) and (2.58). The second case E. Saiz {Saiz, E., 1998} considers is where the macroscopic angle is approximately the Young's angle ($\theta \approx \theta_0$). The velocity of the ridge v_{\parallel} parallel to the substrate is then equal to zero and the ridge grows only in height. The calculated velocity is similar to the calculated groove velocity determined by Mullins for the symmetrical ($B_{sl} = B_{sv}$) case:

$$v_{\perp} = \frac{[0.973(\tan \pi - \phi_s)]^4 B}{4h^3} \quad (2.59).$$

2 Fundamentals

For the asymmetrical case ($B_{sl} \gg B_{sv}$) the ridge growth will depend on the higher diffusivity. The two cases E. Saiz discussed are limiting cases which are rarely found experimentally. In reality, the ridge shape and size will change during the spreading experiment. The general equations describing the experimental case are however not solved. Nevertheless, a trend can be seen by combining the results, described above {Saiz, E 1998}.

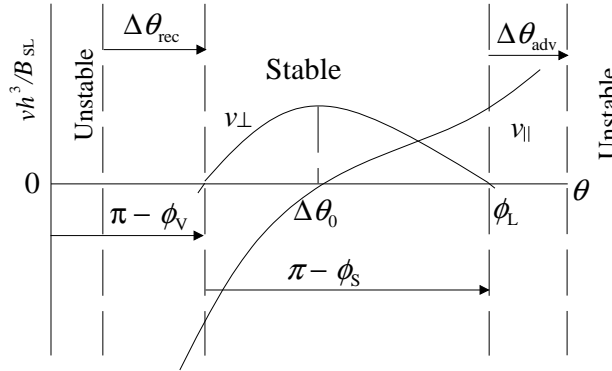


Figure 2.23: The stability range of the ridge, the velocity for a ridge growth v_{\perp} as well as the velocity parallel to the substrate v_{\parallel} are plotted against the macroscopic contact angle, after {Saiz, E 1998}.

As shown in equations (2.57-2.59), all of the derived velocities scale as B/h .³ Therefore, the velocities can be normalized with h^3/B and then plotted as a function of θ (Figure 2.23) {Saiz, E 1998}. The scheme is valid for small ridges as described in the second regime. If the velocity v_{\perp} is equal to zero the first of the aforementioned steady state solutions is reached. As previously described the magnitude of the advancing velocity $v_{\parallel adv}$ at this point is smaller than the magnitude of the receding velocity $v_{\parallel rec}$, since $D_{sl} \gg D_{sv}$. If v_{\parallel} is equal to zero, then $\theta \approx \theta_0$ and the velocity of the ridge growth perpendicular to the substrate v_{\perp} reaches its maximum value, and hence, the second steady state condition is reached. As can be seen in Figure 2.23 if θ lies between the values for the steady state cases then the more rapidly the ridge grows perpendicular to the substrate, the slower it moves parallel to the substrate. A triple line moving along a smooth substrate should form a ridge spontaneously if θ is in this range. In this region a scratch can act as a ridge and grow even further. The closer the contact angle approaches the equilibrium contact angle the lower the chance that the triple line breaks

away from the ridge. If θ is outside the values for the steady state case, the ridge will shrink more rapidly the greater the distance $|\theta - \theta_0|$ is. The drag for spreading will decrease and thus the receding as well as the advancing front will move faster. The probability increases that the triple line breaks away from the ridge. A liquid spreading on a smooth substrate would not form a ridge and scratches would not act as incipient ridges. The normalized velocities vh^3/B are dependent on the contact angle θ as well as on the Mullins constants B_{sv} and B_{sl} . Equations 2.57 and 2.58 show that the magnitude of the velocity in the advancing and receding cases depends on the Mullins constant. This magnitude of velocity determines the point at which the velocity curve v_{\parallel} intersects a vertical line at the steady state situations ($v_{\perp} = 0$) {Saiz, E 1998}.

E. Saiz et al. {Saiz, E 1998} studied the ridge growth using the assumption that there is no initial perturbation for a ridge, (like scratches), that the substrate is completely flat and that the ridge growth is controlled by interfacial diffusion. Under these assumptions there is a condition where a ridge cannot grow even though the contact angle is in the range for stable ridge growth {Saiz, E., 2001, A}. In this case diffusional fluxes are responsible for a ridge growth if the ridge height is infinitesimal. These fluxes are limited by the atomic jump frequency of the atoms of a substrate. If the jump frequency becomes too slow compared to the spreading velocity a ridge, which is at the initial stage atomic sized, can not form. This spreading velocity is called the critical velocity. The critical velocity v_{cr} can be estimated by

$$v_{cr} = \frac{6D_{sl}}{a} \quad (2.60),$$

where a is the jump distance. Hence, if the spreading velocity is faster than the critical velocity a ridge can not nucleate.

3 Literature overview

3.1 Comparison of the molecular kinetic model and the fluid flow model with experiments in low-temperature systems

Both the molecular model and the fluid-flow model have been applied in forced as well as in spontaneous spreading systems for complete and partial wetting. However, traditionally the models work better for systems with complete wetting. This work concentrates on spontaneous and partial wetting. Therefore an overview of some examples of low-temperature wetting experiments, which have shown a partial wetting behavior, and their comparison with the theoretical models is given. One of the concerns of comparing these models with experimental data is that the models result in similar types of graphs. Therefore the data can be fitted with either one of the models. In order to separate the two models one has to analyze the physical implications of the fitting parameters.

Blake {Blake, T.D., 1993} demonstrated the utility of the theory of the molecular kinetic model on the spreading kinetics of a 70 % aqueous solution of glycerol on Mylar polyester tape, which is forced and partial wetting system. The viscosity of the solution of glycerol was 45.6 mPa*s. The wetting data were taken from Burley and Kennedy {Burley, R. 1976, A}, {Burley, R. 1976, B}. The authors measured the advancing contact angle as a function of the wetting velocity and compared those data with the molecular kinetic model, which described the data well {Blake T.D., 1993}. The theoretical curve of the molecular model was obtained by nonlinear regression using equation (2.29). The calculated distances between adsorption sites ($\lambda = 0.92$ nm) are as

expected in the order of atomistic distances. The calculated wetting activity ΔG_w^* is 49kJ/mol and the frequency κ_w^0 is $8.1 \times 10^3 \text{ s}^{-1}$. These calculated parameters are in good agreement with adsorption and diffusion data of solid surfaces {de Boer, J.H., 1953}, {Ehrlich, G. 1980}. They are also in the range of those reported for low-temperature liquids {Schneemilch, M., 1998}.

M. de Ruijter et al. {Ruijter, M. de 1998} investigated the spontaneous spreading kinetics of the system squalane (which is a non-polar hydrocarbon) as a liquid and polyethyleneterephthalate (PET) as a substrate. This system shows partial wetting behavior. The experiments were performed at different temperatures. The authors fitted their experimental data to the fluid flow model and found that the slip length L_S is $4.2 \times 10^{-14} \text{ m}$, which is smaller than the molecular length. The parameter obtained is therefore not physically meaningful and the fluid flow model does not apply. When M. de Ruijter et al. {Ruijter, M. de 1998} compared their experimental data with the molecular model, they found that the distances between adsorption sites ($\lambda = 1.09 \text{ nm}$) are in the order of atomistic distances. The calculated wetting activity ΔG_w^* for the different temperatures ranges is between 12–15.1kJ/mol and the frequency κ_w^0 is between $2.7\text{--}3.5 \times 10^{10} \text{ s}^{-1}$. There is a weak temperature dependency of the wetting activity observable, which can not be explained with the molecular kinetic model. The absolute values calculated by Ruijter et al {Ruijter M. de et al, 1998} are similar to published values of Blake T.D. and co-workers, {Blake T.D,1993}. In summary, the molecular kinetic model is able to represent the dynamic contact angle behavior at different temperatures. This indicates that for these systems the dissipation near the wetting line is more important in comparison to the dissipation due to viscous flow in the liquid.

A general problem in explaining wetting behaviors with the fluid flow model is the fact that the flow cannot simply be described by hydrodynamics since such a description reveals a singularity at the triple line. Thus great effort has been put into determining the detailed physical mechanism which results in a finite wetting behavior. Before Cox proved 1986 {Cox, R.G, 1986} theoretically that the macroscopic contact angle could

be calculated without specifying a special cutoff mechanism and that the macroscopic behavior of the liquid could be described with the Hoffmann-Voinov and Tanner law, most studies had focused on the physical mechanism at the triple line. However, the macroscopic contact angle in all these investigations was successfully described by the Hoffmann-Voinov-Tanner law or, in other words, by the fluid flow model.

For many spontaneous and complete wetting systems, the spreading kinetics were investigated and found to be in good agreement with the fluid flow model. Some examples are given by Tanner {Tanner, L.H., 1979}, Chen {Chen, J.D, 1987} and Ausserré et al {Ausserré, D, 1986}. Tanner {Tanner, L.H., 1979} investigated the spreading kinetics of silicone oil, with a viscosity of 106 Pa*s, on glass. Ausserré et al. {Ausserré, D, 1986} studied the spreading kinetics of silicon fluids on silicone wafers. The silicon had a 20Å thick SiO₂-layer on top of the silicon substrate. Chan et al. {Chen, J.D, 1987} investigated the spreading kinetics of a silicone liquid with a viscosity of 0.198 Pa*s on a soda-lime glass. In all of these examples gravity effects could be neglected. The agreement of these spreading drop data with the fluid flow model suggests that for these systems the energy dissipation during the spreading process can be explained as due to viscous flow in the liquid.

The spreading dynamics in forced wetting systems have been reported in various publications. In a forced wetting system an externally imposed force (hydrodynamic or mechanical) causes the interfacial area between the liquid and solid to increase beyond conditions of static equilibrium {Kistler, S.F. 1993}. For complete wetting and partial forced wetting systems one finds a good agreement with the hydrodynamic theory (fluid flow model). Examples of forced, partial wetting are given by {Ström, G., 1990}, {Guttoff, E.G., 1982} and {Douglas L.J., 1991}. Their experimental data are summarized by Kistler et al. {Kistler, S.F. 1993}. It was confirmed that the fluid flow model captures the dynamic wetting behavior of the authors' selected liquid/solid systems such as PTFE and untreated polystyrene as substrates and silicone fluids as liquids {Kistler, S.F. 1993}. The viscosity of the liquids varied from 2 mPa*s to 4.88 Pa*s. Examples of complete wetting systems are given by {Hoffmann, R.L., 1975}, {Fermigier, M., 1988}, and {Ngan, C.G., 1982}. Their experimental data are

summarized and compared with the fluid flow model by Kistler et al. {Kistler, S.F. 1993}. The systems investigated by the authors were silicon fluids displacing air in capillary tubes and between glass plates. The data gather near the universal curve of the fluid flow model. Especially for the low-speed range ($0.01 < Ca < 0.3$) the fluid flow model is able to fit the experimental data well {Kistler, S.F., 1993}. Thus, in these systems energy dissipation is expected to be due to the viscous flow in the liquid.

The agreement between experiments and theory for forced spreading (including partial and complete wetting systems) and spontaneous spreading for complete wetting systems indicate that a similar mechanism occurs in these systems. Namely, energy is dissipated during the spreading due to the viscous flow of the liquid {Kistler, S.F. 1993}. The same is expected for spontaneous, partial wetting systems as is shown by Hocking et al. {Hocking, L.M., 1982}. The authors studied the spreading kinetics of molten glass ($\text{SiO}_2\text{-NaO}_2\text{-TiO}_2$) on a polished platinum sheet. They compared their experimental data to a continuous model that considers a slip between the fluid and the solid boundary at the contact line to avoid a force singularity there. This model is based on hydrodynamic assumptions which were also used for the fluid flow model. Hocking et al. showed that their experimentally obtained data was consistent with their theoretical predictions. This, together with the fact that Cox proved theoretically that the macroscopic behavior of a liquid can be described with the fluid flow model without a specific cutoff mechanism leads to the assumption that the fluid flow model is valid for the system investigated by Hocking et al. Thus, in this spontaneous partial-wetting system the energy seems to be dissipated due to the viscous flow of the liquid.

3.2 Comparison of the molecular kinetic model and the fluid flow model with experiments in high-temperature systems

Lopez-Esteban et al. {Lopez-Esteban S., 2004} investigated the spreading kinetics of $\text{SiO}_2\text{-CaO-Al}_2\text{O}_3$ on polycrystalline Mo at an oxygen partial pressure of $> 10^{-14}$ Pa. Using a drop transfer set up the experiment was performed at 1200 °C. No reaction

between the glass and the metal was observed and also no interdiffusion at the glass/metal interface was detected with an SEM using EDS analyses. This system is a model system since the glass does not have any volatile components and is stable under a wide range of temperatures and oxygen partial pressures. The analyses of the spreading kinetics showed that the spreading velocity of the glass front is orders of magnitudes slower than expected for spreading controlled by viscous impedance (fluid flow model). Lopez-Esteban et al. {Lopez-Esteban S., 2004} were able to fit their experimental data to a theoretical model introduced by Blake et al. {Blake T.D., 1993}. In their theory they suggested that both viscosity and local dissipation at the triple line play a role in determining the wetting kinetics (molecular kinetic model). The viscous effect can be included in the molecular kinetic model. Two contributions to the wetting activation energy ΔG_W^* were defined: one comes from the liquid – solid ΔG_s interaction and the other from the viscous interaction in the liquid ΔG_{vis} {Blake T.D., 1993}:

$$\Delta G_W^* = \Delta G_s + \Delta G_{vis} \quad (3.1).$$

Therefore (2.29) transforms to {Blake T.D., 1993}:

$$v = 2 \left(\frac{kT}{h} \right) \exp \left(\frac{-(\Delta G_s + \Delta G_{vis})}{NkT} \right) \sinh \left(\frac{\gamma_{lv} (\cos \theta^0 - \cos \theta)}{2nkT} \right) \quad (3.2).$$

Using adsorption distances on the order of 1–4 Å the data of Lopez-Esteban et al. can be described by equation (3.2). The resulting wetting activities were approximately 230–300 kJ/mol. This is on the order of the viscous flow for glasses ($\Delta G_{vis} \approx 290$ kJ/mol). The wetting activity for glasses coincides with the wetting activation energy for viscous flow. The glass molecules around the triple junction are affected by interactions with the solid and the viscous interactions between the molecules themselves {Lopez-Esteban, S., 2004}. Viscous interactions between the glass molecules seem to be stronger than the interactions between the liquid molecules and the substrate. Therefore, the spreading of glass is controlled by the dissipation at the triple junction but the main contribution to the wetting activation energy is the activation energy for viscous flow {Lopez-Esteban S., 2004}. Similar observations were

made by Cherry and Holmes (Cherry, 1983) who investigated polymers with large viscosities (10^2 Pa*s).

Saiz et al. {Saiz E.,2003} studied the kinetics of high-temperature spreading in the system of liquid Sn-3Ag-xBi on Fe-42Ni. Sn3AgxBi is used as a lead free solder. The experiments were performed using a drop-transfer system at 450 °C and 250 °C under Ar+5 %H₂ gas flow. Spreading velocities between 0.5 and 0.01 m/s were observed. Even though this system is a reactive spreading system in which the liquid spreads while a chemical reaction occurs at the liquid-solid interface during the spreading, the observed velocities are so fast that they are consistent with spreading on a flat substrate. Saiz et al. showed that the estimated critical velocity for ridge growth is several orders of magnitude lower than the observed spreading velocities for this system. This supports the idea of spreading on a flat surface without ridge formation. The high velocities reported also preclude simultaneous spreading and growth of a reaction layer which is thicker than a few nanometers. Since the grains of the reaction layer do not grow in the direction of the triple line movement Saiz et al. assumed that spreading occurs on an unreacted surface. The spreading kinetics were compared with the fluid flow model and the molecular kinetic model. Both models were able to describe the experimental data but the fitting parameters from the hydrodynamic model were not reasonable. L_s resulted in zero which is not consistent with the fluid flow model. The parameters which resulted from the molecular kinetic model are more physically reasonable. The calculated adsorption sites are on the order of atomistic distances (0.1–1.0 nm). The calculated wetting energies are slightly higher than the activation energies for viscous flow and the reported molecular displacement frequencies are in the upper range of those reported for low-temperature wetting. All of this suggests that the rate-determining step is the movement of an atom from the liquid onto an adsorption site on a solid surface {Saiz E.,2003}.

3.3 Triple-line ridging in high-temperature wetting systems

Saiz et al. {Saiz, E., 1998} investigated triple line ridging in high-temperature systems, such as liquid metals (Al, Cu, and Ni) on Al_2O_3 and also liquid silicates (Si-Y-Al-O) on metals (Co, Mo, W). The experiments were performed with a sessile drop method in vacuum ($1.3 \cdot 10^{-4}$ Pa) as well as in gettered Ar. It could be shown that triple line ridging took place in the system of the liquid metals on Al_2O_3 and liquid silicates on metals and the ridge size was between 5 nm and 80 μm depending on the system {Saiz, E., 1998}. Triple line ridges of ~ 20 nm height were observed in the system SiO_2 -CaO- Al_2O_3 - TiO_2 on polycrystalline Mo {Lopez-Esteban S., 2004}

3.3.1 Pure Metals (Al, Cu, Ni) on Al_2O_3

Saiz and coworkers {Saiz, E 1998} performed experiments with pure metals (Al, Cu, Ni) on polycrystalline Al_2O_3 substrates. In the experiment Cu on Al_2O_3 , performed at 1150°C in gettered Ar, it was observed that the receding and advancing angles reach a common final angle of $\sim 114^\circ$ after 20–30 minutes {Saiz, E 1998}. Atomic force microscopy measurements were performed after removing the Cu drop from the Al_2O_3 substrate and ridges of 10-40 nm size were detected. The height h of the ridge is small compared to the radius of the droplet ($h/R < 10^{-4}$). Due to this and the fact that the receding and advancing angles reach a common value it was suggested by Saiz et al. that triple line ridging took place in the second regime. Therefore, the measured contact angle reached in Ar atmosphere is close to the Young's equilibrium angle. However, the experiments performed in vacuum showed a decrease in the final angle which can be explained as due to evaporation of the liquid copper. Ridges of 10–80 nm were observed. Even though the contact angle decreased, the drop stayed attached to the ridge since the angles still remained within the attachment range of equation (2.45) {Saiz, E., 2001}. Saiz et al. {Saiz, E., 1998} found undercutting close to the ridges, which was produced by liquid metals. This is a hint that the ridge was formed by local diffusion rather than by solution-precipitation. In the system Ni on polycrystalline Al_2O_3

performed at 1500 °C in gettered Ar ridges at the triple line of the size of 0.2 μm were found. Like in the system Cu on Al_2O_3 grain boundary grooving under the liquid drop was stronger than on the plain substrate. It was suggested that diffusion was the limiting transport mechanism {Saiz, E., 1998}.

Using equation (2.59) Saiz et al. {Saiz, E., 1998} estimated the ridge height. The resulting height of 90 nm for Cu on Al_2O_3 and 300 nm for Ni on Al_2O_3 is in the right order of magnitude considering that the fronts were not attached to a stationary ridge during the entire time.

As remarked earlier (see chapter 2.3.2) Saiz et al. observed that in the case of the spreading of liquid aluminum on sapphire at 1100 °C in vacuum the final angle oscillated periodically between 80° and 60°. This oscillation was attributed to evaporation of the aluminum which results in a decrease of the final angle. The contact angle is not within its attachment range (2.45) and the triple line will break away from the ridge. Levi et al {Levi G., 2003} investigated the morphology of micron-sized Al drops on sapphire substrates by dewetting a thin Al film from a sapphire surface at both 900 °C and 600 °C in an ultra high vacuum furnace in a controlled atmosphere. At 900°C they observed ridging as was also seen by Saiz {Saiz, E. 2001}. Levi et al. {Levi G., 2003} also showed that evaporation of the sapphire substrate atoms diffusing at the interface has an important role in the evolution of the Al– Al_2O_3 interface.

3.3.2 Liquid glasses on metals

Saiz et al. {Saiz, E 1998} observed ridges of 70–80 μm height at the triple junction of silicate glass on Co substrates at 1440 °C. Estimates made by Saiz {Saiz, E., 1998} showed that the ridge should be in the range of 1 μm if the ridge formation were attributed only to surface diffusion. Since the temperature used for the experiments was $\approx 0.9 T_m$ the yield stress in the metals is very low and creep effects can occur. Therefore, the huge ridge can most likely be explained as due to plastic deformation {Saiz, E 1998}. In the case of substrates with higher melting points (Mo, W) the observed ridges were much smaller given the same experimental conditions.

Triple line ridges of ~ 20 nm height were observed in the system SiO₂-CaO-Al₂O₃-TiO₂ on polycrystalline Mo {Lopez-Esteban S., 2004}. A drop-transfer experiment was performed at 1200 °C at an oxygen partial pressure < 10⁻¹⁴ Pa. At this pressure there will be a chemical reaction between the glass and the molybdenum



Lopez-Esteban et al. {Lopez-Esteban S., 2004} showed that the triple line ridging occurred due to interfacial diffusion, which was confirmed by the shape of the ridge which showed a hump on one side. The authors assumed that the liquid was spreading over a flat surface without any reaction. At slower spreading velocity a ridge forms either due to nucleation on defects in the substrate or because the critical range for ridge formation has been reached. When the ridge reaches a height of about 10 nm its speed is so slow that spreading of the liquid is stopped until the liquid can break away from the ridge. This behavior was confirmed by a characteristic stick-slip motion {Lopez-Esteban S., 2004}. The fact that the calculated steady state velocity v_{ss} for a 20 nm ridge is much slower than the observed spreading velocity proves the fact that the liquid front is not attached to the ridge and does not move with the velocity of the ridge {Lopez-Esteban S., 2004}. Thus the speed of the liquid is not controlled by ridge movement. When the spreading slows down or stops reaction products will nucleate at the triple junction. Islands of the reaction product Mo₃Si (tens of microns wide and less than 1 μm thick) were observed in a narrow band (~ 100 μm wide) around the triple junction.

So far the common understanding of reactive spreading in high temperature systems was that the reaction product and the liquid front advance together {Eustathopoulos N., 1998}. Eustathopoulos et al. found that reaction-limiting spreading occurred with pure Al on vitreous carbon under high vacuum conditions at a temperature of 1100 K performed with a sessile drop configuration. In this system, wetting is promoted by the formation of a continuous reaction layer of aluminum carbide {Eustathopoulos N., 1998}. The rate of spreading is limited by the lateral growth of the reaction layer. Reaction limiting spreading was observed for different kind of reactions in different systems such as CuSi alloys on oxidized SiC, CuAg-Ti/Al₂O₃, or CuSi on vitreous carbon {Eustathopoulos N., 1998}. However, Lopez-

Esteban et al. and Gremillard et al. showed that the reaction product and the liquid front do not always advance together. A theory about reactive wetting should start dividing the wetting process into its different steps as fluid flow, adsorption, ridge formation, and reaction processes {Saiz, E., 2000}. The kinetics of each step need to be determined in order to be able to decide which step is crucial for the spreading kinetics {Saiz, E., 2000}. In most glass/metal systems the reaction process does not determine the spreading process but instead the mechanisms which control the kinetics in the non-reactive case are important {Lopez-Esteban S., 2004}.

3.3.3 Liquid metal alloys on ceramics

Gremillard et al. {Gremillard L., 2004} investigated the wetting of Sn–Ag based alloys on Al_2O_3 . Sessile drop experiments were performed at temperatures between 600 °C - 1000 °C under vacuum at pressures which ranged from 10^{-4} to 10^{-3} Pa. Due to the addition of small amounts of Ti (1 wt.%) a decrease in the final contact angle from 150° to 25° was observed {Gremillard, L., 2004}. Eustathopoulos et al. {Eustathopoulos, N., 1998} suggested that the addition of reactive elements such as Ti and Cr to the liquid alloy improve the wetting on ceramics due to an interfacial reaction layer. However, the improvement in the wetting behavior of the tin-silver based alloys on Al_2O_3 is not attributed to a formation of a continuous reaction layer at the metal-ceramic interface {Gremillard L., 2004}. At temperatures below 800 °C small angles were observed but no reaction occurred. At temperatures higher than 800 °C no continuous reaction layer formed but islands of the reaction product close to the triple line were detected. Therefore, Gremillard et al. {Gremillard L., 2004} suggested that there is a finite nucleation barrier for the reaction phase formation and the liquid front and the reaction product do not extend together. This supports the theory of Saiz et al. {Saiz, E., 2000} which focuses on the adsorption of the reactive element at the solid–liquid interface before the reaction can take place. The rate determining process for wetting would then not be the formation of a reaction layer. Furthermore, the decrease in contact angle could be explained by these adsorption effects. Derby et al. {Derby B., 2001} have

shown that Ti segregates at the metal-ceramic interface in the system Sn–Ti/Al₂O₃. They did not observe any reaction product at the interface.

The spreading kinetics of the Sn–Ag based alloys on Al₂O₃ can not be explained with the fluid flow model nor with the molecular kinetic model {Gremillard, L., 2004}. The observed slow spreading kinetics as well as the large variability in contact angles were attributed to the kinetics of dissolution into the liquid and the formation of triple line ridges. The starting alloy consists of a homogeneous distribution of Sn₅Ti₆ pallets that dissolve into the liquid. The difference in the observed contact angles was attributed to the different amounts of Ti dissolved into the liquid. Triple line ridges which nucleated due to local diffusion processes or solution precipitation stopped the liquid and contributed to the wide variability of the contact angles {Gremillard, L., 2004}.

3.4 Wetting behavior of liquid metals on metals for systems with negligible mutual solubility

Several authors have investigated the wetting of liquid metals on metal substrates for systems with negligible mutual solubility {Tomsia, A.P., 1982}, {Pique, D., 1981} {Sugita, T., 1970}, {Yupko, V.L., 1991} {Yupko, V.L., 1986} as the system (liquid Ag on Mo) used in this work. The works did not especially concentrate on the investigation of ridge formation or on the spreading kinetics in those systems. Thus those experiments are of minor importance for this work. Tomsia et al. {Tomsia, A.P., 1982} investigated sessile drop experiments of Ag on Fe at 1000 °C and oxygen partial pressures of 10⁻⁵ and 10⁻¹⁵ Pa. They showed that the contact angles and therefore the surface energies of Fe are sensitive to the degree of saturation with oxide and to the degree of chemisorption of oxygen. The chemisorption of oxygen depends on the activity of oxide in Fe and the p(O₂) in the ambient atmosphere. Pique et al. {Pique, D., 1981} also investigated the system liquid Ag on Fe in a reducing Ar/5 %H₂ atmosphere. They found that the contact angle decreased with increasing temperature and explained this temperature dependence by the adsorption of Ag atoms at lower temperatures which

will be desorbed with increasing temperature. Thus, the γ_{sv} will increase and θ will decrease with increasing temperature.

Sugita et al. {Sugita, T., 1970} performed sessile-drop experiments of liquid Ag on W at 960 °C and 1200 °C and of liquid Au on W at 1063 °C under a total pressure in the system of 1×10^{-17} Pa. With the given surface energies of the liquid and the measured contact angles the authors calculated with equation (2.1b) interfacial energies of about 2500 erg/cm² for Au/W and 2700 erg/cm² for Ag/W.

Yupko et al. {Yupko, V.L., 1986} investigated the wetting of liquid Cu on Mo at temperatures between 1370 °C and 1670 °C. The experiments were performed with a drop transfer system in a He and a He+18 %H₂ atmosphere. The time dependence of the contact angle θ shows that the stable values of θ are established within seconds for both atmospheres. However in a He atmosphere wetting is considerably poorer than in He+18 %H₂ atmosphere. This is due to the higher oxygen content in the He atmosphere. Oxidation of the substrate surface results in higher contact angles in the experiments performed under He.

4 Experimental details

4.1 Wetting experiments

4.1.1 Wetting furnace

The drop transfer experiments are performed in a side-loading vacuum furnace (series 15, CENTORR Vacuum Industries, Nashua, NH, USA). The equipment consists of five separate parts (Figure 4.1): (a)¹ the furnace chamber, (b) a gas manifold, (c) an oxygen analyzer, (d) the control unit (temperature and vacuum regulation) and (e) the vacuum system.

The furnace chamber (a1) is cylindrical, double walled, and made of stainless steel. The heat is provided by a cylindrical tungsten heating element (a2). The chamber is shielded from the heat of the heating element by a set of cylindrical molybdenum shields (a3). In addition, the rear (a4) and top (a5) panels of the chamber are water cooled. The work platform (a6), which is made of tungsten, is placed in the center of the heating element. The Mo sample holder (a7) can be lowered during the experiment due to a vacuum-proof adjustable manipulator (a8). A transparent quartz window (a9) in the front panel of the furnace allows for the observation and recording of the wetting experiments. The temperature inside the chamber is measured with a W5%Re/W26%Re thermocouple sheathed with molybdenum (a10). The thermocouple is placed below the

¹ symbols (a1)-(a10), (b)-(e) refer to figure 4.1

4 Experimental details

working platform. The maximal working temperature of the furnace is 2000°C. The furnace can be operated under vacuum as well as under flowing gases.

An important feature of the furnace is the gas manifold (b) which allows the use of up to three different reaction gases in different mixture ratios. Hence, one can adjust the O₂ partial pressure by adjusting the gas proportions. The measurement of the oxygen concentration of the gas leaving the furnace is done with a yttrium stabilized ZrO₂ oxygen analyzer (Centorr 2D/220) (c). The temperature control is performed with a digital controller (UDC 3000, Honeywell, Phoenix, AZ, USA) (d).

The vacuum pump system (e) is connected to the furnace chamber. The primary vacuum is ensured by a mechanical pump (Leybold D8B). A turbo molecular pump (Leybold TMP-50) enables a vacuum pressure as low as $6 \cdot 10^{-5}$ Pa to be reached.

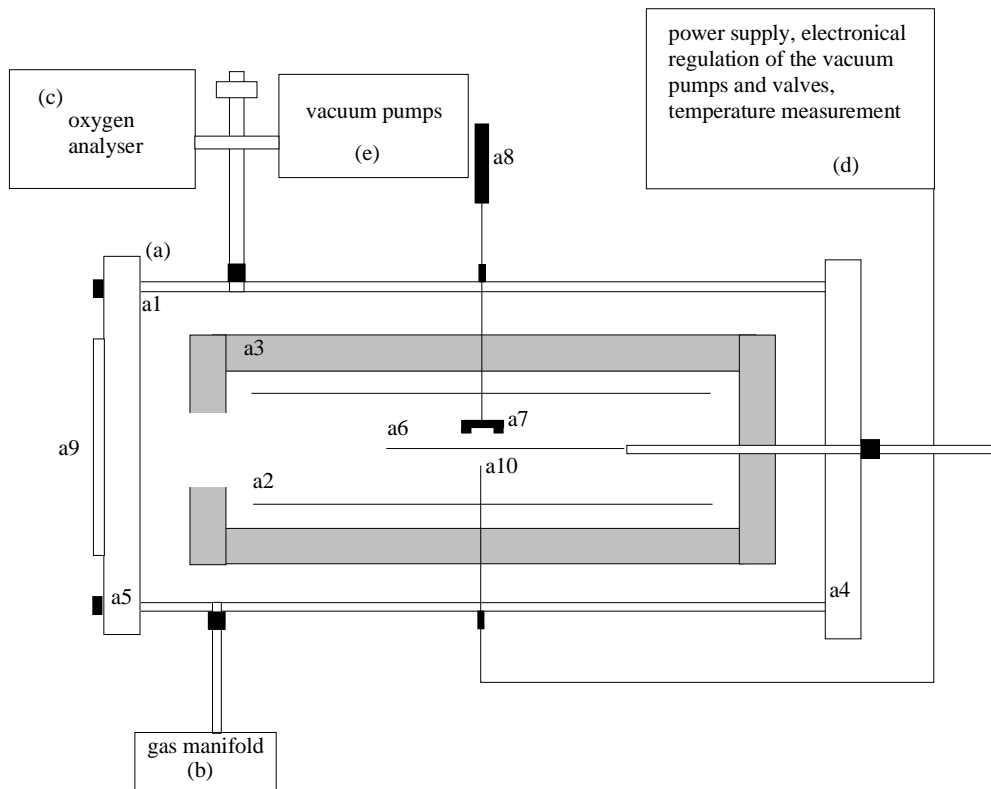


Figure 4.1: Schematic drawing of the vacuum furnace.

4.1.2 Parameters of the wetting experiment

The spreading of liquid Ag on polycrystalline Mo substrates was investigated using a drop-transfer setup inside the induction furnace described in section 4.1.1. The experiments were performed in Ar + 1% H₂ and Ar +5% H₂ flowing at $\sim 2 \cdot 10^{-5}$ m³/s [$p(\text{Ar}) \approx 10^5$ Pa]. For all the experiments using Ar + 1% H₂, the oxygen content in the gas was kept below 10⁻¹⁴ ppm [$p(\text{O}_2) < 10^{-20}$ atm]. For all the experiments using Ar + 5% H₂, the oxygen content in the gas was kept below 10⁻¹⁶ ppm [$p(\text{O}_2) < 10^{-22}$ atm]. The drop-transfer spreading experiments were performed using the following procedure: A small piece of Ag (~ 0.01 – 0.02 g) was placed on a sapphire single crystal surface inside the furnace. There is no reaction between the sapphire and the Ag during the heating phase. Ag does not wet sapphire and exhibits an obtuse contact angle with the sapphire substrate. The Mo substrate was placed on a Mo holder ~ 10 – 15 mm above the molten Ag drop. Subsequently, the furnace was evacuated to a pressure of $\sim 6 \cdot 10^{-4}$ Pa and refilled with gas (Ar + 1% H₂ or Ar + 5% H₂). The gas was allowed to flow for ~ 2 h before heating in order to assure that the required $p(\text{O}_2)$ was reached. The gas flow used was 2×10^{-5} m³/s. The assembly was heated at 15 °C/min to the required wetting temperature (970 °C, 1070 °C, 1150 °C, 1290 °C) When the wetting temperature was reached the Mo substrate was lowered from the top and placed in close proximity to the liquid surface (~ 1 mm or less). In the case of the equilibrated experiment the assembly was maintained at this distance and temperature for 1 h. Afterwards, the substrate was lowered slowly until it just touched the drop surface and the liquid spread on it, transferring from the sapphire plate to the Mo. In the case of the non-equilibrated experiments the wetting experiment was performed as soon as the wetting temperature was reached.

The drop transfer experiments of Ag on single crystalline Mo(110) and (100) were performed at 970 °C, 1070 °C, 1150 °C, and 1290 °C using Ag/5% H₂. In both cases only equilibrated experiments were performed.

The spreading of receding liquid fronts was analyzed by placing a thin foil of the alloy on top of the Mo substrate. The assembly was heated to the test temperature under the same conditions described above.

4.1.3 Recording and analysis of the dynamic contact angle

The dynamic contact angles were recorded *in situ* by observations through the transparent quartz window ([a9] in Figure 4.1). The spreading was recorded using a high-speed motion analysis system (Kodak, series SR) with a digital camera able to acquire up to 2000 frames per seconds for a period of 2 seconds. The final angle as well as the long-time behavior of the drop was recorded with a CCD camera (Sony XC-73) controlled by the software DropImage (Rame Hart Inc., Mountain Lakes, NJ, USA), which is able to take 1 frame per second for several hours.

The DropImage software includes a module for automatic determination of the contact angles and surface energies. However, this feature necessitates very sharp and clear pictures which can only be obtained with transmitted light. Because of the configuration of the furnace (only 1 quartz window), reflected light had to be used leading to less clear images. In order to measure the angle with more precision a new program was developed by L Gremillard {Gremillard, L., 2004} in the group of A.P. Tomsia, Berkeley, CA, USA.

The advantage of this program is that all images which are recorded during an experiment are readily accessible. They can be opened with an automatic image treatment software (for contrast, brightness, and gamma enhancement). The measurement of the contact angles is fast and precise and the storage of the data is easy. The time required to measure one angle is less than 10 s on average. Figure 4.2 shows the typical program interface, including an image of a liquid drop on a substrate as it is recorded with the low-speed camera.

The measurement is based on placing several characteristic points on the image, which depend on the chosen fitting methods. In this work the so-called Photoshop fitting method was used. Three different points are required, which are points 1–3 in Figure 4.3; these points are chosen to determine a triangle of which the base a is the length of the drop-substrate interface, and the edge b is a tangent to the drop. Using these points the software calculates the contact angle applying equation (4.1). The angle θ results to:

4 Experimental details

$$\theta = \frac{\pi}{2} - \arcsin\left(\frac{a^2 + b^2 + c^2}{2ab}\right) \quad (4.1)$$

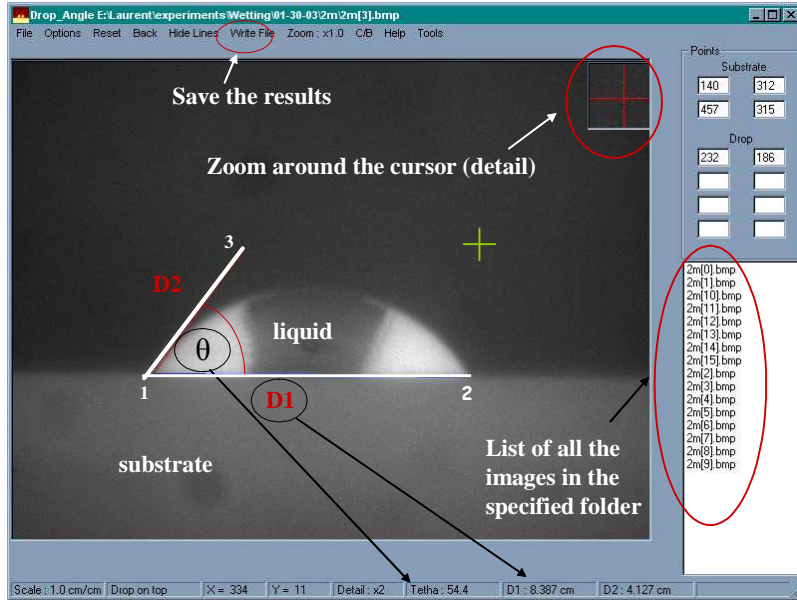


Figure 4.2: Computer interface of the drop image program. The liquid drop is placed on the solid substrate. D1 is the base radius, θ the contact angle {Gremillard, L., 2004}.

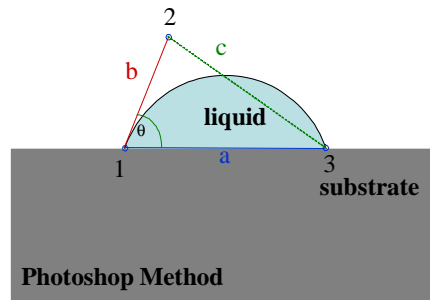


Figure 4.3: Determination of the contact angle with the “Photoshop method” {Gremillard, L., 2004}

4.2 Investigations of the microstructure

4.2.1 Scanning Probe Microscopy (SPM)

Scanning probe microscopy is based on the following principle: a sharp tip is brought into close contact with the surface of a sample and an interaction (force tunneling current etc.) between the tip and the surface of the sample, which strongly depends on the distance between them, is measured {Wiesendanger, R., 1994}.

The interaction is measured while the tip scans the surface line by line. One mode to operate the SPM is to keep the interaction between the tip and the surface constant and recording the reaction of the tip due to changes of topography of the surface.

The most frequently used scanning probe microscopes are the scanning tunneling microscope (STM) and the atomic force microscope (AFM). The interaction of the tip and the surface in STM is related to tunneling effects. If a voltage is applied between the tip and the surface, electrons can tunnel either from the tip into the sample or vice versa. STM is used with conductive materials. In the AFM case the interaction between the tip and the surface arises from intermolecular forces. These can be Van der Waals, magnetic, electrostatic, friction and capillary forces. Depending on the distance between tip and sample the forces can be attractive or repulsive forces. The AFM can be used also for non-conductive samples.

The topography of a surface can be determined by the AFM due to the strong distance dependence of these forces. A tip is mounted on a cantilever. If the tip is brought into close contact with the surface of the sample, the cantilever will bend by an amount dependent on the strength of the force. The force results in:

$$F = \frac{E}{4} \frac{wt^3}{L^3} \Delta z \quad (4.2)$$

where E is the Young's modulus, L the length of the cantilever, w is the width and t is the thickness of the cantilever and Δz the distance between the tip and the sample. The bending of the cantilever can be measured with a laser beam, which is reflected on the top of the cantilever and is collected by a 4-quadrant photodiode array (Figure 4.4).

4 Experimental details

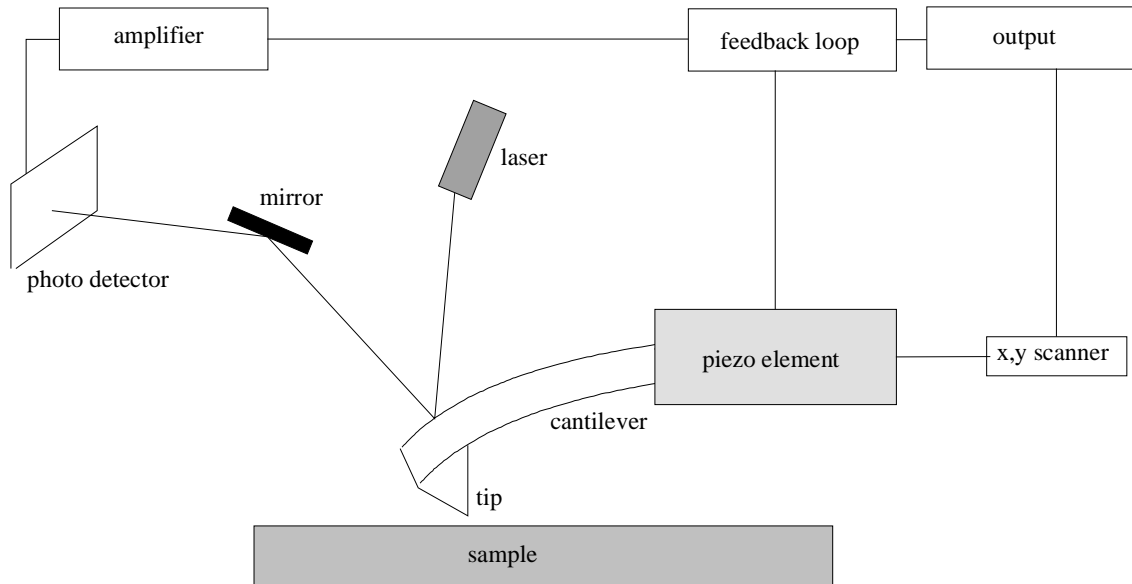


Figure 4.4: Measuring principle of Atomic Force Microscopy, taken from {Richter, G. 2000}

Depending on the force and thus the distance between tip and surface one differentiates between different working modes: the non contact mode, the tapping mode and the contact mode. Figure 4.5 shows the dependence of the intermolecular forces on the distance between tip and surface of the sample. In the case of the contact mode the tip touches the surface and repulsive forces dominate, as shown in Figure 4.5. The mean repulsive force is about 1 nN. In the non contact mode and the tapping mode, attractive forces are present. Independent of the mode the measurement is performed either by a constant force or constant height.

In the case of applying a constant force, the bending of the cantilever is kept constant. The voltage of the z-piezo is regulated by a feedback loop in order to maintain the bending constant. The voltage of the piezo is related to the topography of the

surface. In the case of applying a variable force, the voltage of the piezo is kept constant and the bending of the cantilever is measured via the photodetector.

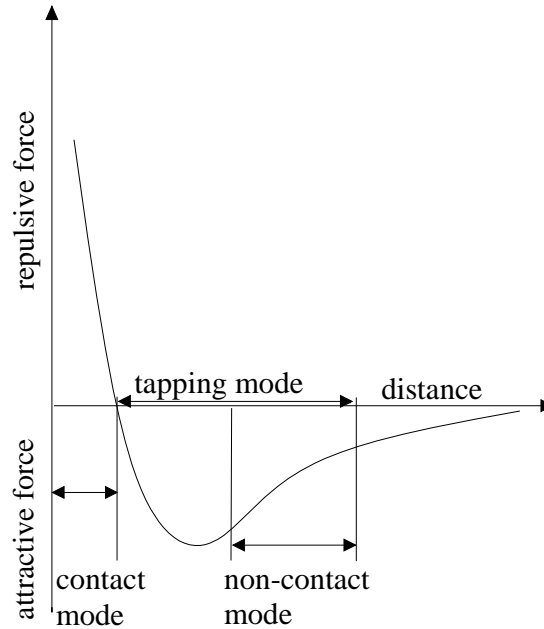


Figure 4.5: Dependence of the intermolecular forces on the distance between tip and surface, courtesy of {Schöllhammer J.1998}

In the present work AFM measurements were performed with a TriboIndenter with AFM option (Hysitron Corp) in Berkeley and a Scanning Probe Microscope TMX 2000 (Topometrix) in Stuttgart. The TriboIndenter with AFM runs with software from Quesant. The X-Y scan range of the AFM is $40\ \mu\text{m} \times 40\ \mu\text{m}$, the X-Y resolution of this system is $7\ \text{\AA}$, and the resolution in Z-direction is $0.7\ \text{\AA}$. The TMX 2000 runs with software from Thermomicroscopes. The X-Y scan range of the AFM is $100\ \mu\text{m} \times 100\ \mu\text{m}$, the resolution in Z-direction is $0.7\ \text{\AA}$ {TMX 2000, Users Manual}. The measurements were performed in the contact mode keeping the force constant. The tip is a small pyramid made of silicon nitride.

4.2.2 Scanning Electron Microscopy (SEM)

The SEM investigations were performed with a high-resolution field emission SEM (JEOL 6300F), which is equipped with a Schottky emitter. The electrons are accelerated by an electric potential in the range of 1-40 kV. A condenser lens projects the image of the source onto the condenser aperture (Figure 4.6). The beam is then focused by the objective lens onto the surface and scanned across the surface using scanning coils. When the primary electrons hit the sample surface, they transfer a part of their energy through inelastic scattering to the electrons in the sample resulting in the emission of secondary electrons. These secondary electrons can have energies up to 100 or 200 eV but typically are in the range of 10-50 eV. Their low kinetic energy restricts their mean free path in the sample, so that secondary electrons escaping from the sample are generated close to the surface, typically within 1-2 nm. This leads to the possibility of probing the sample surface. The secondary electrons are collected by a detector and their intensity is displayed versus the position of the primary beam on the sample. Besides the secondary electrons, there are also backscattered primary electrons. The average energy of the backscattered electrons is less than the primary incident beam but of the same order of magnitude. This imaging mode gives good material contrast but is less surface sensitive since the penetration depth of the backscattered electrons is in the range of some 100 nm. More detailed information is given in {Schmidt, P.F., 1994} and {Brandon, D., 1999}.

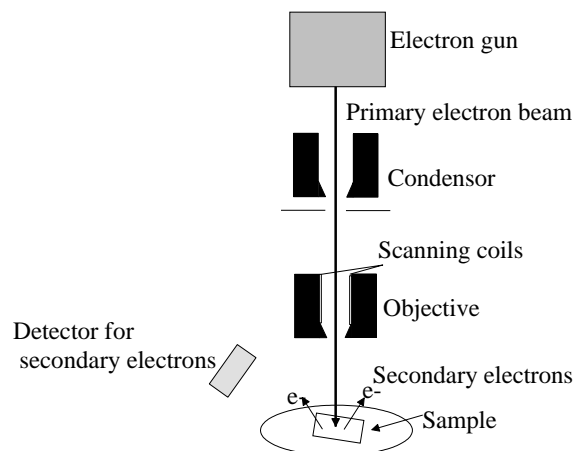


Figure 4.6: Schematic drawing of a scanning electron microscope (SEM), taken from {Butt, H.J., 2003}

4.2.3 Transmission Electron Microscopy (TEM)

Conventional Transmission Electron Microscopy was performed with JEOL 2000 FX and JEOL 4000 EX microscopes. In contrast to the methods described above, TEM is not surface-sensitive. It was used in this work in order to investigate the interface between the Ag and the Mo substrate. A short summary only of the fundamentals of the TEM is given here. More detailed information on the design of a TEM and its applications is given in {Heimendahl, M. 1970}, {Williams, D, Carter, C., 1996} and {Brandon, D., Kaplan W., 1999}.

A heated W-filament, LaB₆-cathode, or a field emission cathode is used to generate an electron beam. The electrons are accelerated by an electric potential in the range of typically 100-400 kV. A Wehnelt-cylinder and a condenser lens system focus the electron beam onto the sample. Interaction processes between the electrons of the electron beam and the sample occur which are used for imaging. The scattered electrons which are transmitted through the electron transparent specimen pass through the objective lens and form an image in the image plane. A diffraction pattern is generated in the back focal plane of the objective lens, where an objective aperture can be inserted. Depending whether the transmitted or a diffracted beam passes through the objective aperture either a bright field image or a dark field image is generated. This is illustrated in Figure 4.7.

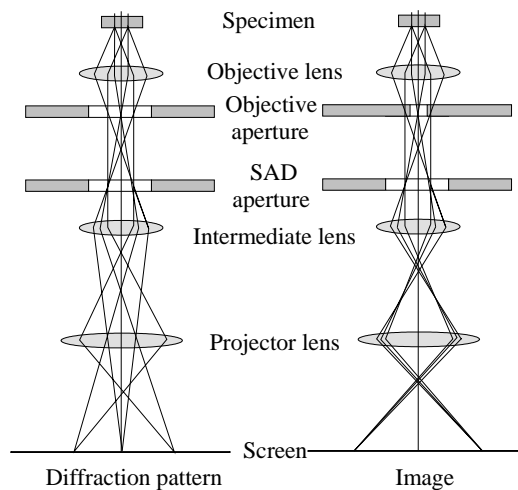


Figure 4.7: Schematic drawing of a TEM illustrating how diffraction pattern and bright field images are generated, taken from {Heimendahl, M., 1970}

4.2.4 Auger Electron Spectroscopy (AES)

The Auger investigations were performed with a JEOL JAMP-7830 F Auger Electron Spectrometer. In Auger electron spectroscopy (AES) the sample of interest is irradiated with an electron beam. These electrons typically have an energy of about 1-5 keV. The incident electron ejects an electron from the inner electron shells of the atoms of the sample, and an empty state is created. An electron in a higher shell then fills the empty state and energy is released, either as a characteristic X-ray photon or a secondary electron. The secondary electron, which is ejected from a higher shell, is called an Auger electron (Figure 4.8). Its kinetic energy is dependent only on the energies of the electron levels involved and is therefore discrete and characteristic of the elements present at the surface of the sample. When analyzed as a function of energy, the peak positions are used to identify the elements. Usually Auger data are presented as a differentiated signal to enhance the visibility of the peaks present. The depth of analysis is about 3-5 nm. More detailed information about Electron Spectroscopy is given in {Seah, M.P., 1988}.

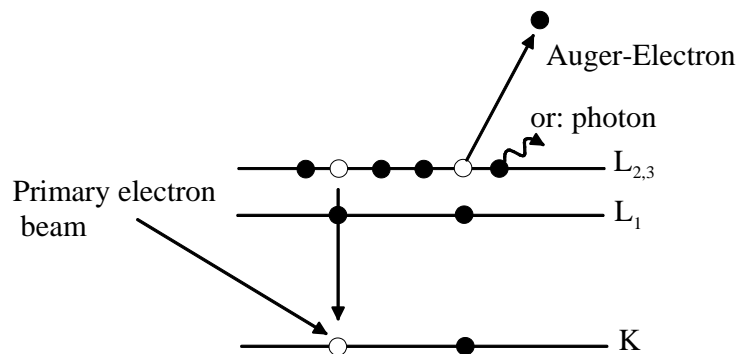


Figure 4.8: A primary electron beam ejects an electron of an inner electron shell of an atom to an unoccupied state or above the ionisation level. An electron in a higher shell fills the unoccupied state and energy is released. The energy can be released by emitting a photon or an Auger electron

4 Experimental details

5 Sample preparation

5.1 Sample preparation of the samples used for the wetting experiment

5.1.1 Polycrystalline and single crystalline Mo

In order to ensure minimum roughness of the Mo substrates in the wetting experiments, they were annealed and polished according to the following procedure:

Prior to the wetting experiments, the polycrystalline Mo substrates (99.9 %, Aldrich, USA, ~10 x 12 mm, 1 mm thick) were annealed at 1350 °C for 15min in order to recrystallize the Mo. The polycrystalline and single crystalline Mo (1cm diameter) were ground with 450µm SiC paper in order to remove the grain boundary grooves that formed during the heat treatment in the case of the polycrystalline Mo. Afterwards they were electrolytically polished. The electrolyte used was a mixture of 875ml of methanol (99.8%) and 125ml H₂SO₄ (95-97%). The H₂SO₄ had to be added to the methanol carefully in drops. For the electrolytical polishing a polishing machine from the company Struers LektroPlol 5 was used. The polished area was a circle of 0.9 cm diameter. The polishing temperature was 20-22 °C. A voltage of 18 V and a flow rate of 7, in the case of the polycrystalline Mo substrates, and between 4 and 5 for the Mo single crystals were applied. The polishing time was 90s. For each polishing cycle 600ml of the electrolyte was used. It was important that the contact arm was kept clean and the polishing mask was in proper contact with the sample. The electrolyte had to be

5 Sample preparation

prepared fresh for each polishing cycle. In each polishing cycle 10 samples could be polished.

Ag as well as Mo substrates were cleaned with acetone and ethanol in an ultrasonic bath and dried with an air gun.

5.2 Properties of the materials used for the wetting experiment

5.2.1 Optical emission spectrometry (ICP-OES) investigations

The compositions of the Mo substrates were determined by ICP-OES investigations and they are listed in Table 5.1. Those of the Ag used in the wetting experiments are listed in Table 5.2.

Table 5.1: Comparison of the composition of the polycrystalline Mo and single crystalline Mo(110) substrates determined with ICP-OES.

	Cr	Ca	Fe	Cu	Mg	Ni	Zn	Zr
Single crystal	<0.001	~0.006	~0.005	~0.015	<0.0001	~0.005	~0.002	~0.007
Poly crystal	<0.001	<0.002	<0.001	<0.001	<0.0001	<0.001	<0.0005	<0.001

Table 5.2: Determination of the Ag composition by ICP-OES

Sample	Cu	Cd	Ni	Pb	Pd
Ag	~0.03	<0.0002	<0.0005	<0.002	<0.002

5.2.2 Orientated Imaging (OIM) investigations

In order to get more detailed information about the polycrystalline Mo surface such as grain size and orientation, OIM measurements were performed. The average grain size is between 21-43 μm . Table 5.3 shows the quantitative analyses of the orientations of the

5 Sample preparation

grains with an error of 15°. About 50 % of all the grains have a (311) orientation with an error of 15°. There are only few grains with a (110) orientation for the different Mo substrates.

Table 5.3: Distribution of Mo grains of different orientations on the polished Mo surface

Sample	(111)	(100)	(110)	(311)
Mo (after annealing for 1h at 1070 °C)	27,9%	19,4%	3,0%	55,9%
Mo, (after annealing for 1h at 1070°C)	18,1%	22,8%	2,4%	53,7%

5.3 Sample preparation for microstructure investigations

5.3.1 Scanning Electron Microscopy

In order to prepare cross-sections of the Ag-Mo sample for the SEM investigations, the sample was coated with Cr to protect it against mechanical abrasion and also to protect the triple line. The samples were first cleaned in ethanol and dried with argon gas. The Cr was sputtered under an argon partial pressure of $4,9 \cdot 10^{-6}$ mbar and a power of 150W for 30 minutes. A 1µm thick chromium layer was grown. The Ag-Mo sample was cut with a (precision) diamond wire saw in a 700 µm thick slice and glued (G1 glue and graphite in order to make the glue harder) in a ceramic tube used for TEM preparation. Afterwards the tube was cut with a (precision) diamond wire saw in 400 µm thick slices. The slices were glued on a glass plate and put in a holder in order to grind and polish the sample. The cross-section was ground with silicon carbide paper up to 2000 µm and afterwards polished with 3 µm diamond suspension. The final polishing was performed with a 0.5 µm silicon dioxide suspension for one hour. The samples were then investigated by a field emission SEM microscope (JEOL6300F) with an operating voltage of 3 kV. The first attempts of polishing a cross-section failed. As shown in Figure 5.1 the triple line is completely destroyed. It seems that Mo grains

5 Sample preparation

broke off and covered the triple line. Ag is very soft and it smeared out during the polishing. It seems that for the mechanical polishing the Cr coating layer is problematic since Cr broke off during grinding. Since the cross-section prepared in such a way was insufficient the samples were re-polished again: grinding with 2000 μm , then polishing with 3 μm diamond suspension, and finally polishing with 0.5 μm silicon dioxide. Figure 5.2 shows the re-polished cross-section. Investigations of the polished surface now allow detection of the triple line.

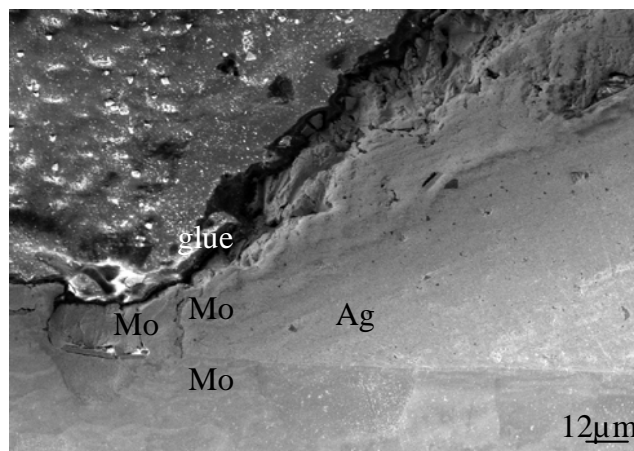


Figure 5.1: Cross-section of Ag on polycrystalline Mo, wetting experiment performed at 1070°C annealed for one hour and quenched afterwards. A clear interface between the Mo and the Ag is not visible. Mo grains broke off and covered the triple line.

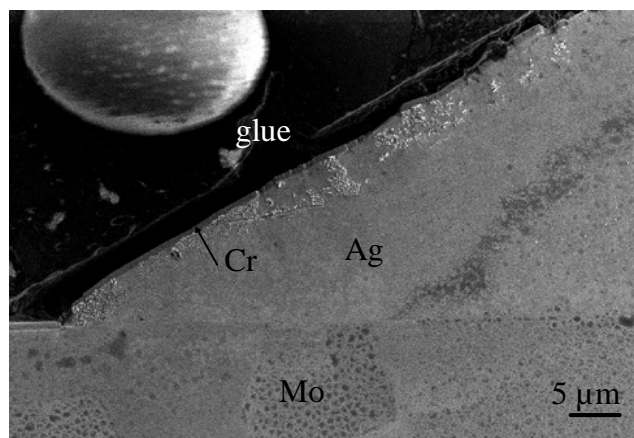


Figure 5.2: Improved cross-section of Ag on polycrystalline Mo The experiment was done at 1070°C, kept at this temperature for one hour and quenched afterwards. The cross-section still shows inhomogeneties which are due to the sample preparation.

5.3.2 Transmission Electron Microscopy

TEM samples were prepared at a focused ion beam work station 200 from the company FEI. The surface of the Ag-Mo sample was sputtered with a chromium layer in order to protect the triple line of the sample. Thus, the sample was protected against shadow effects in the FIB and diffusion of the Gallium ions from the ion beam. Due to the Cr-coating it was not necessary to coat the sample with tungsten or platinum as is usually done for FIB investigations. For the cross-section an area of $173\mu\text{m}^2$ was cut with an acceleration voltage of 30kV and an ion beam current of 2.7nA. The cleaning cut was done with an acceleration voltage of 6kV and an ion beam current of 12pA. The cross-section in Figure 5.3A of the Ag-Mo sample shows a clear interface between Ag and Mo. A TEM lamella Figure 5.3B was cut out of the sample using the focussed ion beam and put with a micro tweezers on a copper net, shown in Figure 5.4. The TEM lamella can easily be destroyed by removing the sample with the micro tweezers. An example is visible in Figure 5.5.

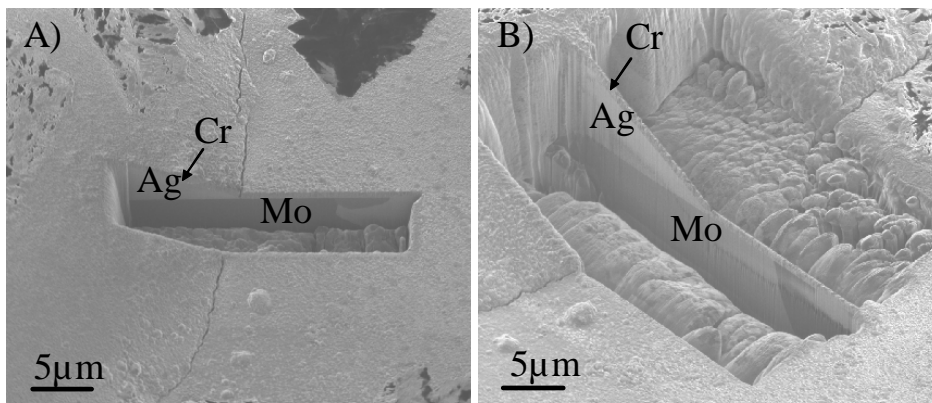


Figure 5.3: Illustration of a FIB cross-section cut through a Ag-Mo sample (A). The interface between Ag and Mo is clearly visible. To protect the sample against Ga ion diffusion the sample was coated with Cr. In B) a TEM lamella is cut with the focus ion beam work station

5 Sample preparation

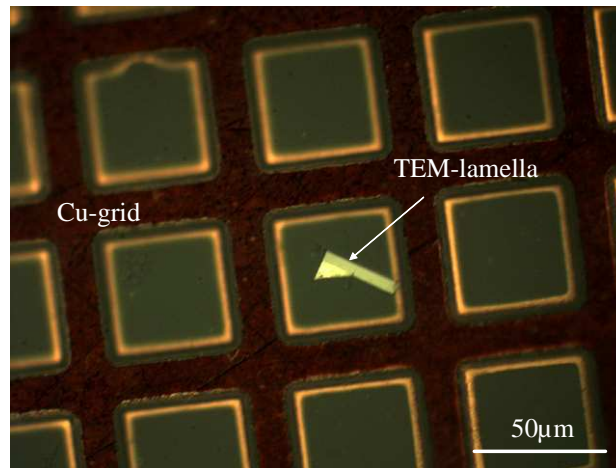


Figure 5.4: A TEM-lamella which was cut with the FIB is placed on a copper-grid

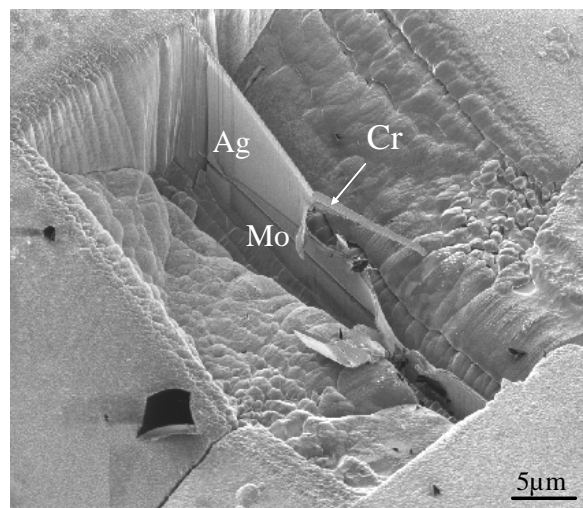


Figure 5.5: Due to the lifting with the micro tweezers the TEM lamella, which was cut in the FIB was destroyed

6 Experimental results

This chapter describes the spreading kinetics of liquid Ag on polycrystalline and single crystalline Mo at four different temperatures. Furthermore, the influences of equilibration of the system, roughness of the Mo substrate and ridge formation on the kinetics of spreading were investigated.

6.1 Spreading kinetics

6.1.1 Spreading kinetics of liquid Ag on polycrystalline Mo

The change of contact angles and droplet radii for Ag on polycrystalline Mo in Ar/5 %H₂ atmosphere were measured as a function of time. The time dependence of the wetting angle (Figure 6.1A) shows a strong decrease in the contact angle at the beginning of the wetting experiments up to about 0.005 s. Spreading velocities $v=[dR(t)/dt]$ between 0.1 and 0.6 m/s were recorded. When the contact angle is close to its final value, oscillations in the contact angle can be seen (Figure 6.1 A and 6.1.B). Figure 6.1C showing successive images taken with a high speed camera of a Ag drop on a Mo substrate, reveals the oscillations around the equilibrium angle and radius. The same effect has been observed by other authors and it is regarded as being due to inertia {Eustathopoulos, N., 1999}.

The final angle decreases with increasing temperature for the case of Ar/5 %H₂ atmosphere (Figure 6.2) and increasing H₂ content in the atmosphere (Figure 6.3). In the following only experiments which were performed under Ar/ 5%H₂ gas flow are presented.

6 Experimental results

The dimensionless spreading rate $Ca(t) = \eta[dR(t)/dt]\gamma_{LV}$ was calculated using $\eta \approx 0.004 \text{ Nsm}^{-2}$ and $\gamma_{LV} \approx 0.9 \text{ Jm}^{-2}$ {Smithells, C.J., 1976}. The contact angle was then plotted as a function of Ca and the results are shown in Figures 6.4-6.7. With the dimensionless and normalized value of Ca the spreading rates of different material systems with different values of viscosity and surface energy can be compared. Figures 6.4-6.7 show that the capillary numbers-angle dependency is similar for the different temperatures. The capillary number decreases with decreasing dynamic contact angle. As the dynamic contact angle approaches the final angle, the velocity of the drop and thus the capillary number is reduced. If the contact angle reaches its equilibrium, the velocity of the drop and therefore the capillary number become zero. The oscillations in the final angle at low velocities can be seen to be especially pronounced in Figure 6.5.

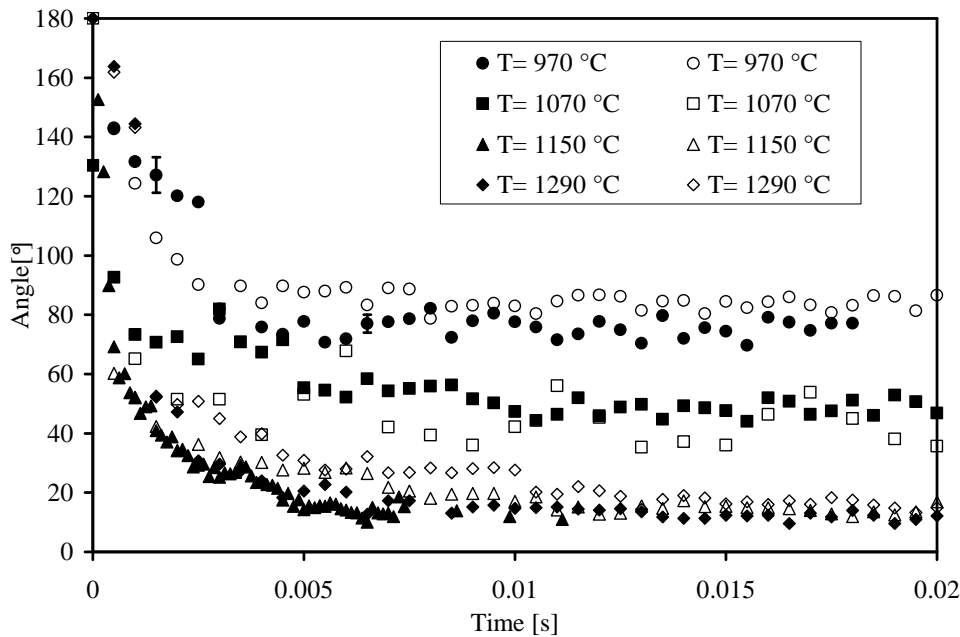


Figure 6.1A: Evolution of the advancing contact angle with time during the spreading of Ag drops on polycrystalline-Mo substrates at different temperatures. Two experiments at each temperature were performed which are presented as open and solid symbols.

6 Experimental results

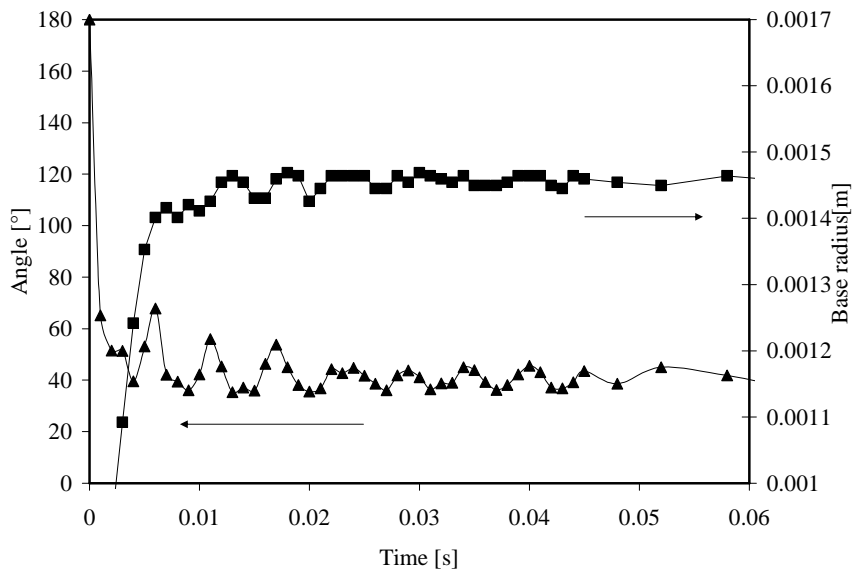


Figure 6.1.B: The dependence of the base radius and angle for liquid Ag on polycrystalline Mo at 1070°C shown. Oscillations in the base radius as well as the contact angle can be seen when they are close to their equilibrium values.

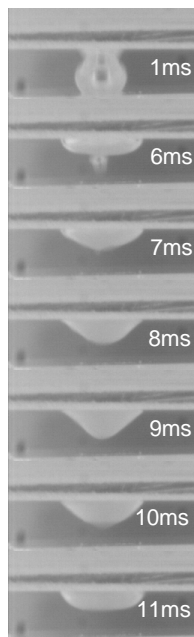


Figure 6.1.C: Successive images taken with a high speed camera of an Ag drop on a polycrystalline Mo substrate at 1070°C. Oscillation in the base radius as well as the contact angle can be seen when they are close to their equilibrium values.

6 Experimental results

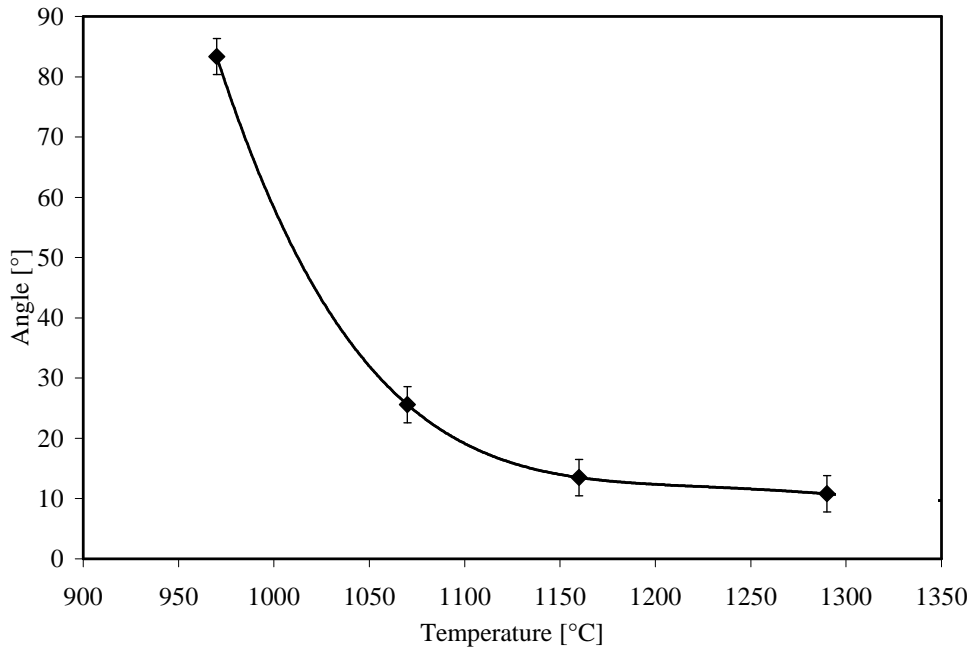


Figure 6.2: Final advancing contact angle of Ag on polycrystalline– Mo, reached at different temperatures.

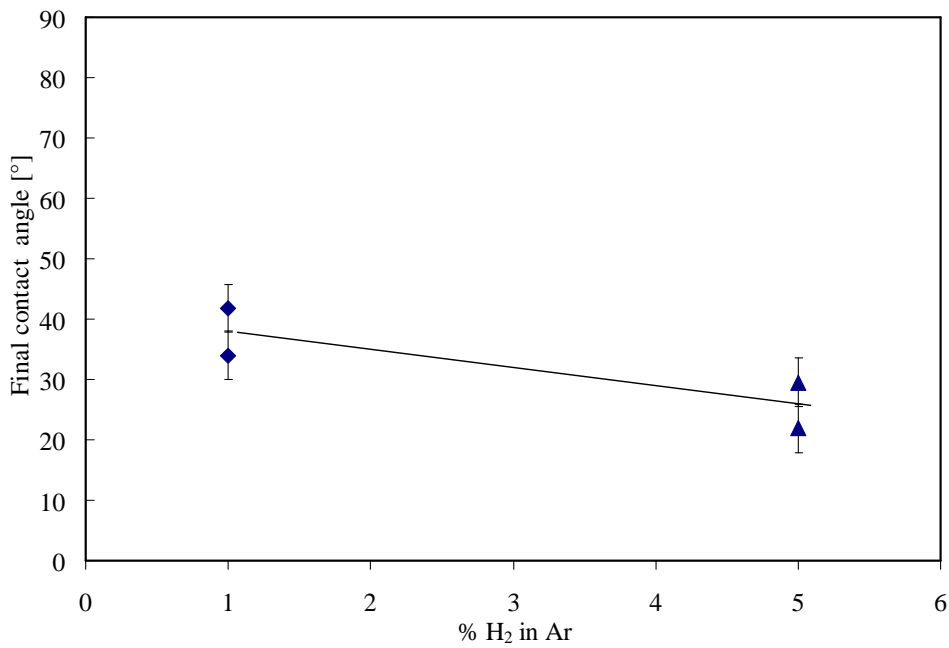


Figure 6.3: The advancing final angle of Ag on polycrystalline– Mo showing influence of H₂ content in the surrounding atmosphere.

6 Experimental results

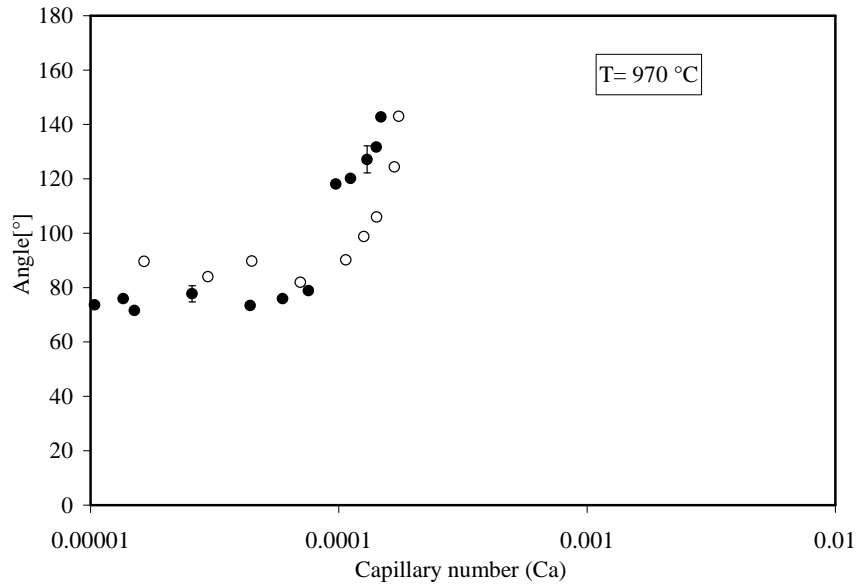


Figure 6.4: Evolution of the contact angle of the Ag drop on polycrystalline – Mo as a function of Capillary number at 970 °C.

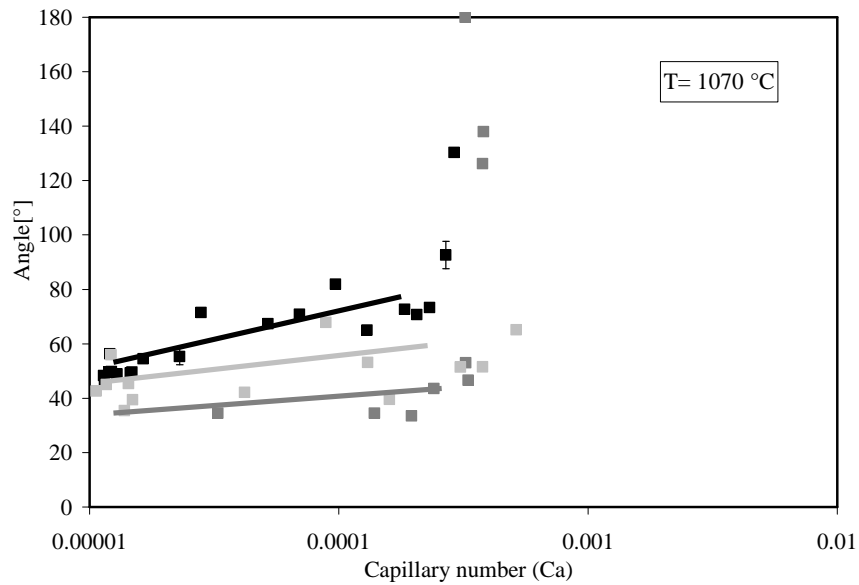


Figure 6.5: The contact angle of the Ag drop on polycrystalline– Mo shown as a function of the Capillary number at 1070 °C. At low velocities an oscillation of the angle is visible. The lines represent a guide to the eye for the general behavior of the data.

6 Experimental results

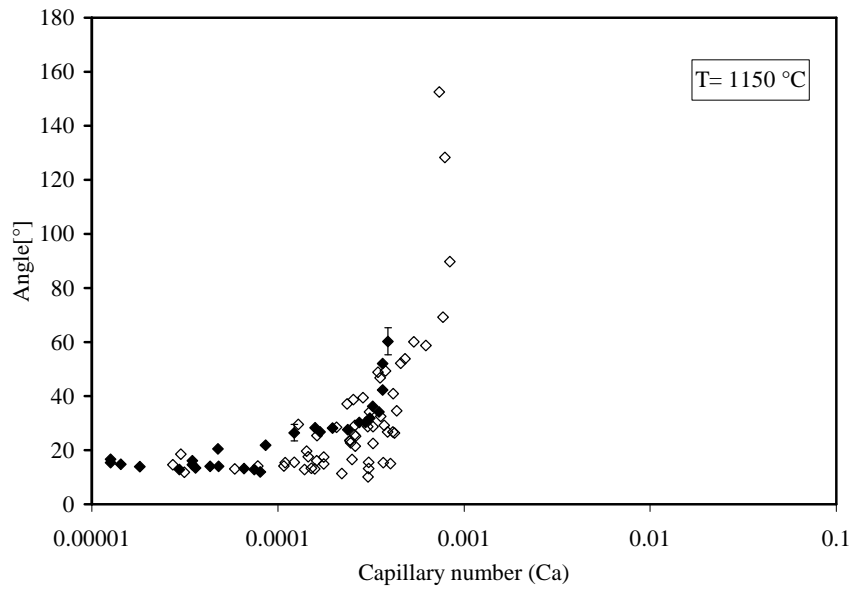


Figure 6.6: Evolution of the contact angle of the Ag drop on polycrystalline– Mo as a function of Capillary number at 1150 °C.

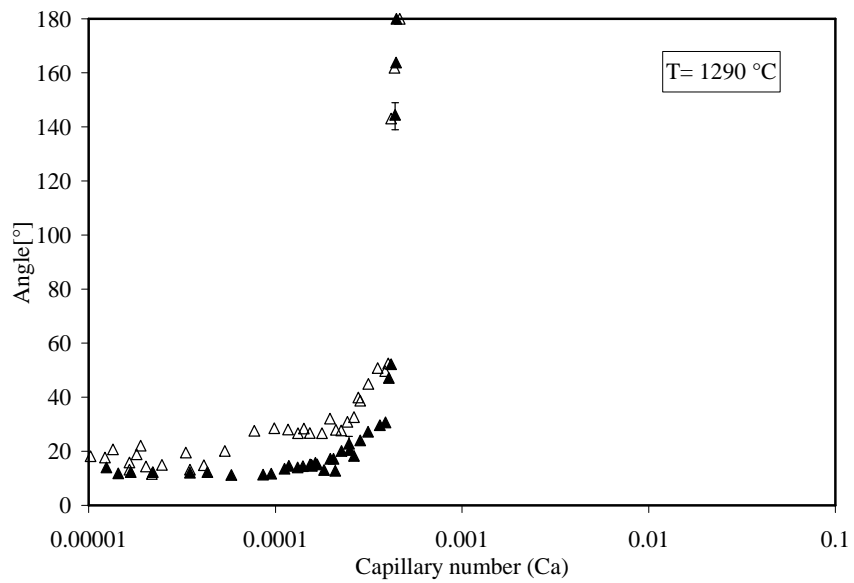


Figure 6.7: The contact angle of the Ag drop on polycrystalline– Mo plotted as a function of the Capillary number at 1290 °C.

6.1.2 Spreading kinetics of liquid Ag on single-crystalline Mo

The time dependence of the wetting angle, as plotted in Figures 6.8A and 6.8B for the cases of single crystalline Mo(110) and Mo(100), shows a sharp decrease in the angle during the initial 0.002 s of the experiment. When the contact angle is very close to its final value, oscillations in the contact angle due to inertia can be seen as was reported for Ag on polycrystalline Mo. Spreading velocities of about 0.3 m/s can be observed. Accordingly, the spreading kinetics and velocities are similar to those seen with Ag on polycrystalline– Mo. The advancing final angle decreases with increasing temperature for Mo(110) and Mo(100) as shown in Figure 6.9. However, this decrease is not as pronounced as in the system Ag on polycrystalline– Mo. The final contact angle in the spreading experiments on single-crystalline Mo(110) is lower than in the case of polycrystalline– Mo for temperatures up to 1150 °C. For higher temperatures the final angle is similar within the error bars. For temperatures lower than 1050 °C the final angle of Ag on Mo(100) is in between the values for Ag on Mo(110) and polycrystalline– Mo. As shown in Figure 6.9 and 6.10A-B the final angle depends on the temperature while the spreading kinetics (related to the capillary number) is temperature-independent.

6 Experimental results

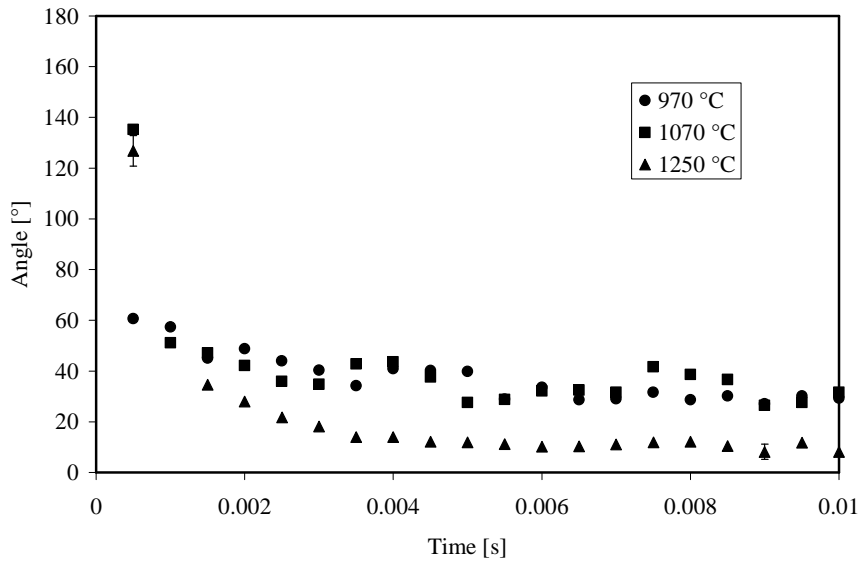


Figure 6.8 A: The contact angle is plotted as a function of time for the spreading of Ag drops on single crystalline Mo(110) substrates at different temperatures. A strong decrease of the angle up to 0.002 s is observed. When the contact angle is very close to its final value, oscillations in the contact angle due to inertia can be seen.

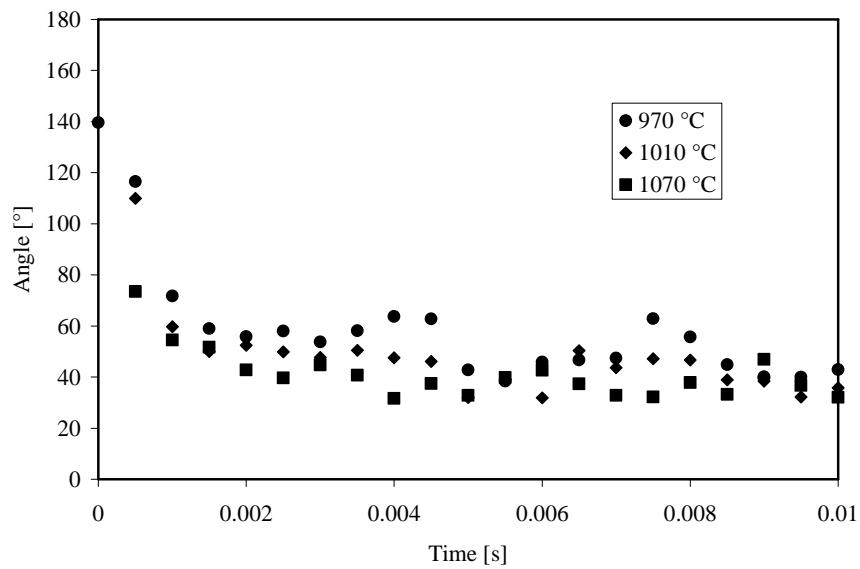


Figure 6.8B: Illustration of the contact angle of liquid Ag on single crystalline Mo(100) substrates as a function of the time.

6 Experimental results

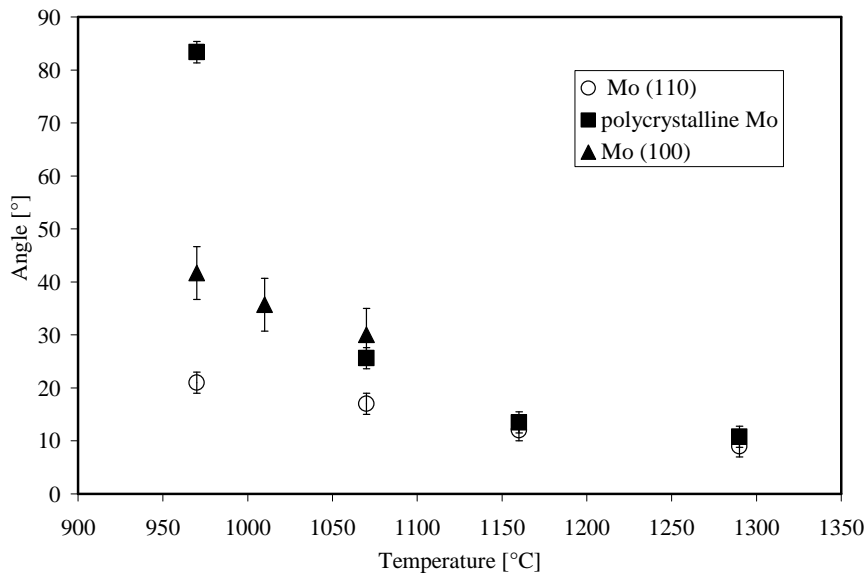


Figure 6.9: Comparison of the advancing final contact angle of Ag on polycrystalline–Mo and on single crystalline Mo(110) and (100), reached at different temperatures. The final angle in case of polycrystalline–Mo and Mo(110) was measured after 0.5 h, the final angle of Mo(100) was measured after 2 s.

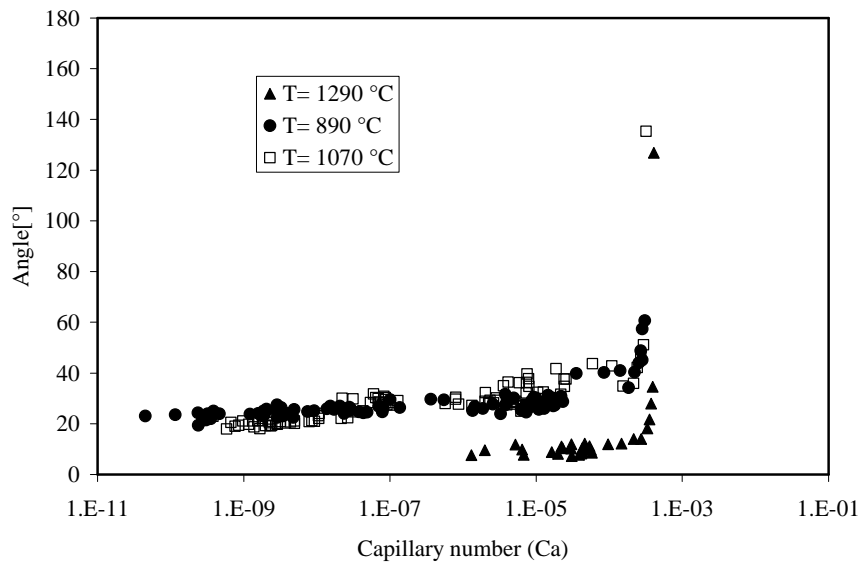


Figure 6.10 A: The contact angle of the Ag drop on single crystalline Mo(110) is shown as a function of the Capillary number for different temperatures.

6 Experimental results

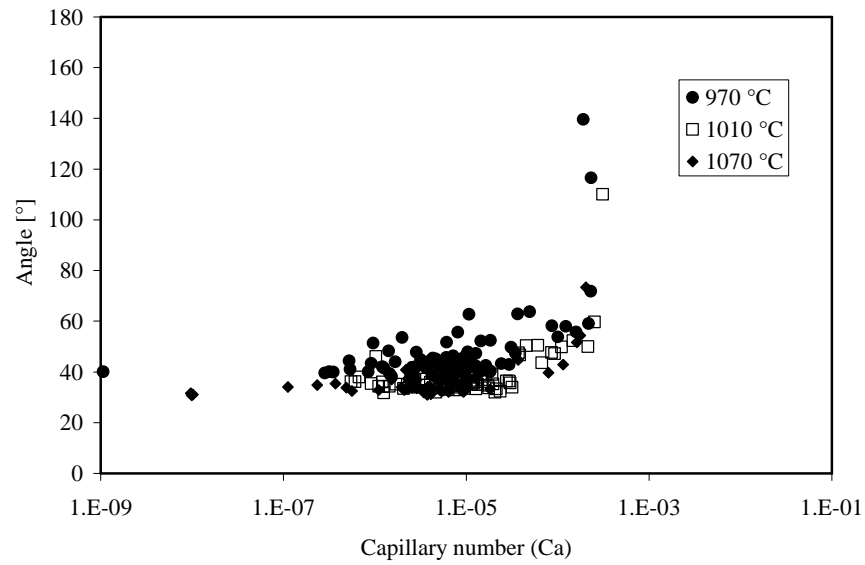


Figure 6.10B: The contact angle of the Ag drop on single crystalline Mo(100) is plotted versus the Capillary number for different temperatures

6.2 Determination of advancing and receding angles

The influence of the surface roughness of the Mo substrates on the spreading was investigated by measuring advancing and receding angles. The roughness was determined by AFM. The receding angle was measured when Ag melted. Figure 6.11 shows that Ag receded at its melting point to a drop with a larger contact angle than at the temperature used for the experiment described in chapter 6.1. When the temperature was raised to the temperature used for the wetting experiment, the Ag drop advanced again.

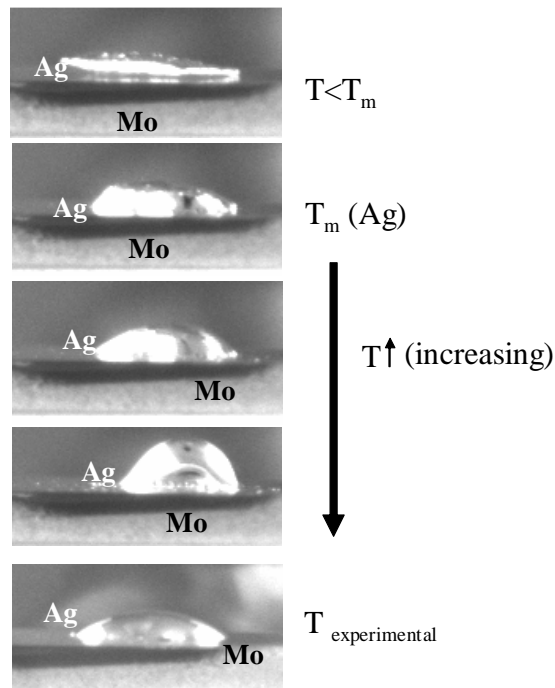


Figure 6.11: Images of the receding Ag drop on a polycrystalline– Mo substrate when the temperature was raised to the desired temperature used for the experiments described in chapter 6.1.

6 Experimental results

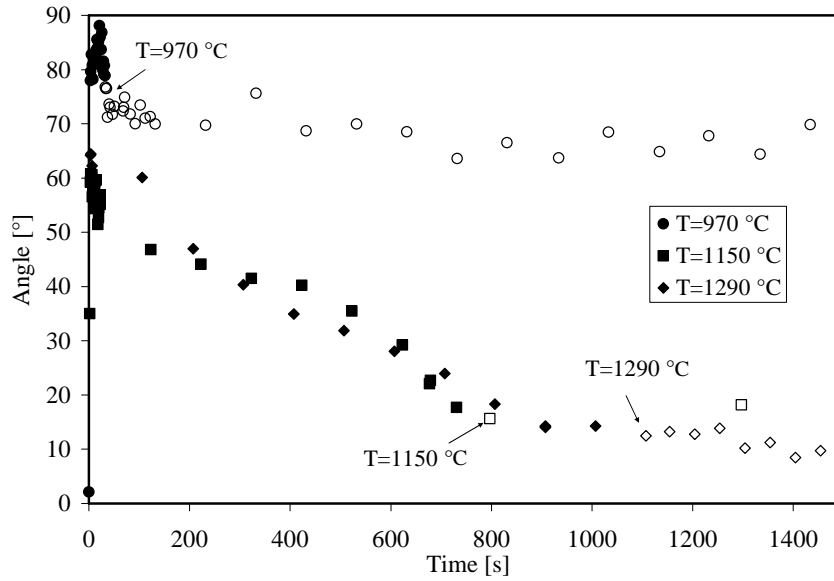


Figure 6.12: Evolution of the receding contact angle while heating to the temperature used for the wetting experiments. The open symbols represent the angles reached at the temperatures used for the wetting experiments (970 °C, 1150 °C, and 1290 °C)

The contact angle increases while the temperature is increased, reaches a maximum value and then decreases with increasing temperature as shown in (Figure 6.12). The final angle is measured after holding the wetting temperature constant for 0.5 h. Since the Ag drop recedes and then advances, the final angle measured here is the same as an advancing angle obtained with the sessile drop method. The final angles obtained with the different methods are shown in Table 6.1A.

Table 6.1 A: Comparison of advancing angles measured by drop-transfer and sessile drop method.

Temperature [°C]	Final advancing angle (drop transfer) [°]	Final advancing angle (sessile drop) [°]
970	83.5	63.6
1150	13.5	15.6
1290	10.8	14.2

No hysteresis between advancing and receding angles in the system Ag-Mo has been observed. Additionally advancing experiments were performed on a variety of polished substrates in order to investigate the effect of roughness on the final angle. The results which are presented in Table 6.1.B reveal that the different surface roughness resulted in similar final angles.

Table 6.1.B The final advancing angles of differently treated Mo substrates are compared

Treatment of the Mo substrate	Temperature [°C]	Roughness [nm]	Final advancing angle [°]
mechanically polished	1070	≈100	29
electrolytically polished	1070	≈300	26

6.3 Effect of equilibration on the final contact angle

In the *equilibrated* experiments the Mo substrate is placed 1-2 mm above the silver drop and kept there at the test temperature for 1 hour before the spreading experiment is performed. In the *non-equilibrated* case the furnace is heated up to the wetting temperature and the wetting experiment is performed as soon as the furnace reaches the wetting temperature. It could be observed that the final angle in the equilibrium case was lower than the final angle in the non-equilibrated case (Figure 6.13). However, the equilibration did not affect the spreading kinetics. This is illustrated in Figures 6.14 to 6.17, which indicate that the angle-capillary number dependency is similar for all wetting temperatures used in this work.

In order to investigate whether Ag is adsorbed on the Mo surface during the heating process prior to the wetting experiment, experiments (equilibrated and non-equilibrated) were performed which were stopped just before the actual wetting had been initiated. In this way one could investigate the Mo surfaces as they were at the actual wetting. Figure 6.18 shows SEM micrographs of the Mo substrate. To remind the reader the Mo was annealed under Ar/5 %H₂ gas flow with Ag vapor in the atmosphere.

6 Experimental results

In the equilibrium case (Figure 6.18 A, C) the Mo substrate was in close proximity to the Ag droplet (1-2 mm) and annealed at the test temperature for 1 hour. In the non-equilibrium case (Figure 6.18 B, D) the Mo was heated with Ag vapor in the atmosphere to the test temperature and quenched as soon as the test temperature was reached. The Mo substrate was not kept in close proximity to the Ag droplet. The distance between the liquid Ag drop and the Mo substrate was about 1-2 cm. As one can see in the scanning electron microscope images, Ag drops cover the Mo substrate prior to the wetting experiment when equilibrated for one hour. There is no preferred nucleation site of the Ag droplets on Mo. It should be noted that the individual Ag drops can not be seen in the low magnification images. No Ag droplets were observed in the non-equilibrated case. The higher the annealing temperature the greater the area covered by Ag droplets and the greater the size of the droplets. The determination of the coverage of Mo with Ag was performed while the e^- beam was scanned over an area of about $100 \times 100 \mu\text{m}$. The results are summarized in Table 6.2.

Table 6.2: Comparison of the coverage of Ag droplets on the Mo substrate as a function the temperature, for the equilibrated case.

Coverage of Ag [area %] (Mo equilibrated at 1070 °C)	Coverage of Ag [area %] (Mo equilibrated at 1290 °C)
0.94	23.14

6 Experimental results

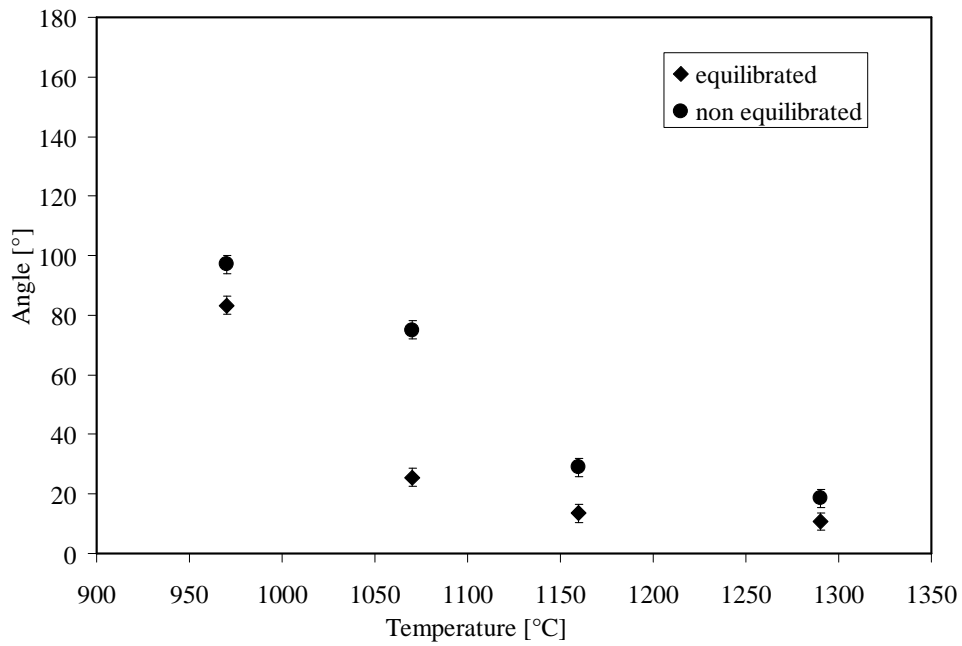


Figure 6.13: Comparison of the final contact angle of Ag on polycrystalline– Mo in case of equilibration and non-equilibration.

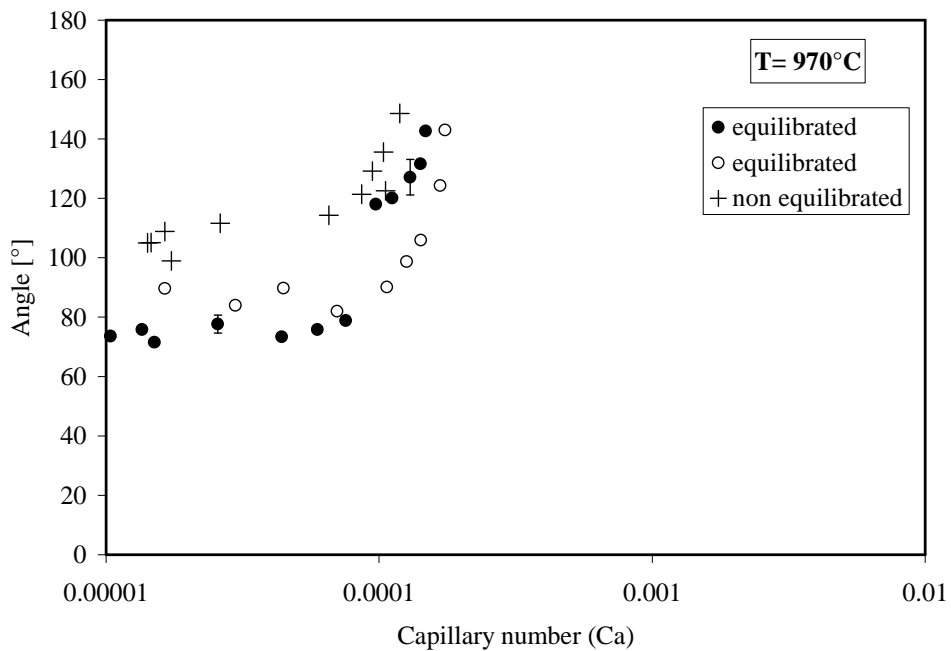


Figure 6.14: Evolution of the contact angle of the Ag drop on polycrystalline– Mo in an equilibrated system and non-equilibrated system at 970 °C.

6 Experimental results

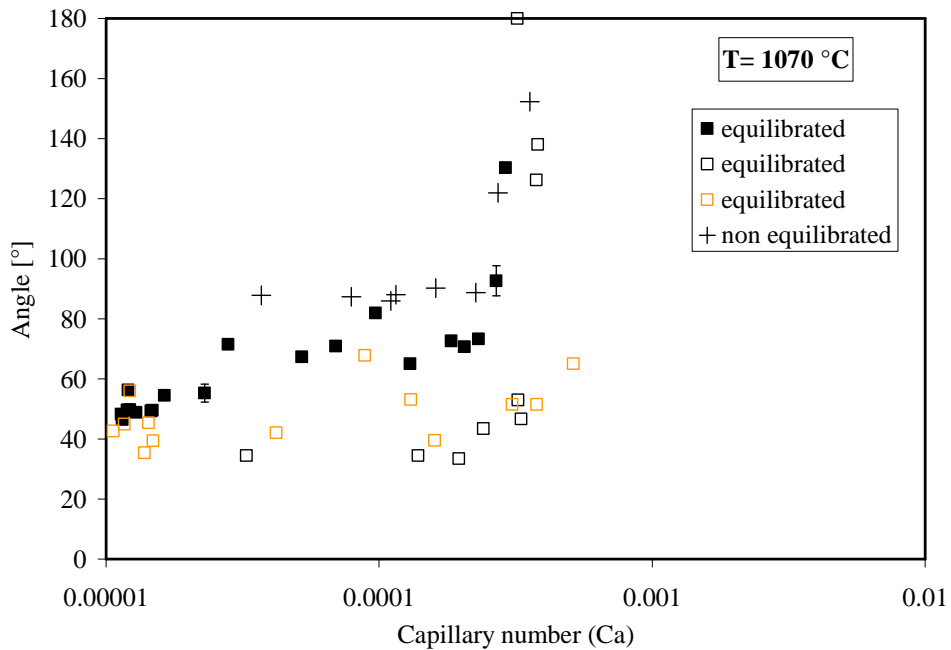


Figure 6.15: Contact angle – Capillary number dependence of the Ag drop on a polycrystalline–Mo substrate for the equilibrated system and non-equilibrated case at 1070 °C. Oscillations in the contact angle at low velocities are visible.

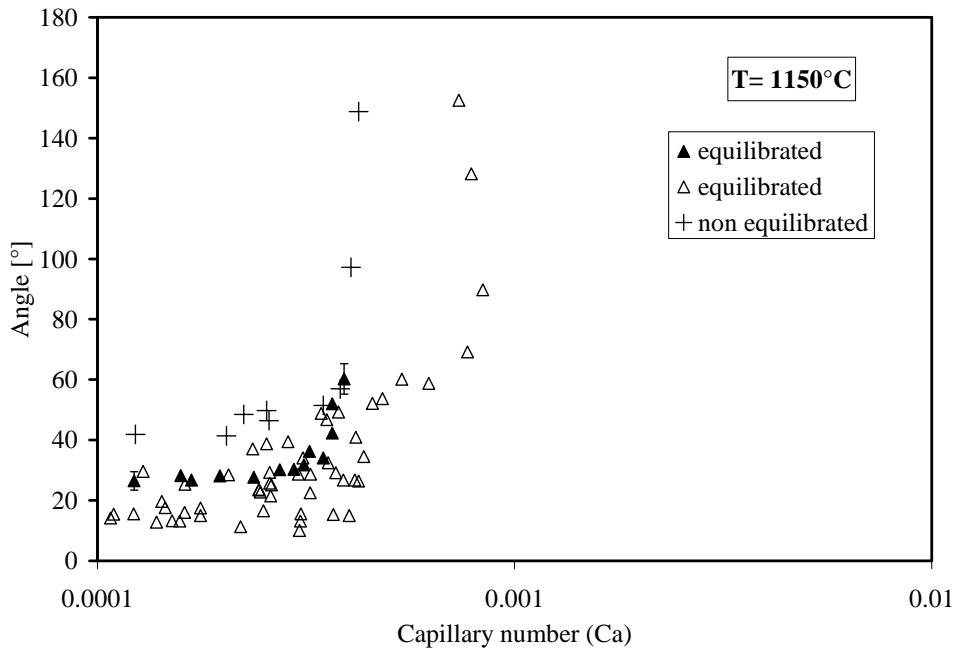


Figure 6.16: The contact angle of the Ag drop on polycrystalline– Mo in an equilibrated system and non-equilibrated system is plotted versus the Capillary number at 1150 °C.

6 Experimental results

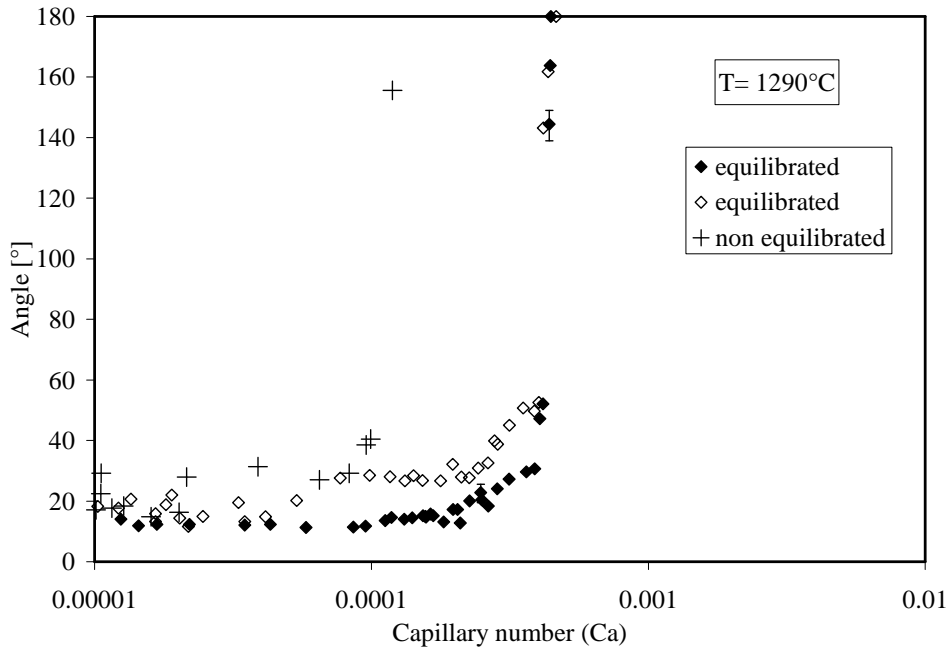


Figure 6.17: Contact angle-Capillary number dependence of the Ag drop on polycrystalline– Mo in an equilibrated and a non-equilibrated system at 1290 °C

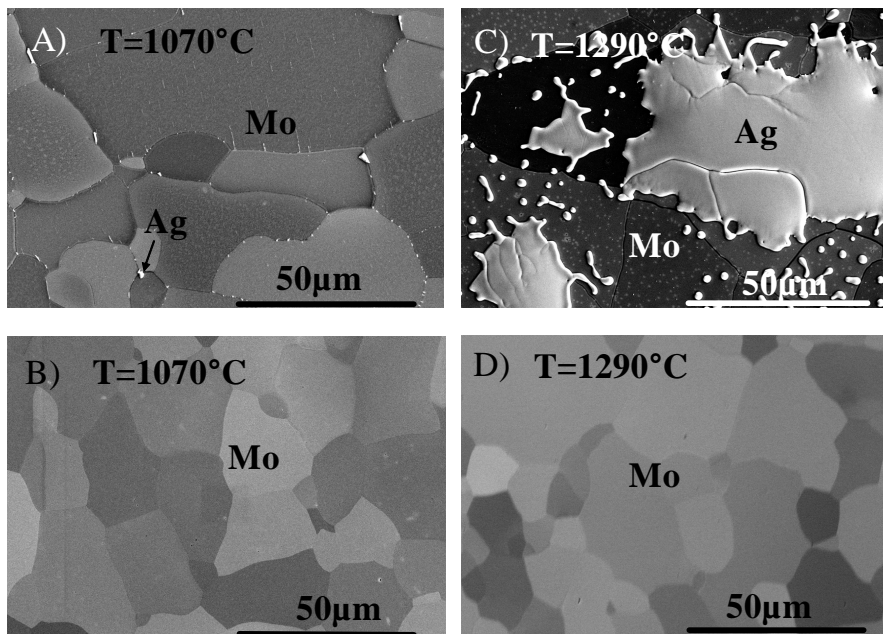


Figure 6.18 (A) and (C) show the SEM images of the Mo substrate annealed in Ar/5% H_2 gas flow and Ag vapor in the atmosphere at 1070 °C and 1290 °C under equilibrated conditions, (B) and (D) show the Mo substrate annealed with Ag vapor in the atmosphere at 1070 °C and 1290 °C under non–equilibrated conditions.

Auger analyses were performed of the Mo substrates annealed under Ag vapor at equilibrated and non equilibrated conditions as are shown in Figure 6.18 C and D.

In summary, the final equilibrium angle of liquid Ag on Mo depends on temperature, equilibration state and Mo orientation (polycrystalline–Mo, Mo(110) and Mo(100)). The final contact angle decreases with increasing temperature. The contact angle is always higher for the non-equilibrated case compared to the equilibrated case. However, the spreading kinetics are the same for all temperatures, equilibration states and orientations of the Mo substrate.

6.4 Grooving experiments of Mo

Grooving experiments were performed in order to calculate the surface diffusivities that control ridge evolution. The diffusion constant was determined on electrolytically polished samples which were annealed for 0.5 h, 1 h, and 1.5 h at 1070 °C, 1150 °C, and 1290 °C in flowing Ar/5 %H₂ and Ag vapor present in the furnace atmosphere. The Mo substrate was kept in close proximity (1-2mm) to the liquid Ag drop during the annealing process. The groove width for the different samples was investigated by AFM. The Mullins constant as well as the diffusion coefficient were determined and compared with values from the literature, as described later in chapter 7. Figure 6.19 shows the Mo surface after different annealing temperatures and times. The higher the temperature the greater is the size of the Ag droplets on the Mo substrate. Figure 6.20 displays the dependence of the groove width on temperature and time. Diffusion coefficients are obtained by fitting Mullins equation to the measured data. The lines in Figure 6.20 represent these fittings and the symbols represent the data points. In Figure 6.21 the dependence of the groove height on temperature and time is shown. The groove height increases with increasing temperature. The error in measuring the groove height is greater than in measuring the groove width due to the diameter of the AFM tip. Therefore the time dependence of the groove width was used to determine the Mullins constant and the diffusion coefficient. Figure 6.22 represents the ratio of the groove height to the groove width for the different annealing times. The ratio is constant within

6 Experimental results

the error bars. This is in accordance with Mullins grooving theory. From the Arrhenius plot in Figure 6.23 one can determine the diffusion enthalpy ΔG for Mo under the experimental conditions used in this work. Using Equation 6.1, the calculated diffusion enthalpy is 1.8 ± 0.9 eV.

$$D = D_0 e^{\frac{\Delta G}{kT}} \quad (6.1)$$

6 Experimental results

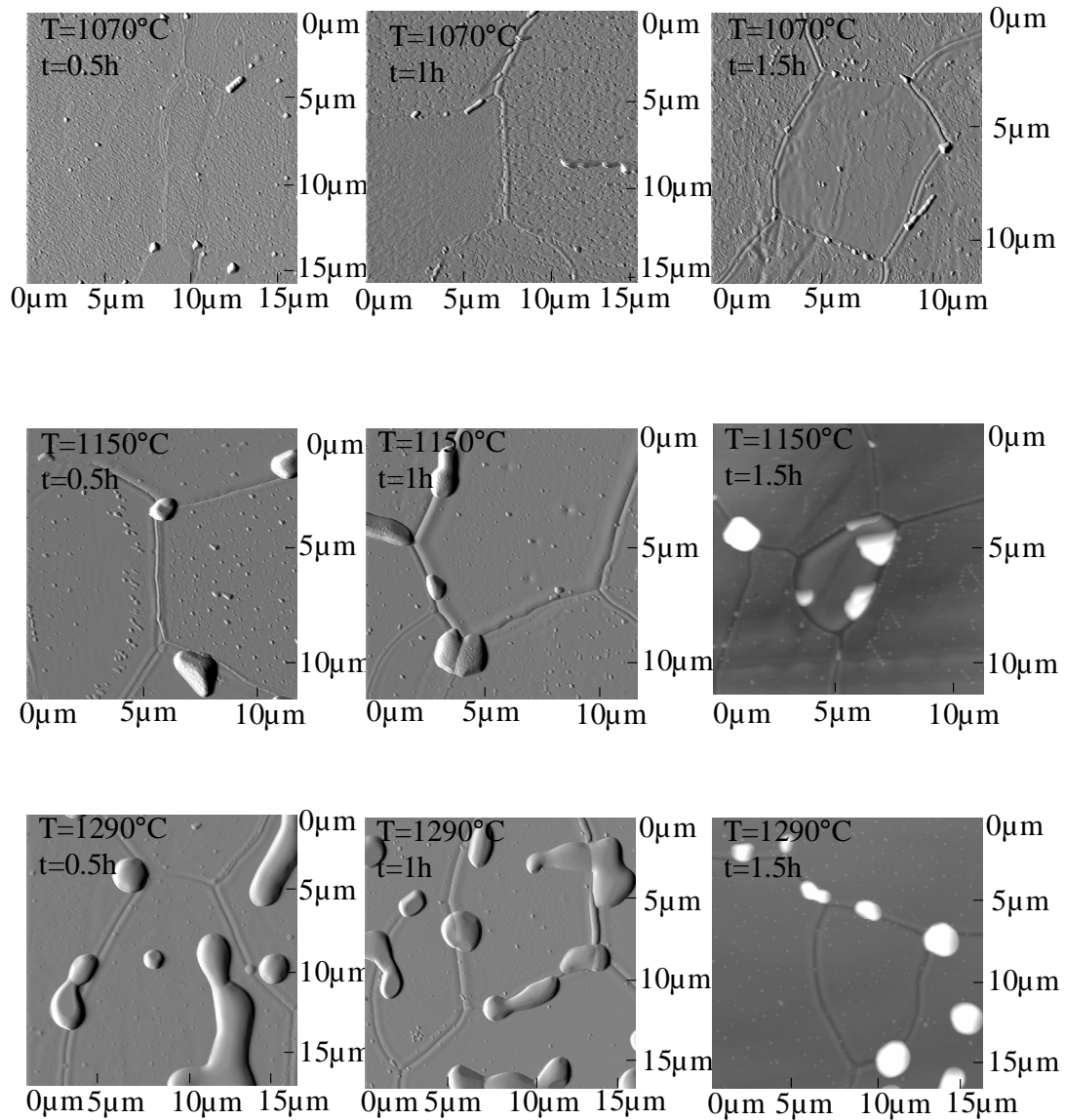


Figure 6.19: AFM images of Mo substrates annealed under Ar/5% H_2 gas flow and Ag vapor in the atmosphere at different temperatures and times. It can be seen that the amount and size of the Ag droplets increase with increasing temperature. Note that the AFM images taken for the samples at 1150°C (at all annealing times) and the AFM image at 1070°C annealed for 1.5h are taken at different magnifications than the other images.

6 Experimental results

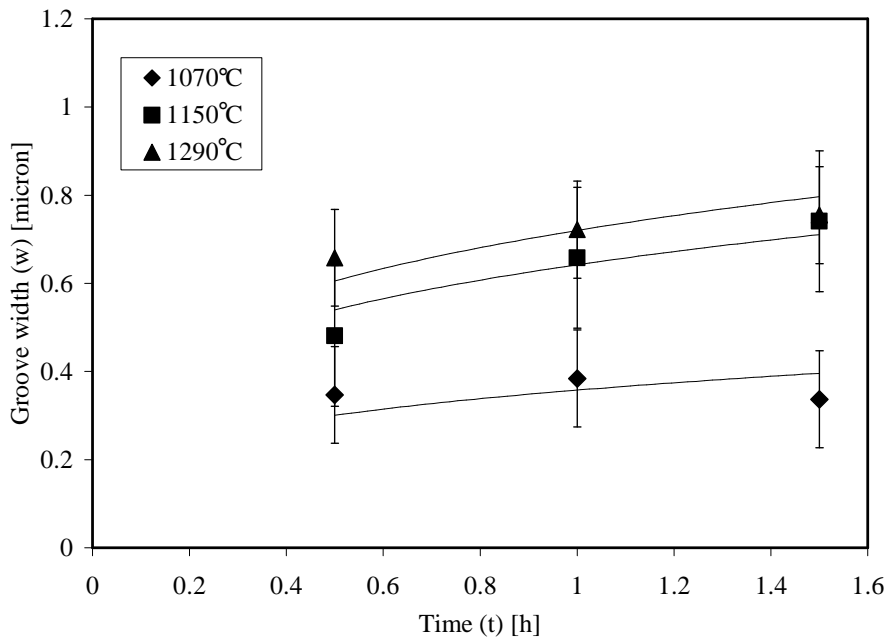


Figure 6.20: Time and temperature dependence of the groove width.

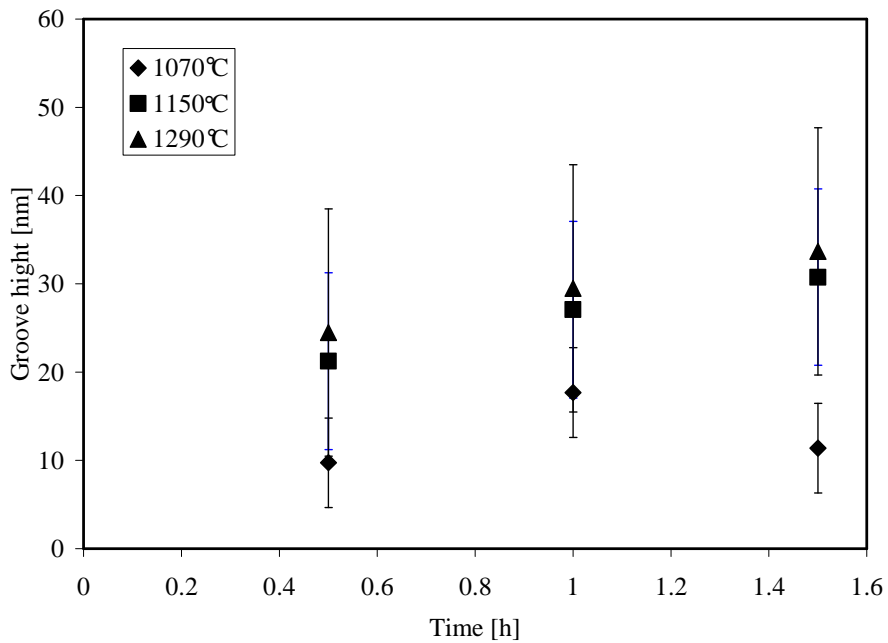


Figure 6.21: The dependence of groove height on time and temperature (1070 °C, 1150 °C and 1290 °C) are shown.

6 Experimental results

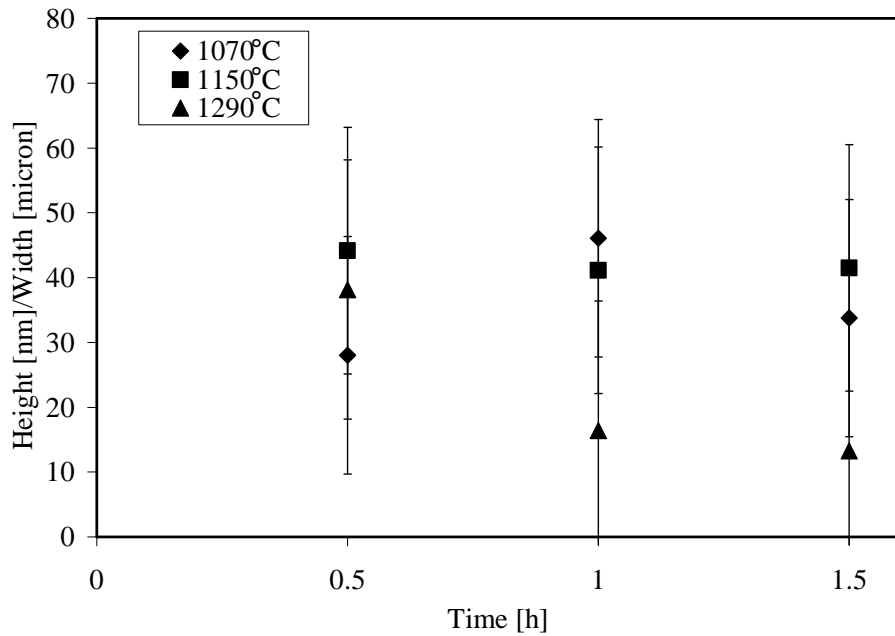


Figure 6.22 Dependence of the ratio of groove height/groove width on time and temperature. The ratio of groove height/width stays constant within the error bars for each temperature.

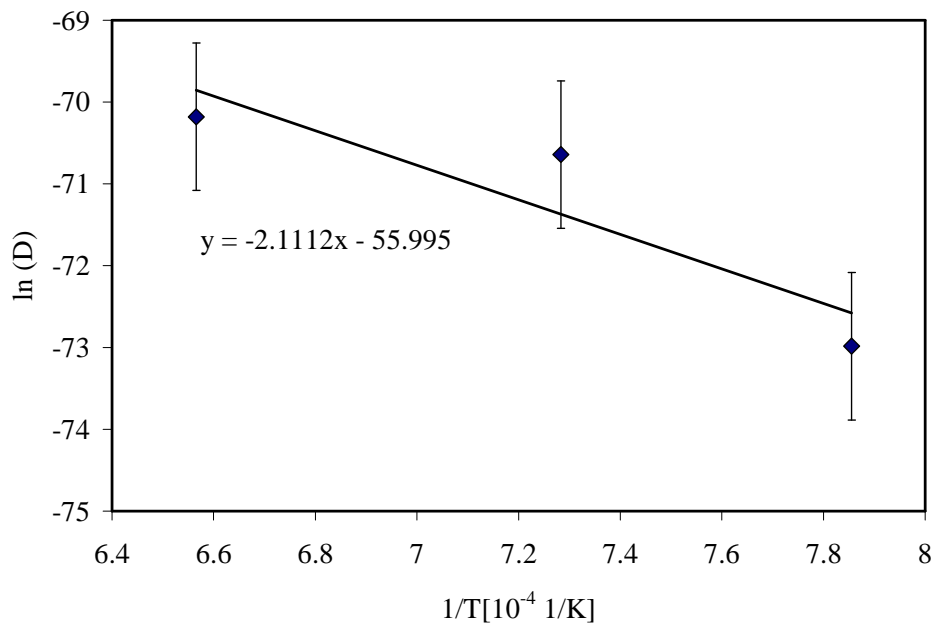


Figure 6.23: The dependence of the logarithm of the diffusion constant (D) versus $1/T$. is plotted. The symbols are the data points; the line represents the Arrhenius plot.

6.5 Investigations of the microstructure

In order to investigate whether effects like ridging, diffusion, adsorption and grain orientation of the polycrystalline– Mo influence the spreading kinetics of liquid Ag on Mo, microstructure investigations were performed. The objective of these studies was to determine the structure of the Mo surface, the Ag-Mo interface, and the triple line of the samples after cooling.

6.5.1 Scanning electron microscopy

The microstructure of the Mo and Ag surfaces and of polished cross sections after the spreading experiment was analyzed by SEM using a field emission microscope (JEOL 6300F).

Figures 6.24A-C show high-resolution SEM micrographs of the Ag drop on the polycrystalline– Mo substrate after the wetting experiment at 1070 °C. Grain boundaries are clearly visible on the Mo substrate. The visibility of the Mo grains on the surface indicates that thermal etching took place during the experiment. The grain size and texture were further investigated by OIM experiments.

Small droplets are visible approximately 2-6 μm ahead of the silver drop (Figure 6.24 C), (Figure 6.29). These droplets surround the Ag droplet and have a height of about 100 nm. The droplets contain Si and Ca as detected by EDS analyses in the SEM. Additional element identifications were done by Auger measurements (see chapter: 6.5.5) The area on the Mo substrate between the row of droplets and the silver drop is clean, the rest of the Mo surface is covered by the tiny droplets (nano-droplets). It is suggested that due to a thermal shrinkage of the Ag drop that a ridge could be present in the between the Ag drop and the row of small droplets after cooling (chapter 7.8). This possibility was studied by AFM measurements and is summarized in chapter 6.5.2.

A higher magnification image of the triple line in Figure 6.24 B indicates that the Mo grains do not influence the movement of the Ag from a microscopic point of view.

High-resolution SEM micrographs of the Ag drop on the single crystalline Mo substrate after the wetting experiments at 970 °C, 1070 °C, 1150 °C and, 1290 °C are displayed in Figure 6.25. No facets on the Ag drop surface were observed.

The results of the spreading kinetics and grooving experiments indicate that the probability of ridge formation would be the highest for longer experiments where samples were annealed for one hour at the maximum temperature after spreading. For this reason this system was chosen for more detailed investigations. In order to protect the sample against mechanical abrasion and also to protect the triple line, the Ag-Mo sample was coated with Cr, as described in chapter 5. Within the detection limit of the SEM, which is 5-10 nm, no ridge was detected. EDS analyses in the SEM showed that after spreading no appreciable diffusion of Mo into the liquid Ag occurred at 1000 °C within the resolution limit of the EDS investigations, Figure 6.27. For further TEM investigations (chapter 6.5.3) the sample, shown in Figure 6.26 was ion-milled and the interface as well as the surface around the triple line were investigated in order to determine whether a ridge had formed.

6 Experimental results

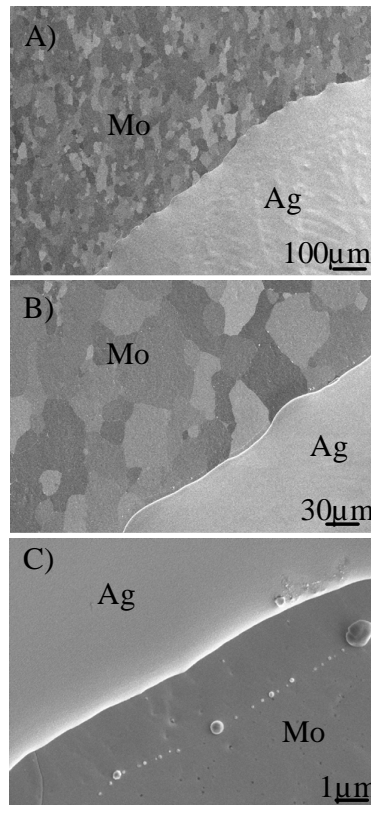


Figure 6.24: SEM micrographs of the Ag droplet on polycrystalline– Mo substrate after quenching from 1070 °C taken with different magnifications.

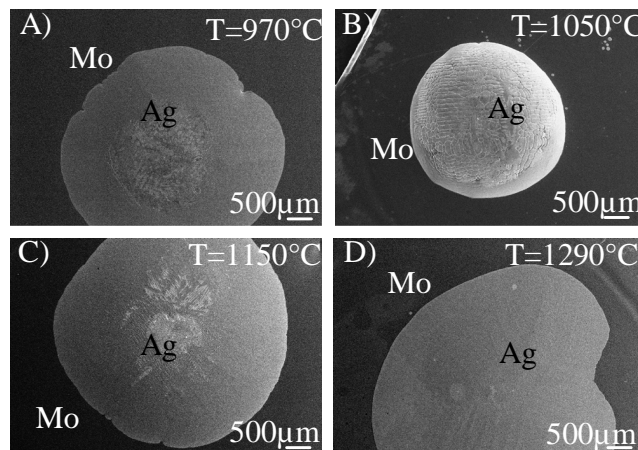


Figure 6.25 A-D: Top view image of Ag on single crystalline Mo. The wetting experiments were performed at A) 970 °C, B) 1070, C) 1150 °C and D) 1290 °C and the samples quenched afterwards to room temperature.

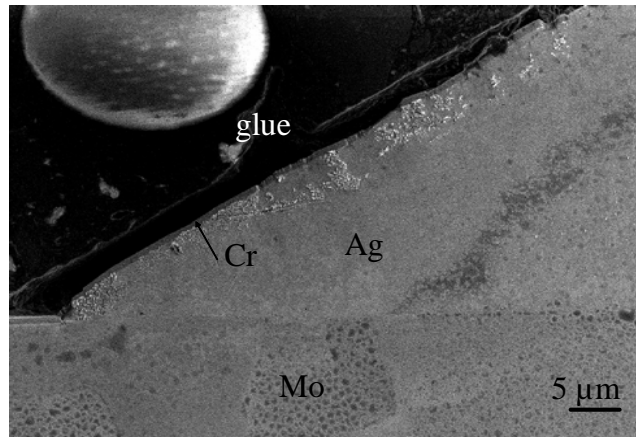


Figure 6.26: Cross-section of an Ag drop on a polycrystalline– Mo substrate. The experiment was performed at 1070 °C, kept at this temperature for one hour and the specimen quenched afterwards. The cross-section shows some inhomogeneties which is due to the sample preparation.

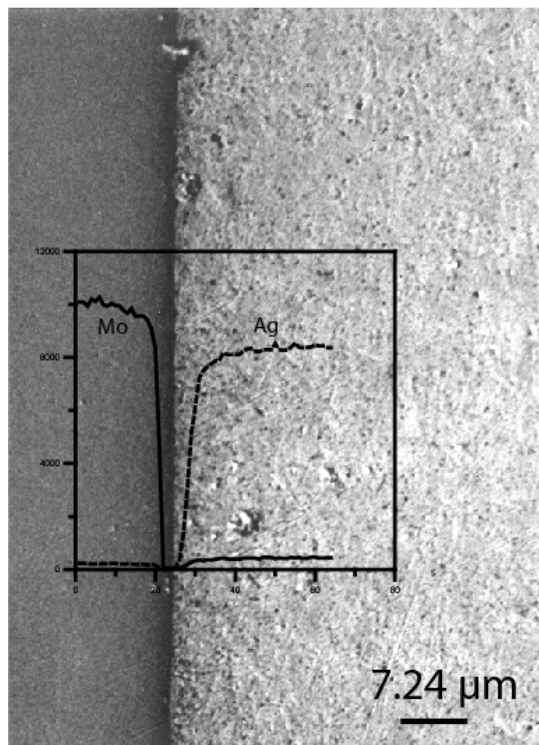


Figure 6.27: EDS line analyses in the SEM of the cross-section of the Ag droplet on polycrystalline– Mo. The temperature of the wetting experiment was 1070 °C. After the wetting experiment was performed this temperature was held constant for one hour. Afterwards the sample was quenched.

6.5.2 Atomic Force Microscopy

AFM measurements of the Ag-Mo samples produced under a gas flow of Ar/5 %H₂ at 1070 °C annealed for one hour and quenched afterwards, did not show any ridges in the smooth area between the silver droplet and the droplets which surround the silver drop (Figure 6.28). In Figure 6.29 an SEM micrograph of the quenched wetting sample is shown. The Ag drop is surrounded by smaller droplets, further away from these droplets nano-droplets are visible. The heights of the nano-droplets were measured with the AFM and ranged between 15 and 30 nm (Figure 6.30). These nano-droplets can not be analyzed by EDS in the SEM. AFM-measurements show that the heights of the droplets which surround the Ag drop are about 100 nm. Auger measurements were performed in order to identify these particles (chapter 6.5.5).

For the experiments where a Mo single crystal was used as a substrate, a similar microstructure was found (Figure 6.31) as for the polycrystalline substrate. Nano-droplets and droplets surrounding the Ag drop were observed.

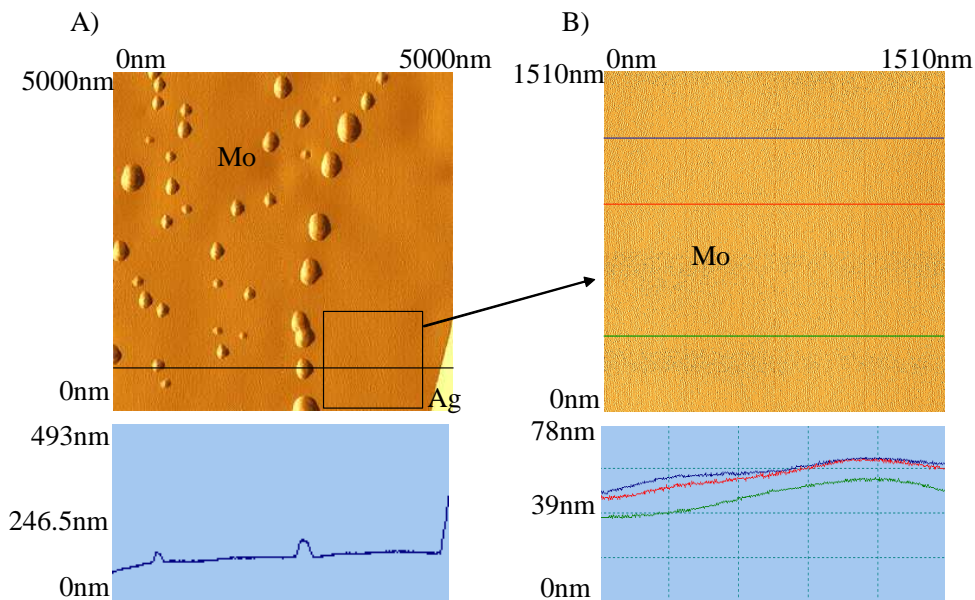


Figure 6.28 A and B: AFM images of a Ag drop on polycrystalline– Mo substrate. The wetting experiment had been performed at 1070 °C. After maintaining this temperature for 1h, the sample was quenched to room temperature. (A) Shows an area where small Ag droplets occur. (B) is an enlarged image of the area indicated in A. No ridge was detected within the resolution limits of the AFM.

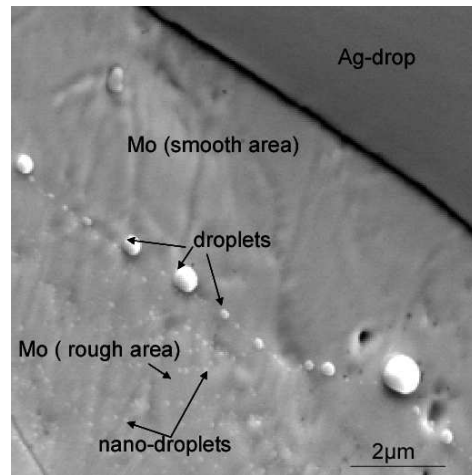


Figure 6.29: SEM micrograph of the surface structure of the Mo ahead of the Ag drop. Small droplets which surround the Ag drop and nano-droplets further away from those droplets are visible.

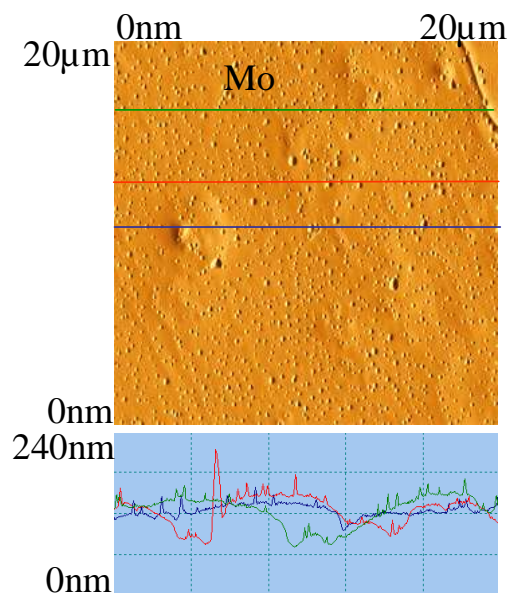


Figure 6.30: AFM image showing nano-droplets on the Mo surface at a distance of 7 μm ahead of the Ag drop.

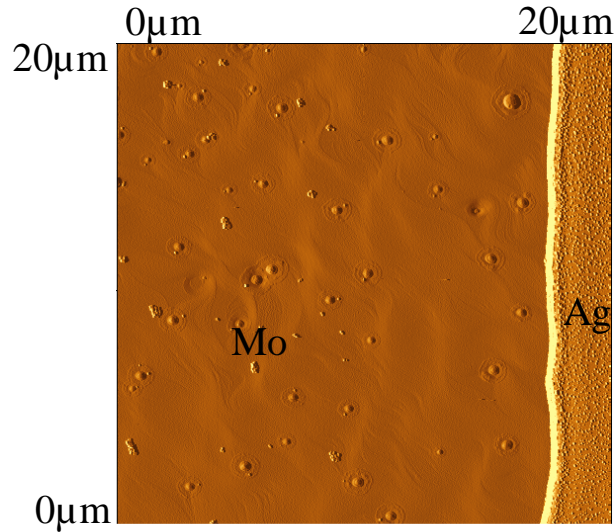


Figure 6.31: AFM images of the surface structure of Ag on single-crystalline Mo. The wetting temperature was 1070 °C. Droplets surrounding the Ag drop are visible on the surface.

6.5.3 Transmission Electron Microscopy

In order to investigate the interface between Ag and Mo, TEM samples were prepared from the Ag-Mo (polycrystalline) wetting samples produced at 1070 °C. According to the studies of the spreading kinetics, which will be explained in more detail in chapter 7.7 and 7.8, ridge formation could take place in the long term Ag-Mo studies. Therefore, the investigation of ridge formation on those Ag-Mo samples was performed. A JEOL 2000 FX was used to investigate the specimen. High-resolution TEM images at the Ag-Mo interface were acquired with a JEOL 4000EX. TEM samples were prepared using a FIB (see chapter 5.3.2).

Conventional TEM was done with the JEOL 4000 EX and the Zeiss 912 Omega. The aim was to (i) determine whether ridges had formed at the triple line and (ii) to determine the orientation relationship between the Ag and the Mo at the triple line. In Figure 6.32 a bright field TEM image of the Mo surface which is covered by a Cr protection layer ahead of the Ag drop is shown. The Mo surface looks wavy as it was

observed by AFM measurements. Figure 6.33 shows a bright field image of the Ag-Mo interface. No ridge could be detected at the Ag-Mo interface and the Mo surface within the resolution limits of the TEM.

Figure 6.34 shows four diffraction patterns taken at different positions of the sample as are indicated in the bright field TEM micrograph. Position 1 was in the bulk Mo and position 2 was in the bulk Ag region. Closer to the triple line, neither the Ag nor the Mo diffraction patterns changed. Hence the same grain of Ag and Mo exists at the triple line as at positions 1 and 2. The diffraction patterns 3 and 4 were taken at the interface of Ag and Mo. They consist of the diffraction pattern of pure Ag and pure Mo. The tilt angle between the Ag grain and the Mo grain at the interface is 39.88° and the tilt axis is [322].

EDS measurements at the Ag-Mo interface were carried out in a VG HB 501 UX. The goal was to measure a concentration profile across the Ag-Mo interface for the wetting sample prepared at 1070°C in order to investigate possible Mo diffusion into the Ag drop. To perform the EDS measurements, the TEM sample prepared by FIB was used. As mentioned earlier the TEM lamella was put on a copper grid. The line analysis of the EDS measurements in Figure 6.35 showed Mo peaks at each position of the sample, e.g. in the silver drop and the Cr layer. The content of Mo was more than 0.5 at% (which is the solubility limit of Mo in liquid silver at 1070°C).

The reasons for such a large Mo content in the silver drop as well as in the Cr layers are:

- The TEM sample was not well oriented to the detector such that one has a fluorescence effect in the Mo.
- The whole sample was contaminated with Mo due to the TEM preparation with the FIB.

To determine whether fluorescence occurs in the Mo, the TEM sample was turned by 180° . The EDS profiles in Figure 6.36 show that Mo was still detected all over the surface. Hence it can be excluded that fluorescence is responsible. Since the effect is the result of the sample preparation, the TEM preparation has to be further improved. For additional investigations the TEM sample would have to be fixed with tungsten onto the

copper grid and ion milling has to be performed in order to remove the surface layer damaged by the ion beam. The ion milling should be performed from both sides of the sample with a low energy in order to clean the surface. The EDS measurements showed in all spectra C, Si, Cu, Ga, O, and Fe. Fe has its origin from the polepiece in the VG microscope. Si, C, Cu, O have their origin from the copper grid. Ga arises from the cutting process in the FIB. In addition Ga and Cr segregate at the interface as schematically shown in Figure 6.37 A). The concentration of Ga and Cr was determined at the Ag/Mo interface in a thick and a thin area of the sample. Table 6.3 reveals that a higher content of Ga and Cr was detected in the thinner area at the interface than at the thicker area. This and the fact that the interface appeared bright in the Z-contrast image (bright means either higher atomic number or thicker area of the sample) is a hint for segregation of Ga and Cr at the interface as it is indicated in Figure 3.37 A). No diffusion of Ga and Cr into the interface occurs Figure 3.37 B). If diffusion into the interface has occurred, one would not detect less Ga and Cr in the thicker area of the specimen.

Table 6.3: Concentration of Ga and Cr on the surface of an Ag-Mo cross-section

	Ga [at%]	Cr [at%]
Interface in a thin area of the sample	3	10.4
Interface in a thick area of the sample	1.3	4.3

To conclude, TEM preparation has to be further improved in order to perform detailed EDS analyses.

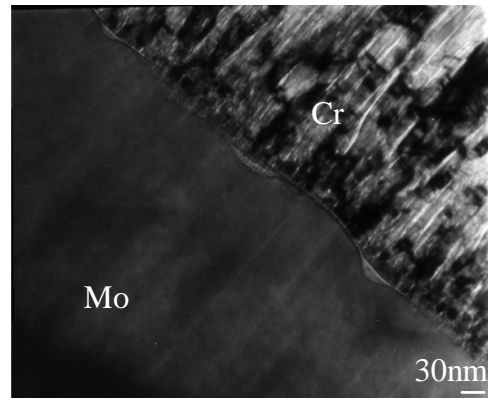


Figure 6.32: Bright field TEM image of the cross-section of the Mo surface protected by a Cr layer. The Mo surface is ahead of the Ag drop. The surface appears rough.

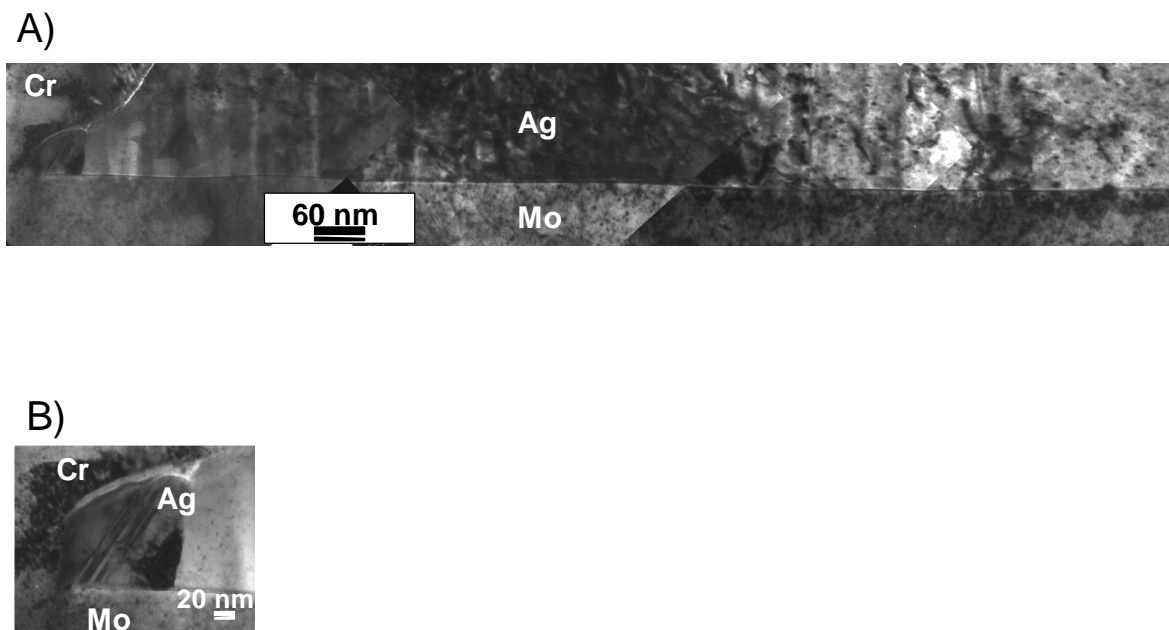


Figure 6.33: TEM bright field image of (A) the Ag-Mo interface and the triple line, B) higher magnification image of the triple line region. No ridges were observable within the detection limits of the TEM

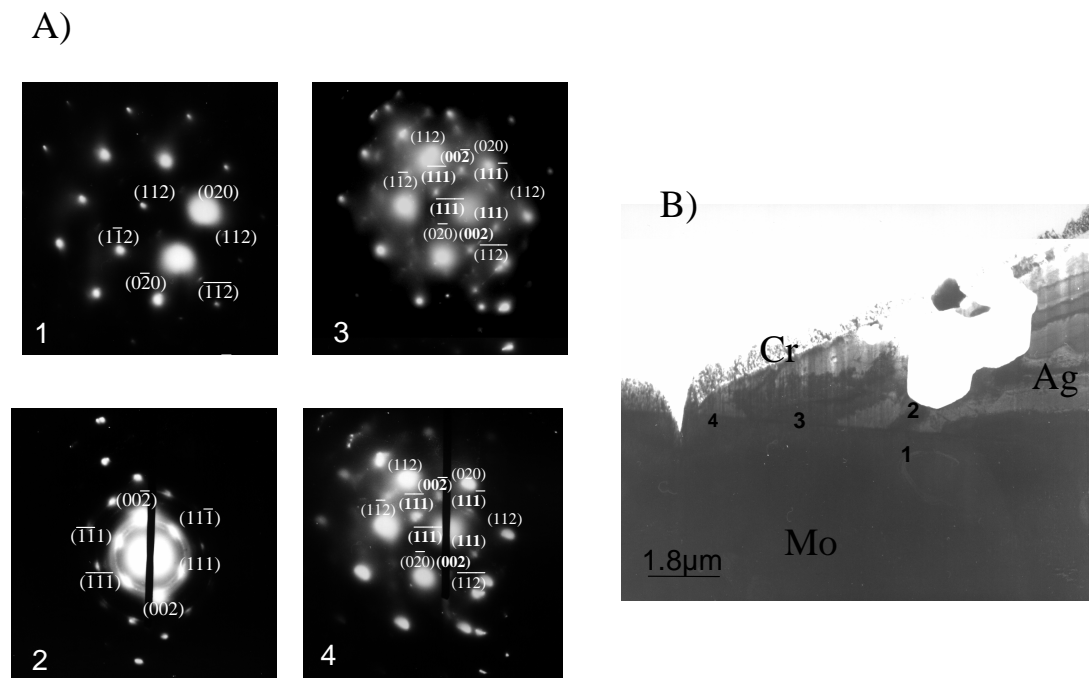


Figure 6.34: (A): SAD pattern 1-4 , which were acquired at the positions marked in the conventional TEM image (B). The SAD pattern 1 was taken in the pure Mo matrix, pattern 2, was acquired in the pure Ag, patterns 3+4 are taken from the interface Ag-Mo. The tilt angle between the Ag grain and the Mo grain at the triple line is 39.88° and the tilt axis is $[322]$.

6 Experimental results

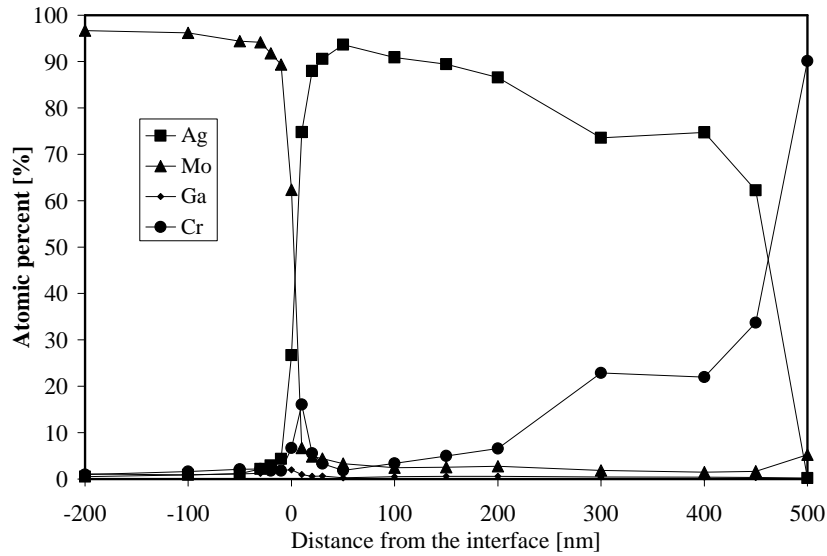


Figure 6.35: EDS measurements along the Ag-Mo interface. On the left side from the interface is the Mo matrix, the right side is the Ag drop.

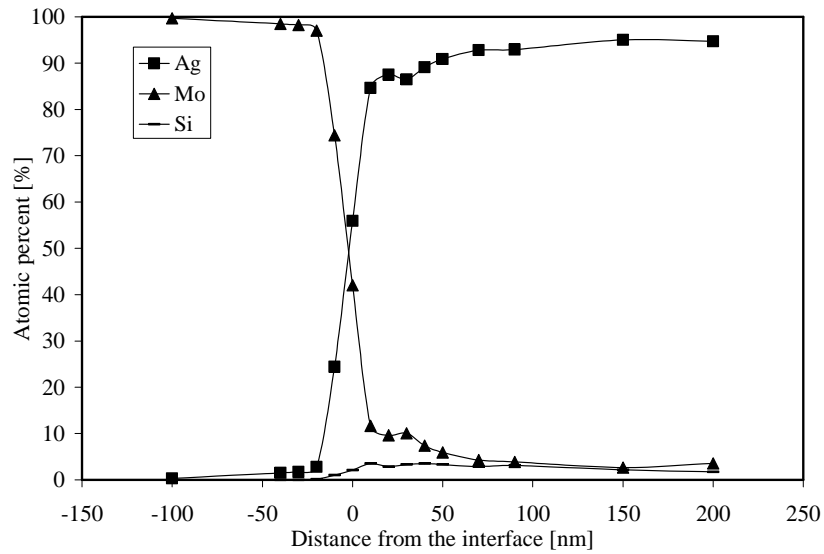


Figure 6.36: EDS measurements along the Ag-Mo interface, the sample was turned by 180° compared to Figure 6.35. The left side of the interface represents the Mo matrix, the right side the Ag drop.

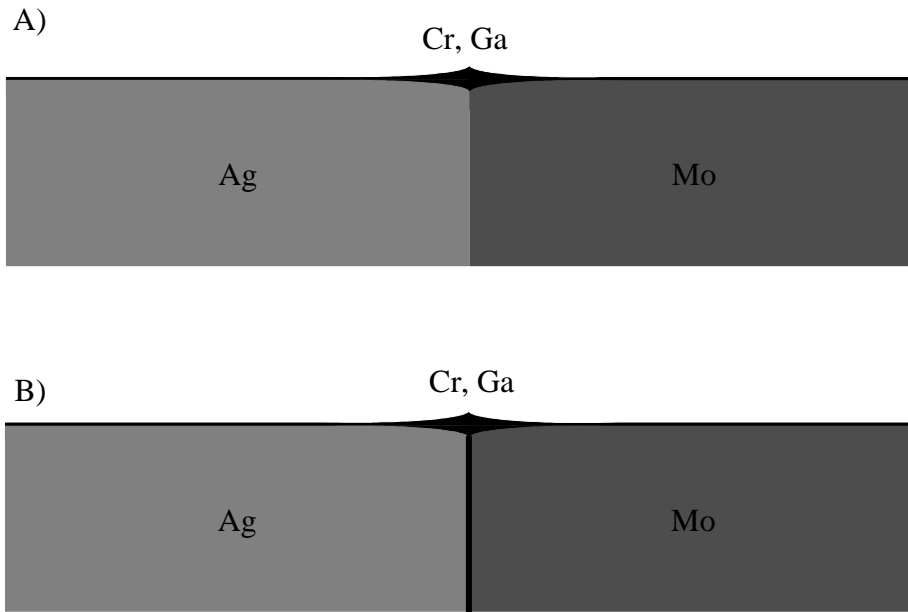


Figure 6.37: Schematic Illustration of a segregation of Ga and Cr on the surface of the Ag-Mo cross-section (A), Segregation and diffusion of Ga and Cr into the Ag_Mo interface

6.5.4 Focussed Ion Beam

The Focussed Ion Beam (FIB) investigations were done at a focused ion beam work station 200 of the company FEI. In order to detect possible ridges in the droplets ahead of the Ag drop which are visible in Figure 6.29 cross-sections through these droplets were performed (Figure 6.38). Within the resolution limit of the FIB no ridges can be detected close to or under the droplets.

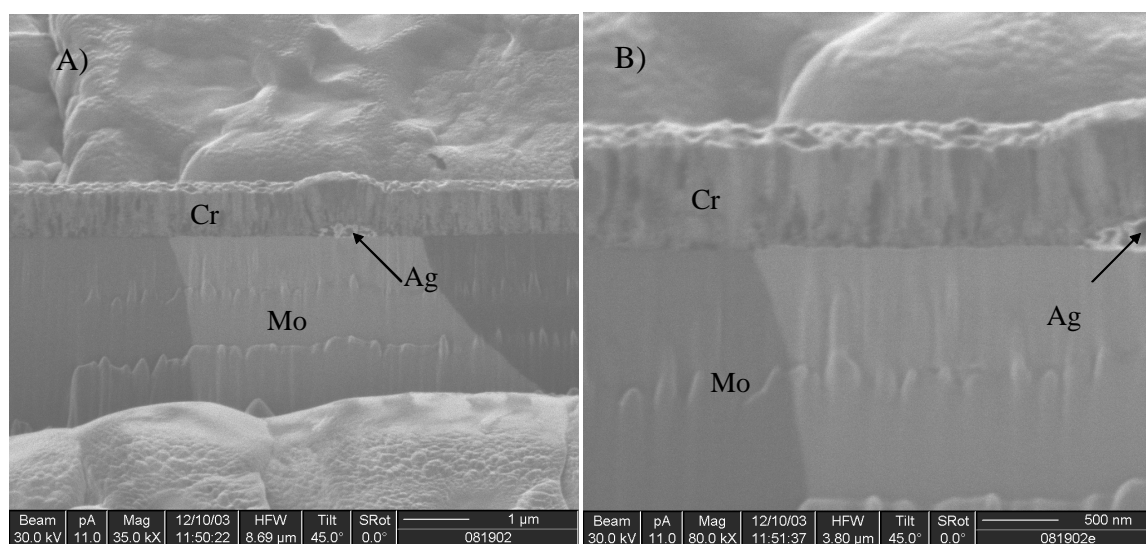


Figure 6.38: Cross-section through the Ag droplets, which are detected ahead of the Ag drop. No ridge was found within the resolution limit of the FIB.

6.5.5 Auger Spectroscopy

The Auger investigations were performed with an Auger JEOL: JAMP-7830 F on differently treated Mo substrates. In order to determine which impurities are introduced due to the annealing in the wetting furnace, Auger analyses were performed from electrolytically polished Mo substrates before and after annealing at 1070 °C for 1.5h in Ar/5% H₂ atmosphere. The results were compared with each other. As can be seen in Table 6.4.A, only S and Ca might be additionally introduced during the wetting experiment, C, N and O can result from the storage of the samples prior to the Auger measurements. However independent from their prior treatment, the impurities disappeared after removing 14nm from the Mo surface by sputtering.

To determine whether Ag adsorbed on the Mo substrate during the heating and equilibration process but prior to the wetting experiments, Auger analyses were performed from Mo substrates annealed under equilibrated and non-equilibrated conditions (Table 6.4.B). In order to investigate the Mo surface directly before the wetting experiment was performed, the polished Mo substrate was kept for 1h at 1290 °C in close proximity (1-2mm) to the liquid Ag drop and quenched afterwards for the equilibrated case. In the non-equilibrated case the polished Mo substrate was heated to 1290 °C, while the distance between the Ag drop and Mo substrate was 1-2cm. As soon as 1290 °C was reached the sample was quenched. The Auger analyses reveal that besides the impurities resulting from the storage and/or furnace atmosphere (C, O, N, S, Ca), no Ag adsorbate was found on the annealed Mo substrate either under equilibrated or non-equilibrated conditions (Table 6.4.B). The impurities vanished after sputtering the surface with Ar (500 eV) ions.

The Auger analyses of the Ag-Mo samples after the Mo sample was wetted with Ag are presented in Table 6.4.C. These wetting experiments were performed at 1070 °C under equilibrated and non-equilibrated conditions (see chapter 6.3). Figure 6.29 shows an SEM micrograph of the different areas studied on the Ag-Mo sample. As can be seen the Ag drop is surrounded by small droplets and nanodroplets. After removing the impurities resulting from the storage and/or furnace atmosphere by sputtering, the Auger analyses reveals that the small droplets which surround the main Ag drop are Ag droplets and the nanodroplets contain Ag as well as Mo. In contrast to the Mo substrate which was annealed in Ag vapor simulating the situation before the wetting experiment was performed, Ag adsorbate layer was found on the free Mo surface after it was wetted by Ag ahead of the Ag drop. On some of the samples the additional elements as Sb and Si were found.

6 Experimental results

Table 6.4 A: Comparison of surface investigation of differently treated Mo substrates before sputtering and after sputtering. A 14nm thick layer was sputtered from the Mo surface.

Treatment of the Mo substrate	Before sputtering	After sputtering (14nm)
electrolytically polished	Mo,(C, O)	Mo
Annealing Tempertature:1070°C, Annealing time : 1.5h Gas flow : Ar/5% H ₂	<u>Mo</u> ,(C, O, Ca, N, S)	Mo

Table 6.4 B: Auger investigations of the Mo substrates annealed under equilibrated and non equilibrated conditions. A 14nm thick layer was sputtered from the Mo surface.

Treatment of the Mo substrate	Before sputtering	After sputtering (14nm)
Annealing Tempertature:1290 °C, Annealing time : 2s Gas flow : Ar/5% H ₂ + Ag vapor non equilibrated	Mo, (C, O, Ca, N, S)	Mo
Annealing Tempertature:1290 °C, Annealing time : 1h Gas flow : Ar/5% H ₂ + Ag vapor equilibrated	Mo-substrate: Mo, (C, O, N) Ag-droplet: Ag,(S)	Mo substrate:Mo, Ag droplets: Ag

6 Experimental results

Table 6.4C: Comparison of surface investigation of Ag-Mo spreading experiments performed at 1070°C under different equilibration conditions. In all cases a gas flow of Ar/5%H₂ was used. An 8nm thick layer was sputtered from the Mo surface.

Conditions of the Ag-Mo spreading experiment	Before sputtering	After sputtering
<u>non equilibrated</u>	<u>Ag-drop</u> : Ag, Mo, (S, O) <u>Ag-droplets</u> : Ag, Mo Si, (O, Ca, C) <u>Mo substrate (smooth area)</u> : Mo, Ag, (O, C) <u>Mo substrate (rough area)</u> : Mo, Ag, (O, C) <u>Nano-droplets</u> : Ag, Si (O, C, Ca),	<u>Ag-droplets</u> : Ag, Mo, (Si), (O) <u>Mo substrate (smooth area)</u> : Ag, Mo
<u>equilibrated</u>	<u>Ag-drop</u> : Ag, Sb (S, C) <u>Ag-droplets</u> : Ag, Mo, Sb Si, (O, Ca, C, S) <u>Mo substrate (smooth area)</u> : Mo Ag, Sb (O, C, N), <u>Mo substrate (rough area)</u> : Mo, Ag, Sb, (O, C, N), <u>Nano-droplets</u> : Ag, Mo, Sb, (O, C, N)	<u>Ag-drop</u> : Ag <u>Ag-droplets</u> : Ag, Mo, Si, O, Ca <u>Mo substrate (smooth area)</u> : Mo, Ag <u>Mo substrate (rough area)</u> : Mo, Ag <u>Nano-droplets</u> : Mo, Ag

The Auger analyses of the Ag- single-crystal Mo(110) wetting experiment performed at 1070 °C before sputtering are shown in Table 6.5.

6 Experimental results

Table 6.5: Auger analyses of the Ag- Mo(110) wetting experiment performed at 1070 °C before sputtering are presented

area	Elements
Ag drop	Ag, O, Sb, S
Mo (smooth area)	Mo, O, Sb, N, C
Mo (rough area)	Mo, O, Sb, N, C
droplets	Mo, O, Sb, N, C, Si,, Ca
Nano-droplets	Mo, O, Sb, N, C Si,, Ca

7 Interpretation and discussion

7.1 Spreading kinetics

In this section the Ag-Mo high-temperature wetting data are compared to the equations of the fluid flow model and the molecular-kinetic model. The goal is to show whether high temperature spreading can be understood in terms of one of these models.

In the Figures 7.1-7.10 the dynamic contact angle is plotted against the capillary number for the experiments with liquid Ag on polycrystalline- Mo, single crystalline Mo(110), and Mo(100), performed at a variety of temperatures. Also plotted are the calculated curves using the molecular kinetic model and the fluid flow model. All the experimental curves show a similar kinetic behavior at different temperatures. The contact angle decreases strongly with decreasing capillary number. The spreading velocities $v=[dR(t)/dt]$ are between 0.1 and 0.6 m/s. Similar spreading velocities have been observed for low-viscosity liquids like metals at high temperatures as for example molten Sn on a Mo or Ge substrate using a drop transfer set up {Naidich, Y., 1972},{Naidich, Y., 1992}.

The velocities expected with the fluid flow model are estimated in the following way: It is known that the radius of the drop is of the order of 1mm. The capillary length (L) in equation (2.31) has to be of the order of this value. The slip length L_S is estimated as not being smaller than the interatomic distance ($\approx 1 \text{ \AA}$), or greater than the radius of the drop itself, leading to $1 \text{ \AA} < L_S < 1 \text{ mm}$. Under these conditions the data points of the measured velocities should be between the lines for the Fluid Flow Model fit in Figures 7.1-7.10. This was not observed in the experiments. L/L_S would have to be much lower

than 10^{-10} for the data points to fit into this band. This means that L_S has to be smaller than 1 \AA , which is physically not reasonable. Therefore, it is concluded that the fluid flow model does not describe the Ag–Mo wetting data for the fastest spreading velocities and that viscous impedance is not the main source of energy dissipation during the spreading of liquid silver. The molecular model, on the other hand, does describe the fastest velocity data well. This is consistent with a spreading kinetics controlled by the friction of the moving triple junction. The activation free energy ΔG is between 95–145 kJ/mol. The frequencies K_ω are around 10^8 s^{-1} . The reported value for the surface diffusion energy {Seebauer, E.G., 1995} and the one calculated in this work (chapter 6.4) are comparable and on the order of 100 kJ/mol. The activation energy for surface desorption in metal-metal systems is of the order of 1000 kJ/mol {Seebauer, E.G. 1995}. The calculated wetting activation free energy for the Ag-Mo system is lower than the activation free energy for surface desorption but of the same order of activation energies for surface diffusion reported in the literature. Hence, the rate-determining step for wetting seems to be surface diffusion rather than adsorption and desorption. Ruijter et al. {de Ruijter, M.J.,2000} proposed a theory which combines the fluid flow model and the molecular kinetic model. According to this model, for systems far away from equilibrium the molecular kinetic model should fit the spreading data and for systems which are close to the equilibrium or at very long time the fluid-flow model should apply. Figures 7.1 - 7.10 show that at the fastest spreading velocities and at contact angles which are far away from equilibrium the molecular model describes the experimental data.

It should be noted that at the reported velocities typically inertia effects become relevant which, for example, leads to overshooting as shown in Figure 6.1.B. However, these inertia effects do not influence the kinetics nor change the conclusions presented in this work since experiments with different masses / sizes of Ag drops showed identical results within the accuracy.

7 Interpretation and discussion

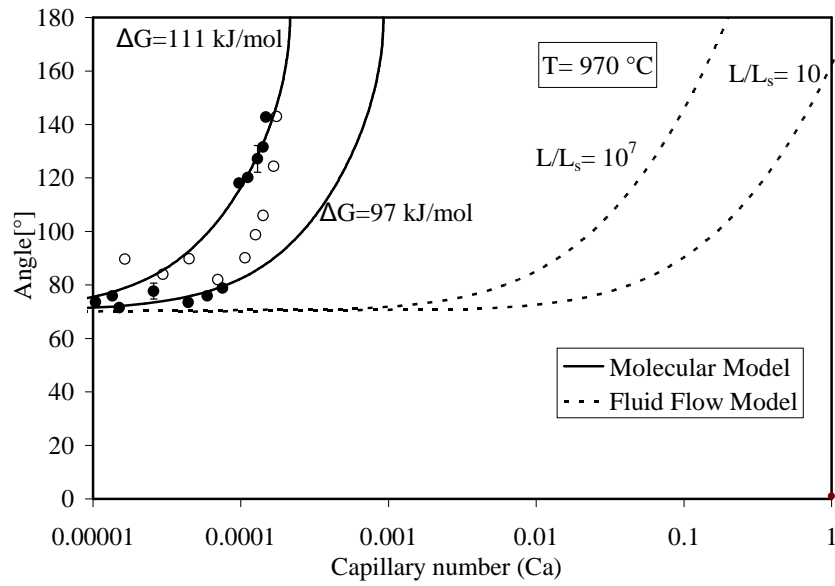


Figure 7.1: The data points representing the evolution of the contact angle of the Ag drop on polycrystalline- Mo plotted against the capillary number at 970 °C are compared with the fluid flow (dotted line) and the molecular kinetic model (line). The molecular kinetic model describes the experimental data

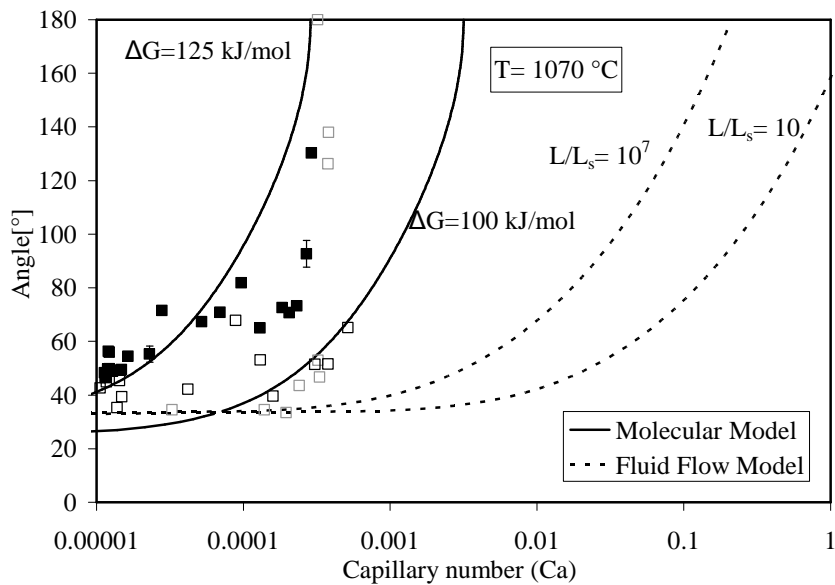


Figure 7.2: Comparison of the angle - capillary number dependency of the liquid Ag drop on polycrystalline- Mo at 1070 °C to the curves calculated using the molecular kinetic and the fluid flow model.

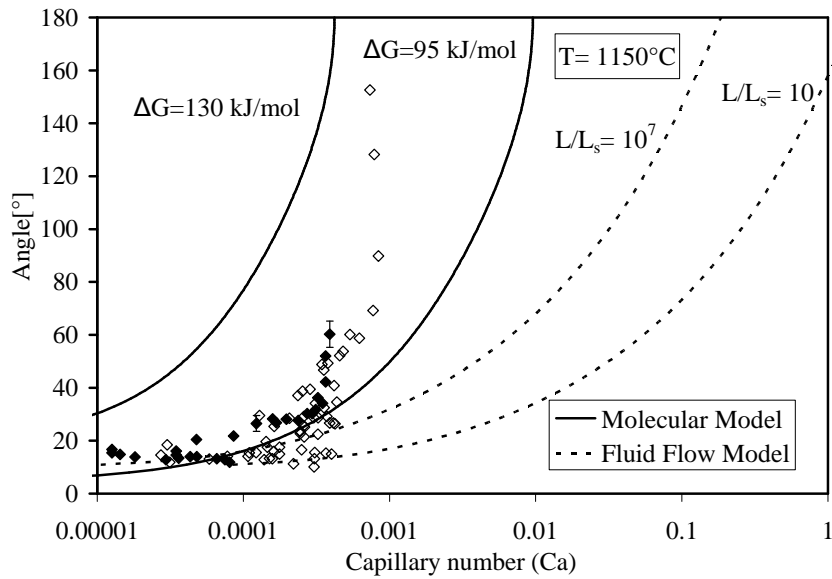


Figure 7.3: The contact angle of the Ag drop on polycrystalline- Mo is plotted as a function of the capillary number. The experiment was performed at 1150 °C. The data points are compared to the molecular kinetic model and the fluid flow model.

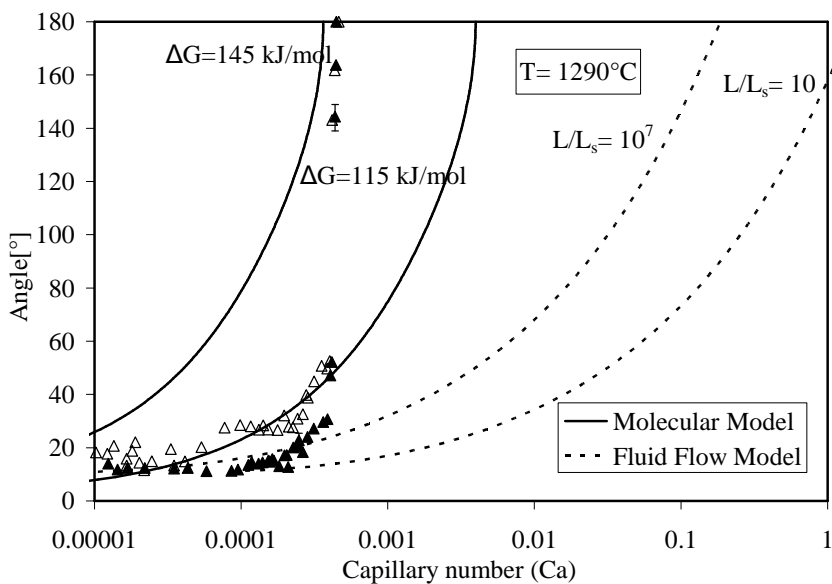


Figure 7.4: Evolution of the contact angle of the Ag drop on polycrystalline- Mo as a function of the capillary number at 1290 °C. The fast spreading velocities of the experiment can be described with the molecular kinetic model while for the lower velocities the fluid flow model applies.

7 Interpretation and discussion

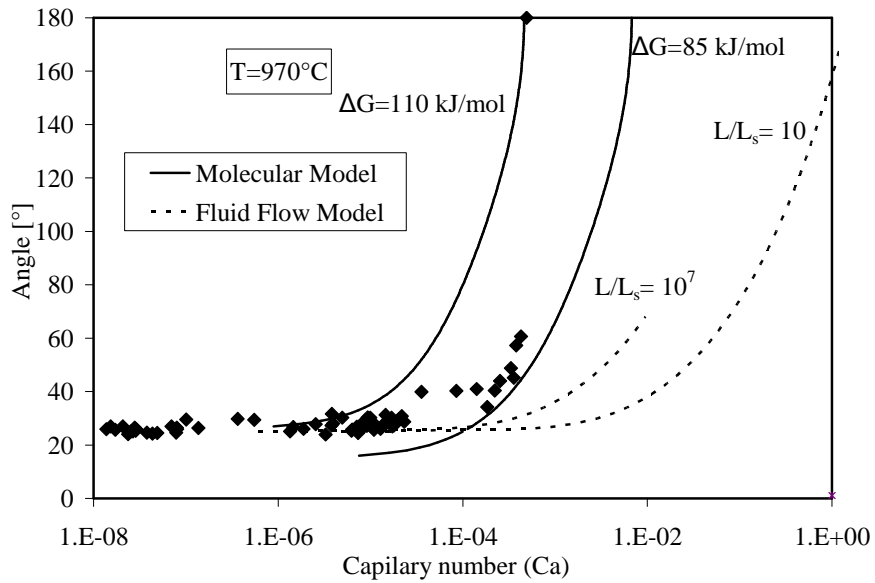


Figure 7.5: Contact angle - capillary number dependency of the Ag drop on single crystalline Mo (110) at 970 °C. The data can be described with the molecular kinetic model.

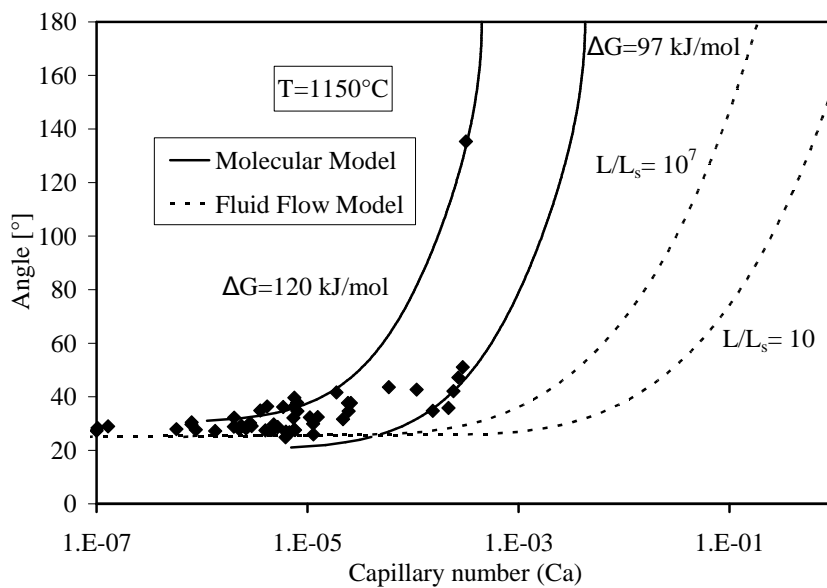


Figure 7.6: The contact angle of the Ag drop on single crystalline Mo(110) is shown as a function of the capillary number at 1150 °C and compared with the molecular kinetic model and the fluid flow model.

7 Interpretation and discussion

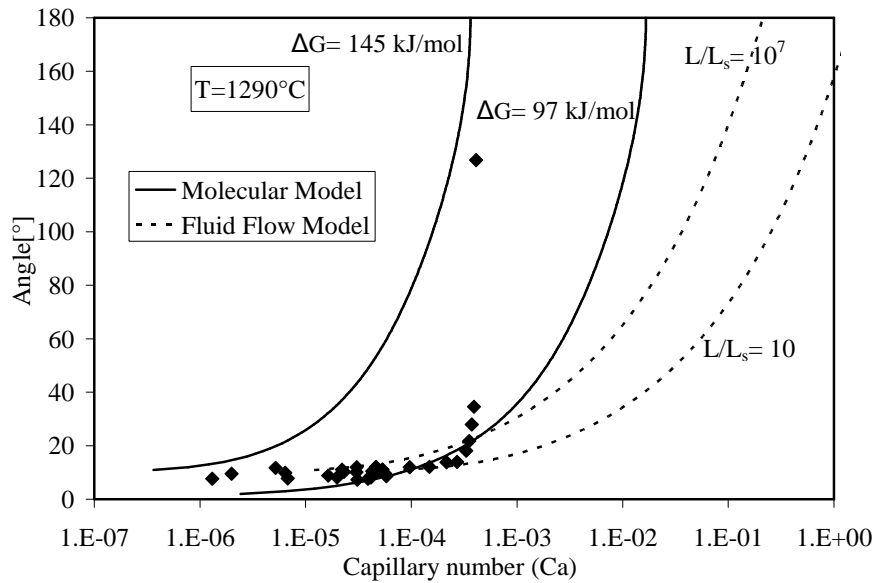


Figure 7.7: Evolution of the contact angle of the Ag drop on single crystalline Mo(110) as a function of the capillary number at 1290°C and comparison to the calculated curves predicted by the molecular kinetic and the fluid flow model.

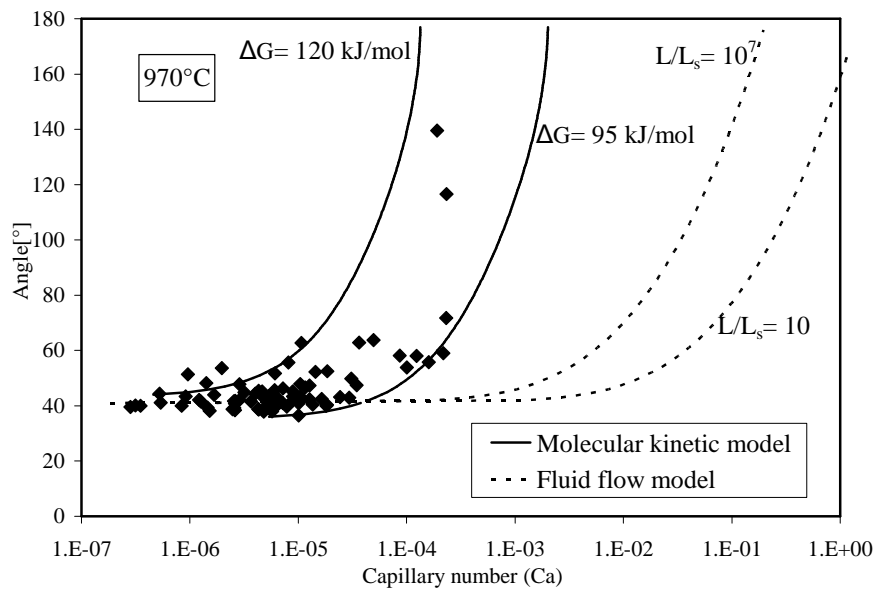


Figure 7.8: The contact angle of the Ag drop on single-crystalline Mo(100) is plotted as a function of the capillary number. The experiment is performed at 970°C . The data points are compared with curves predicted by the molecular kinetic model and the fluid flow model.

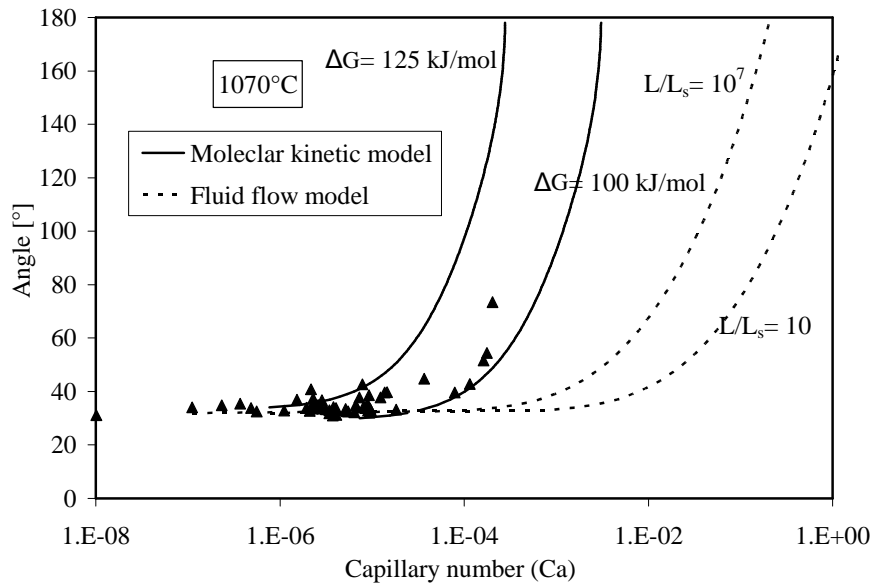


Figure 7.9: Comparison of the angle - capillary number dependency of the liquid Ag drop on single crystalline Mo (100) at 1070 °C with calculated curves using the molecular kinetic and the fluid flow model.

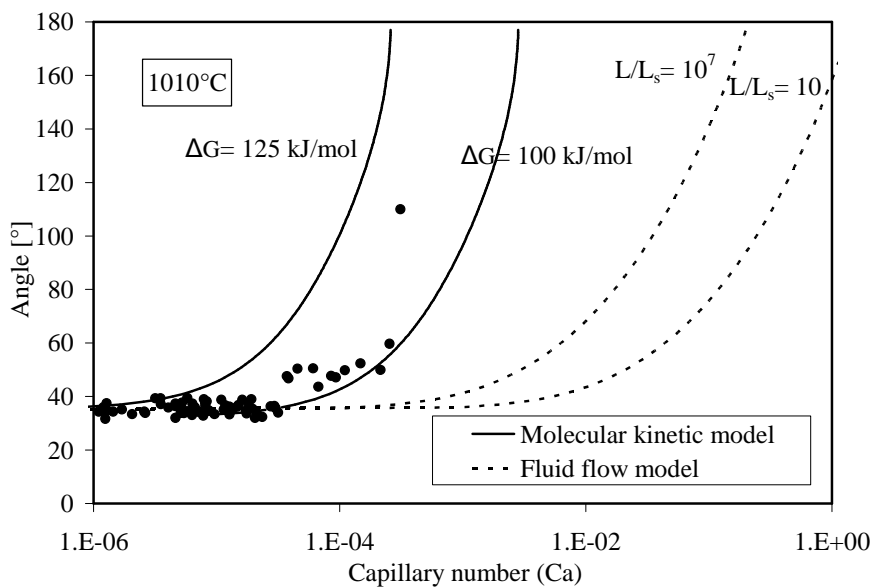


Figure 7.10: The contact angle of liquid Ag on Mo(100) is plotted versus the dimensionless capillary number and compared with the models valid for low-temperature wetting.

7.2 Effect of roughness on the spreading kinetics

Eick et al. and Neumann et al. showed that a contact angle hysteresis is in general attributed to surface roughness or chemical inhomogeneities (A.W. Neumann, R.J. Good, 1972), (J. D. Eick, 1975). To study the effect of roughness, receding and advancing angles were measured for Ag on Mo substrates at different temperatures. As described in chapter 6.2 the receding angle overshoot during the heating process and became an advancing angle. This, and the fact that similar final angles were reached with different polishing procedures and therefore different surface roughness (Table 6.1.B), demonstrates that the surface roughness of the Mo substrates does not influence the final contact angle or the spreading kinetics in the experiments performed.

7.3 Effect of equilibration on spreading and the final contact angle

As is shown in Figure 6.13 the non-equilibrated final angle for liquid Ag on polycrystalline Mo is greater than the equilibrated angle at each temperature. The difference between equilibrated and non-equilibrated final angles in the case of the polycrystalline substrate is about 10° for all temperatures with the exception of a difference of 50° at 1150°C . However, the spreading kinetics are similar in all cases (Figures 6.14.-17), and can be described using the molecular kinetic model. This implies that friction at the triple junction is the main source of energy dissipation during spreading. The slightly faster spreading kinetics at higher temperatures in the equilibrated experiments compared to the non-equilibrated ones can be explained by the presence of small Ag drops on the Mo surface after equilibration and prior to the wetting experiment (Figure 6.18). The area coverage of the Ag drops increases with increasing temperature in the equilibrated experiments. This is shown in Table 6.2. While the liquid Ag front spreads over the surface, it sweeps the Ag drops which are on the substrate reducing the friction of the triple line. This effect will be more obvious the more Ag drops are on the Mo substrate. Since there are no Ag drops on the Mo substrate in the non-equilibrated case (Figure 6.18), the spreading kinetic is slower than that for

the equilibrated case. A comparison of Figures 6.14-6.17 shows that the difference in the spreading kinetics is more distinct at higher temperatures due to the larger number of drops at higher temperatures.

The effect of ‘dry’ wetting (dry “spreading”) (see chapter 2.3.1.) {Cannon, R.M. 1995}, where an equilibrium Ag adsorbate layer on the Mo substrate prior to the spreading would result in a higher contact angle compared to spreading on a clean substrate, cannot explain the higher final angle in the equilibrated experiments. The adsorbate would be expected in the equilibrated case but the higher contact angle was found in the non equilibrated experiments. Additionally, an Auger analysis revealed that no Ag adsorbate is present on the Mo substrates (see Table 6.4B) prior to spreading. After the wetting experiment however Ag adsorbates were found (see Table 6.4C).

In order to explain the higher final angle after equilibration either the energies γ_{LV} and / or γ_{SL} would have to be larger or the surface energy γ_{SV} would have to be lower when compared to the non–equilibrated situation.

Impurities on the Ag surface could reduce the surface energy γ_{LV} . An Auger analysis showed that the substrates before spreading as the Ag drops after spreading had S impurities at the surface (see Table 6.4B and C). These impurities originate from the furnace since an OIM study of the Ag and the Mo showed no S impurities in these materials prior to their treatment in the furnace (Table 5.1-5.2). The difference in the final angles however cannot be explained by the S impurities since they are found in both equilibrated and non equilibrated experiments.

An adsorbate on the Mo substrate would decrease the surface energy γ_{SV} . In order to explain the higher contact angle in the non equilibrated case such an adsorbate should be present in the non equilibrated experiment but must be reduced in the equilibrated situation.. After Allen et al. {Allen, B.C., 1972} a layer of oxygen on a Mo substrate will vanish at a total pressure of 10^{-7} Pa only at temperatures above 1000 °C by volatile oxide formation. Although the reducing atmosphere Ar/5%H₂ ensures that the substrate has no oxide layer it is conceivable that in the non equilibrated experiments oxygen on the Mo surface present prior to the experiment might not be fully desorbed. This would lead to a decrease in γ_{SV} and a higher final angle in the non equilibrated cases. This

reasoning is also supported by the fact that the final contact angle increases with decreasing hydrogen content (Figure 6.3).

7.4 Effect of temperature on the final contact angle

Figures 6.9 and 6.13 show that the final angle of liquid Ag on Mo single crystal as well as on polycrystalline Mo decreases with increasing temperature under all experimental conditions. The strongest decrease of the final angle is observed on polycrystalline Mo substrates between 970 °C and 1070 °C, as shown in Figure 6.13 and Table 7.1.

According to Young's equation (2.1.b) either γ_{LV} has to decrease or $(\gamma_{SV} - \gamma_{SL})$ has to increase with temperature in order to explain the observed effect. After Keene {Keene, B.J., 1993} the temperature dependence of the surface energy γ_{LV} of liquid Ag is

$$\gamma_{LV} = 925 \text{ mN/m} - 0.21 \text{ mN/Km} (T - 960 \text{ °C}) \quad (7.1).$$

Thus γ_{LV} decreases from 922.9 mN/m for 970 °C to 855.7 mN/m at 1250 °C. This results in a decrease in the final angle of only 0.5° and therefore cannot explain the observed decreases in the final angle. The change of the final angle from 970 °C to 1290 °C is, for example, 70° for the polycrystalline substrate. The data by Chatain et al suggest that hydrogen adsorption does not affect the liquid silver surface energy γ_{LV} {Chatain, D, 1994}. The other surface energies γ_{SV} or γ_{SL} should also vary with temperature. In Table 7.1, 7.2 and 7.3, the values for $(\gamma_{SV} - \gamma_{SL})$ between 970 °C and 1250 °C and for different substrates are summarized. Differences smaller than 100 mN/m are typical except for the polycrystalline substrate between 970 °C and higher temperatures.

According to Allen {Allen, B.C., 1972} the interfacial energy γ_{SL} can be expressed as

$$\gamma_{SL} = -\frac{RT \ln X}{4A_M} \quad (7.2),$$

where X is the mole fraction of solid in the liquid phase, A_M the molar area and R the gas constant. With {Eustathopoulos, N., 1999}

$$X \cong K \exp\left[\frac{-\lambda}{RT}\right] \text{ and } K = \exp\left[-W\left(1 - \frac{T}{T_m}\right)/RT\right] \quad (7.3)$$

where λ is the regular solution parameter and W is the heat of melting, the interfacial energy γ_{SL} becomes

$$\gamma_{SL} \cong \frac{\lambda}{4A_M} + \frac{W}{4A_M} \left(1 - \frac{T}{T_m}\right) \quad (7.4)$$

The interfacial energy γ_{SL} decreases with increasing solubility and temperature according to equations (7.2) and (7.3). Liquid Ag on Mo shows only a small increase of X from 0.3 to 1.2 at% with increasing temperature from 970 °C to 1290 °C. According to Allen et al. {Allen, B.C., 1972} the surface energy γ_{SV} of Mo is 1750 mN/m at 1600 °C. Using this value and equations (7.2)-(7.4), $\Delta\gamma_{SL}$ results in a decrease of about 40 mN/m which is sufficient to explain the difference in the final angle except for the polycrystalline substrate. One has to keep in mind that the error in the angle measurement of $\pm 3^\circ$ results in an uncertainty for (γ_{SV} - γ_{SL}) of about ± 20 mN/m.

The strong increase of $\Delta(\gamma_{SV}$ - $\gamma_{SL}) \approx 700$ mN/m for the polycrystalline substrate from 970 °C to 1070 °C is neither explained by changes of the interfacial energy, γ_{SL} , nor by changes of the surface energy γ_{LV} of the liquid Ag. In general, the surface energy γ_{SV} of a solid metal has a negative temperature gradient $d\gamma_{SV}/dT$ {Allen, B.C., 1972}, {Keene, B.J., 1993}. Nevertheless positive temperature gradients have been reported and are attributed to the presence of surface active impurities or adsorbates {Allen, B.C., 1972}. Pique et al. {Pique D., 1981} showed a decrease in contact angle in the system of liquid Ag on Fe from 40° to 12° in a temperature range between 975 °C and 1150 °C. For this system it was argued that at lower temperatures Ag adsorbs on the Fe substrate and desorbs with increasing temperature. Therefore, γ_{SV} increases with increasing temperature and Pique et al. {Pique D., 1981} related this increase in γ_{SV} to the decreasing final contact angle. Ag and Fe are insoluble and no reaction is expected. In the present study of liquid Ag on Mo no Ag adsorbate layer was observed on the Mo prior to the wetting experiment (Table 6.4B) and thus the decrease of the contact angle with temperature cannot be explained by adsorption and desorption of Ag.

Allen et al. {Allen, B.C., 1972} reported that at a total pressure of 10^{-7} Pa an oxygen layer on the Mo surface is only removed above 1000 °C by volatile oxide formation. Although in the experiments of this work the reducing atmosphere Ar/5% H_2 in the furnace ensures that the substrate has no oxide layer it is conceivable that oxygen on the Mo polycrystalline substrate, present prior to the experiment might not be fully desorbed at 970 °C. This would lead to a decrease in γ_{SV} and a higher final angle. Furthermore it might be conceivable that the free energy of adsorption for oxygen is larger at the grain boundaries of the polycrystalline Mo compared to the surfaces explaining why the single crystalline substrates do not show the same effect.

A change of the surface energy γ_{SV} due to the hydrogen in the furnace atmosphere is ruled out because of the following reasons. Reconstruction of the Mo surface was reported in the temperature range $373\text{ °C} < T < 623\text{ °C}$ with hydrogen coverage up to saturation {Prybyla, J.A., 1991}. Due to the reconstruction, a decrease in surface energy is expected with increasing temperature. The reported wetting experiments however are all performed at temperatures above 970 °C where we expect full reconstruction without any further change with temperature. Mo–H phases are observed at high pressures (>3 GPa) and temperatures up to 500 °C {Fukai Y, 2003}, {Antonov, V.E, 2004}. In this temperature and pressure range, α , β , and ϵ phases exist, with bcc, hcp, and fcc, structure, respectively. A compound formation of the Mo–H at the experimental conditions used in this study is not expected.

7 Interpretation and discussion

Table 7.1: Final angle θ of liquid Ag on polycrystalline Mo (equilibrated) and surface energies γ_{LV} and $(\gamma_{SV} - \gamma_{SL})$ at 970 °C , 1070 °C, 1150 °C, 1290 °C are shown. The surface energy γ_{LV} was calculated with equation (7.1) after Keene {Keene, B.J., 1993}¹.

Temperature[°C]	Final angle θ , [°]	γ_{LV} [mN/m]	$(\gamma_{SV} - \gamma_{SL})$ [mN/m]
970	83.3	922.9	99
1070	25.6	901.9	813
1150	13.5	885.1	860
1290	10.8	855.7	840

Table 7.2: The final contact angle of Ag on Mo(110) as well as the surface energies γ_{LV} and $(\gamma_{SV} - \gamma_{SL})$ are listed at 970 °C , 1070 °C, 1150 °C, 1290 °C. The surface energy γ_{LV} was calculated with equation (7.1) after Keene {Keene, B.J., 1993}.

Temperature[°C]	Final angle θ , [°]	γ_{LV} [mN/m]	$(\gamma_{SV} - \gamma_{SL})$ [mN/m]
970	21	922.9	861
1070	17	901.9	862
1150	12	885.1	865
1290	9	855.7	844

Table 7.3: The change of the surface energies γ_{LV} and $(\gamma_{SV} - \gamma_{SL})$ and the final contact angle at 970 °C , 1010 °C, 1070 °C, are shown for Ag on Mo(100). The surface energy γ_{LV} is determined with equation (7.1) after Keene {Keene, B.J., 1993}.

Temperature[°C]	Final angle θ , [°]	γ_{LV} [mN/m]	$(\gamma_{SV} - \gamma_{SL})$ [mN/m]
970	41.7	922.9	689.07
1010	35.7	914	742.24
1070	30	885.1	766.51

¹ At 970°C the final angle found in the sessile drop experiment were lower than the finale angle found in the drop-transfer experiment. Using the result of the sessile drop experiments we find $(\gamma_{SV} - \gamma_{SL}) = 418$ mN/m.

7.5 Effect of Mo surface orientation on the final angle

As shown in Figure 6.9. the final contact angle depends on the orientation of the Mo substrate. Naidich et al. {Naidich, Y., 1981} reported for Ge melt on Ge substrates contact angles for (111), (110) and (100) planes. Closer packed planes have a lower surface energy leading to higher contact angles resulting in $\theta_{(111)} > \theta_{(110)} > \theta_{(100)}$. Mo has a bcc structure and therefore Mo(110) is the closest-packed plane and has the lowest surface energy. However, the contact angle of the Ag drop on a single crystalline Mo (110) is lower than the contact angle on single crystalline Mo(100) for the investigated temperatures of 970 °C and 1070 °C (Figure 6.9.). By far the highest contact angle was observed in the experiment at 970 °C for wetting on a polycrystalline Mo substrate. At 1070 °C the final angle for Ag on the polycrystalline Mo is in between the values for the single crystals and at the two highest investigated temperatures of 1150 °C and 1290 °C the measured final angles for the polycrystalline–Mo and single crystalline Mo(110) are identical within the experimental uncertainty (Figure 6.9).

Che et al. {Che J.G., 1998} calculated a surface energy of Mo(100) of 3.34 J/m² and of Mo(110) of 2.92 J/m² at 0K. This difference of 13% in surface energy should decrease as temperature increases {Staumal, B., 2005}. Nevertheless it would result in a higher contact angle for Ag on Mo(110) in contradiction to the experimental results of the present work. According to Prybyla et al. reconstruction of the Mo surface takes place in a hydrogen atmosphere at temperatures ranging from 373 °C to 623 °C with hydrogen coverage up to saturation {Prybyla, J.A., 1991}. At the temperatures used for the wetting experiments one thus expects fully reconstructed surfaces. It might be conceivable that due to reconstruction the surface energy reduces more strongly for surfaces with higher surface energy. Thus the Mo(100) surface might reduce its surface energy due to reconstruction below the Mo(110) surface energy explaining the experimental findings.

Besides the surface energy of the Mo substrates the interfacial energy between the Mo substrate and the Ag drop might differ for different orientations as well. From the data one can deduce that the difference $\gamma_{SV} - \gamma_{SL}$ for Ag on Mo(110) has to be higher than on Mo(100) (Table(7.1)-(7.2)). Therefore,

$$\gamma_{SV}^{100} - \gamma_{SL}^{100} < \gamma_{SV}^{110} - \gamma_{SL}^{110} \quad (7.5)$$

which leads to:

$$\Delta\gamma_{SL} = \gamma_{SL}^{100} - \gamma_{SL}^{110} > \Delta\gamma_{SV} = \gamma_{SV}^{100} - \gamma_{SV}^{110} \quad (7.6).$$

Thus a difference of the interfacial energies for the two orientations larger than for the surface energy could explain the experiments.

Since at temperatures between at 970 °C and 1070 °C the surface energies of different faces of Mo differ we expect that the surface energy of the polycrystalline substrate ranges between the values for the various faces but will be different from any value for a specific face. Thus different final angles on the polycrystalline substrates are expected as seen at 1070 °C. At the higher temperatures, 1150 °C and 1290 °C, the final angles are comparable for the different substrates. A possible explanation for the experiment at 970 °C was proposed in the last section as being due to the oxygen on the substrate not being fully desorbed.

7.6 Grooving experiments of Mo

As mentioned earlier the grooving of polycrystalline- Mo experiments were performed in order to calculate the surface diffusivities that will control the ridge formation. The diffusion coefficients are the result of fitting Mullins equation (2.56) to the measured data in Figure 6.20. The Mullins constant as well as the diffusion constant are listed in Table 7.4 Gjostein et al. {Gjostein, N.A., 1963} determined the interfacial diffusion coefficient for Mo as $4 \cdot 10^{-14} \text{m}^2/\text{s}$ at 1000°C. The determined diffusion coefficients in this work are in the same range as reported in the literature {Gjostein, N.A., 1963}

Table 7.4: The Mullins constant and the Interfacial diffusion coefficient were determined for different temperatures

Temperature [°C]	Mullins constant B [m ⁴ /s]	Interfacial diffusion coefficient D[m ² /s]
1070	$2.01 \cdot 10^{-32}$	$8.70 \cdot 10^{-15}$
1150	$2.09 \cdot 10^{-31}$	$9.76 \cdot 10^{-14}$
1250	$3.32 \cdot 10^{-31}$	$1.73 \cdot 10^{-13}$

7.7 Influence of ridge formation on the spreading kinetics

Saiz et al. {Saiz, E., 1998} found that especially in high-temperature wetting systems like liquid metals on ceramic substrates ridge formation plays an important role. In systems which are able to form ridges, these can control the spreading kinetics depending on the size of the ridge compared to the radius of the drop curvature and the ridge growth velocity compared to the spreading velocity {Saiz, E., 1998}. Therefore the formation of a ridge in the Ag-Mo system was investigated.

The diffusion coefficient, which was determined from the Mo grooving experiments (see chapter 6.4) was used to determine the critical spreading velocity ($v_{cr} = 6D_{sl}/a$) beyond which ridge formation cannot take place. It is assumed that the substrate is completely flat, and that there is no initial perturbation for ridge growth {Saiz, E., 1998}.

In Figures 7.11-7.13 the contact angle is plotted versus the capillary number. The plots show the measured angle-velocity dependency at different temperatures (1070°C, 1150°C, and 1290°C). The vertical line in each plot represents the critical spreading velocity beyond which ridge formation is not possible. It can be seen that at the fastest spreading velocities ridge formation can not occur in either of the wetting experiments. Therefore, ridge formation does not seem to influence the spreading kinetics in the case

where no initial perturbation exists. However, if there is an initial perturbation on the Mo substrate the question arises of how small a ridge has to be in order to be able to move with the liquid front at the reported spreading velocities. Mullins equation (see chapter 2.4.2) and the boundary conditions proposed by Saiz et al. {Saiz, E 1998} can be used to determine the velocity of a ridge depending on its height:

$$v_{ss}^{adv} = B_{sv} \left(\frac{\tan(\pi - \phi_s)}{h} \right)^3.$$

The plots (Figures 7.14-7.16) represent the velocity

dependence on the ridge height for 1070°C, 1150°C, and 1290°C. Since no ridge in the Ag-Mo experiments was observed either by SEM or TEM, the dihedral angle of the ridge was estimated from literature values. Φ was chosen to be between 90°-140° (Figure 7.14-16). Using these values v_{ss}^{adv} was calculated and is plotted in Figures 7.14-16.

Under these conditions a ridge which moves with the liquid front would have to be much smaller than 1nm for all the temperatures used in the experiments. Thus, the spreading kinetics at the fastest reported velocities is not influenced by ridge formation under the chosen experimental conditions.

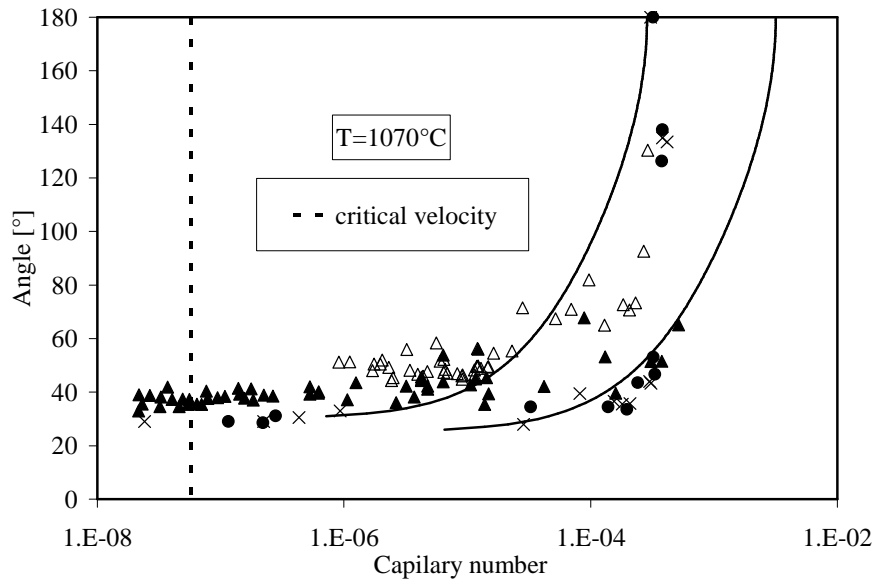


Figure 7.11: Evolution of the contact angle of the Ag drop on polycrystalline- Mo as a function of the capillary number at 1070°C. Also plotted is the critical velocity beyond which ridge formation is not possible.

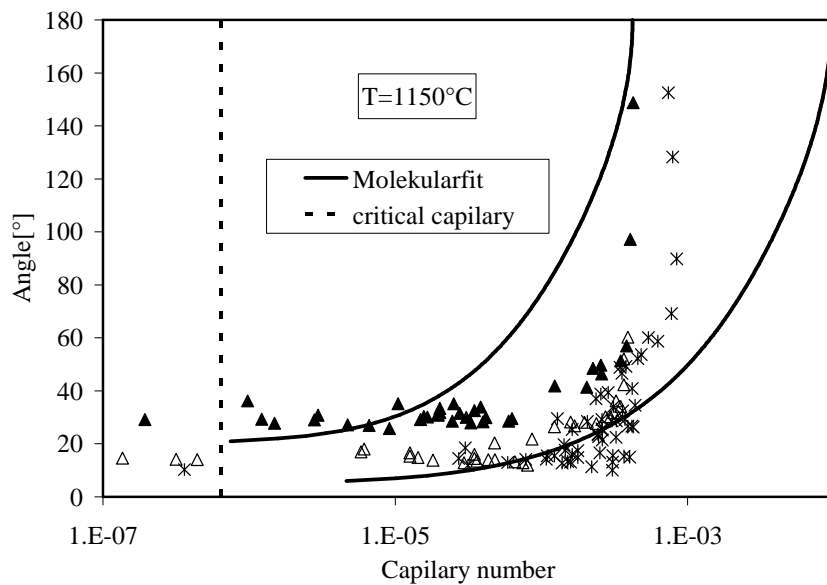


Figure 7.12: The critical velocity, beyond which ridge formation is not possible and the contact angle of the Ag drop on polycrystalline- Mo in dependence of the capillary number is plotted for 1150°C.

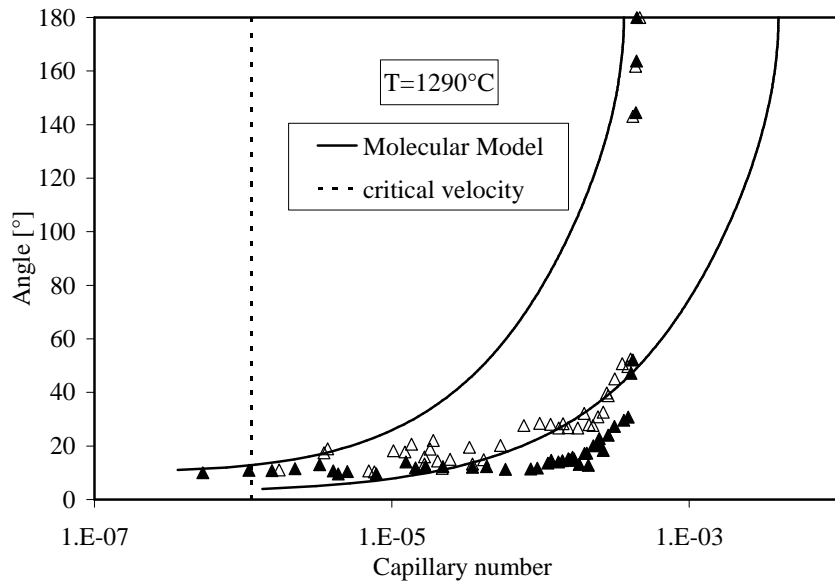


Figure 7.13: Evolution of the contact angle of the Ag drop on polycrystalline-Mo as a function of the capillary number at 1290°C and critical velocity, beyond which ridge formation is not possible.

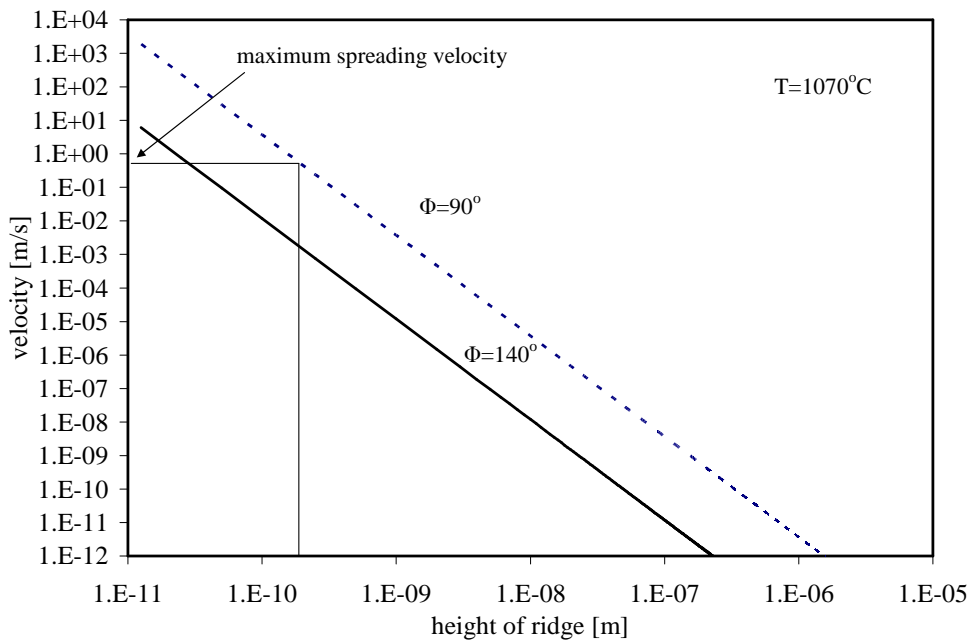


Figure 7.14: Maximum velocity of a ridge as a function of its height at 1070°C.

7 Interpretation and discussion

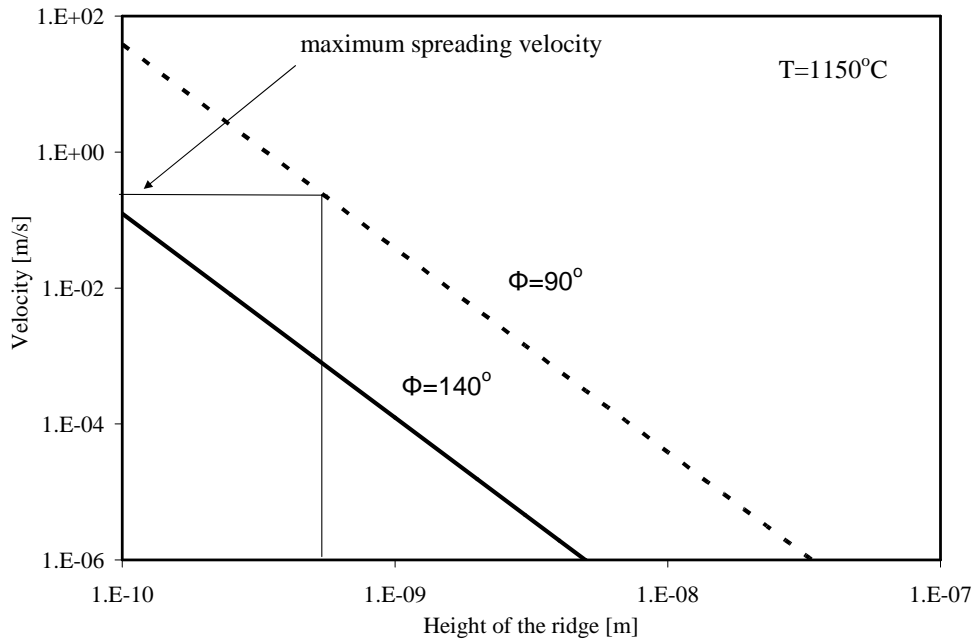


Figure 7.15: The maximum velocity of a ridge in dependency of its height is plotted for $\Phi=90^{\circ}$ and $\Phi=140^{\circ}$ at 1150°C .

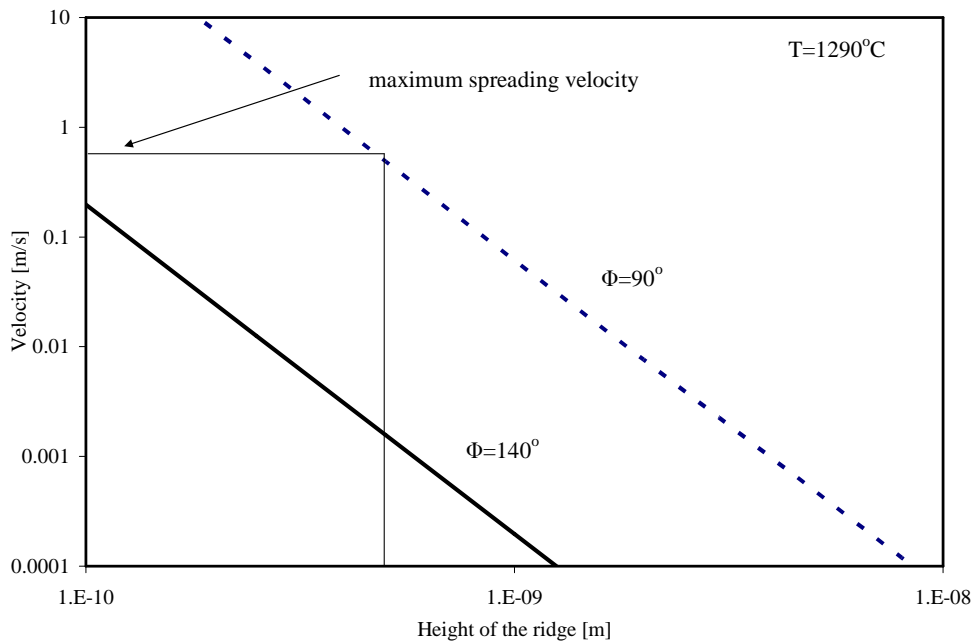


Figure 7.16: Maximum velocity of a ridge versus its height is shown at 1290°C .

7.8 Interfacial characterizations

In the last section it was shown that ridge formation is not possible at the fastest reported spreading velocities if there is no initial perturbation acting as a ridge. Where an initial perturbation exists the ridge would have to be much smaller than 1nm in order to move with the liquid front at the fastest reported velocities. Nevertheless, ridge formation might still occur while the system is equilibrating for 0.5h after spreading. This equilibrating was done in order to determine the final contact angle. AFM, SEM and TEM investigations were performed on those samples which were equilibrated for 0.5h after the wetting experiment in order to detect possible ridge formation.

SEM and Auger investigations showed a ring of small silver droplets surrounding the main Ag drop approximately 6 μm ahead of it. (Figure 6.24 A-C). Auger analyses showed that these droplets are small Ag droplets (see chapter 6.5.5). It seems that these Ag droplets form because the liquid silver front overshoots during spreading due to inertia. The velocity of the liquid front is very fast and advances with a velocity of about (0.3-0.5 m/s). As a consequence it can overshoot for a few microns and recede again leaving a ring of small Ag droplets. A hint for such an overshooting can be seen in the Figure 6.1.B, which shows an oscillation in the contact angle as in the radius over time. After the Ag drop receded and reached its final angle the sample was quenched. It is then expected that the Ag drop receded further due to thermal shrinkage. If a ridge formed after the drop reached its final angle the triple line might have broken off the ridge during thermal shrinkage. However no ridge was detected by AFM (resolution of 1nm) in the area between the small silver drops and the main Ag drop. Also no ridges were detected in the SEM and TEM cross-sections—within their detection limits. FIB investigations performed at the small droplet ahead of the Ag drop also did not show evidence of a ridge (Figure 6.38). This manifests the fact that ridges did not form either at the fastest velocities or for 0.5 hours after the liquid front stopped. Thus, ridge formation does not influence the spreading kinetics or the final angle of the wetting experiments performed of Ag on polycrystalline- Mo at the chosen experimental conditions.

8 Summary

Because of the great technological importance of high-temperature wetting many studies have been performed to investigate the spreading of molten metals and oxides on different substrates. Whereas low-temperature wetting can be well described using already established models the theoretical analysis of high-temperature systems is complicated by the fact that the substrate can not be approximated as ideally rigid and insoluble. In addition, the effects of adsorption and interfacial reaction have to be taken into account. Since atmosphere and temperature control are required, high-temperature experiments are challenging.

In this work a drop-transfer system, which allows analyzing isothermal spreading and avoids complicated effects related to melting and equilibration, has been used to study high-temperature spreading ensuring appropriate atmosphere and temperature control. The spreading kinetics of a model system (liquid Ag on polycrystalline Mo and single-crystalline Mo (110) and Mo (100)) was investigated. Ag–Mo is a system with a simple eutectic phase diagram without intermetallic phases. Consequently no chemical reactions are expected during spreading.

In order to unveil the basic phenomena controlling spreading in metal–metal systems, the observed spreading kinetics in the Ag–Mo system were compared with current theories of low-temperature spreading. The dynamic wetting in low-temperature systems has been analyzed from the perspectives of hydrodynamics (fluid flow model) and atomistic mechanisms (molecular kinetic model). Analyses of the spreading data reveal that the molecular model does describe the data well for all the investigated systems. Therefore, most of the energy dissipation during spreading is due to friction of the triple line rather than viscous impedance in the liquid. A comparison of the measured free activation energy for wetting of $\Delta G \approx 95\text{--}145$ kJ/mol with literature

values indicates that the rate-determining step is the surface diffusion of the silver atoms. The observed spreading kinetics was independent from the equilibration state of the system, the temperature, and the Mo orientation. However, the final contact angle showed a dependency on all these factors. The investigations of the effect of equilibration on the final contact angle reveal that for all substrates and temperatures lower final angles are recorded during experiments performed under equilibrated conditions. It is proposed that this is due to the need of longer times to eliminate all oxygen adsorbate from the Mo surface even under highly reducing conditions.

The decrease in the final angle with increasing temperature in case of liquid Ag on single-crystalline Mo substrates is due to an increase of solubility of Mo in the liquid Ag from 0.3 to 1.2 at.% with in the temperature range from 970 °C to 1290 °C. This results in a change of the interfacial energy $\Delta\gamma_{SL}$ of about 40 mN/m, which is sufficient to explain the difference in the final angle. However in case of liquid Ag on polycrystalline Mo substrates the strong decrease of the final angle at temperatures around (970 °C-1070 °C) is neither explained by changes of the interfacial energy γ_{SL} nor by changes of the surface energy γ_{LV} of the liquid Ag. It is conceivable that at the temperature of 970 °C oxygen on the polycrystalline Mo substrate, present prior to the experiment, might not be fully desorbed even under highly reducing conditions. This would lead to a decrease in γ_{SV} and a higher final angle.

The final contact angle for Ag on the Mo(100) single crystal for temperatures up to 1070 °C is always larger than the one observed for the Mo(110) surface. The experiments can be explained if they obey the relation $\Delta\gamma_{SL} = \gamma_{SL}^{100} - \gamma_{SL}^{110} > \Delta\gamma_{SV} = \gamma_{SV}^{100} - \gamma_{SV}^{110}$. This suggests that either γ_{SL} is different for the different Mo orientations or that under the experimental conditions the surface energy of Mo(110) has to be higher than the one from Mo(100). It is known that in the presence of hydrogen a reconstruction of the Mo surface occurs which results in a change of the surface energies. At the experimental temperatures one can expect fully reconstructed surfaces. Thus the Mo(100) surface might reduce its surface energy due to reconstruction below the Mo(110) surface energy explaining the experimental findings.

In order to investigate possible ridge formation, due to local atomic diffusion of atoms of the substrate at the triple line during the spreading process, grooving experiments of the polycrystalline Mo were performed and the surface diffusivities that will control ridge evolution were determined. Ridge formation can influence the spreading kinetics and was reported for several high-temperatures system such as glass on Mo and Al on Al_2O_3 {Saiz, E., 1998}, {Lopez-Esteban S., 2004}. In experiments of this work ridge formation at the fastest reported wetting velocities was not possible without initial perturbation for a ridge. If there was an initial perturbation, the ridge had to be smaller than 1nm in order to move with the liquid front. Therefore ridge formation does not influence the spreading kinetics in these experiments. SEM, AFM, and TEM investigations of the triple line showed that ridge formation does also not occur at the end of the wetting experiment when the drop is close to equilibrium and the wetting velocity is slow. The spreading was recorded for up to one hour.

8 Summary

9 Appendix

In this chapter the original data for the base radius of the liquid Ag drop in dependence of the time during the spreading experiment are presented (Figure 9.1-9.4). The Capillary numbers (Ca) shown in chapter 6 (Figures 6.4-6.7, 6.10A-B, 6.14-6.17) are determined with

$$Ca(t) = \eta [dR(t)/dt] \chi_{LV} \quad (9.1)$$

with R as the base radius of the drop, η the viscosity of the Ag and χ_{LV} the surface energy of Ag.

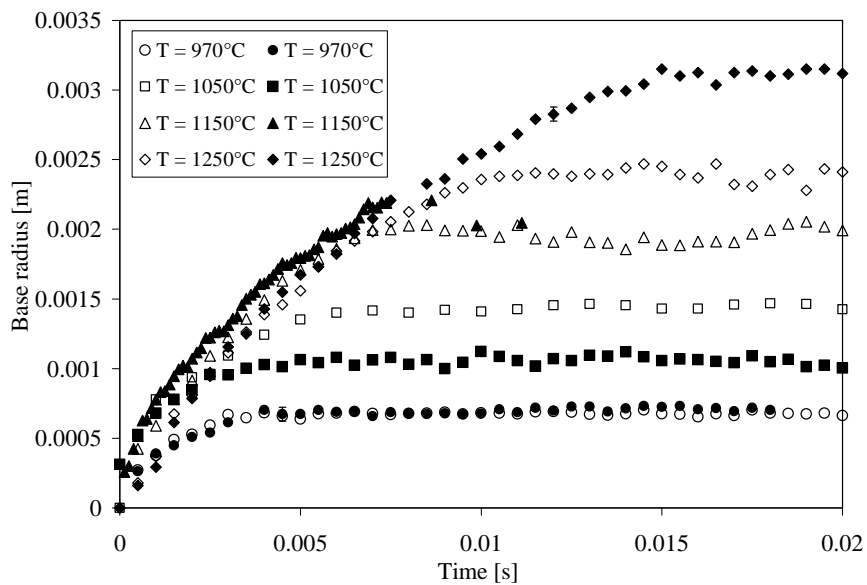


Figure 9.1: Presentation of the base radius of the liquid Ag versus time on polycrystalline Mo. The Capillary numbers in figures 6.4-6.7 are determined out of the derivation of these radii versus time data

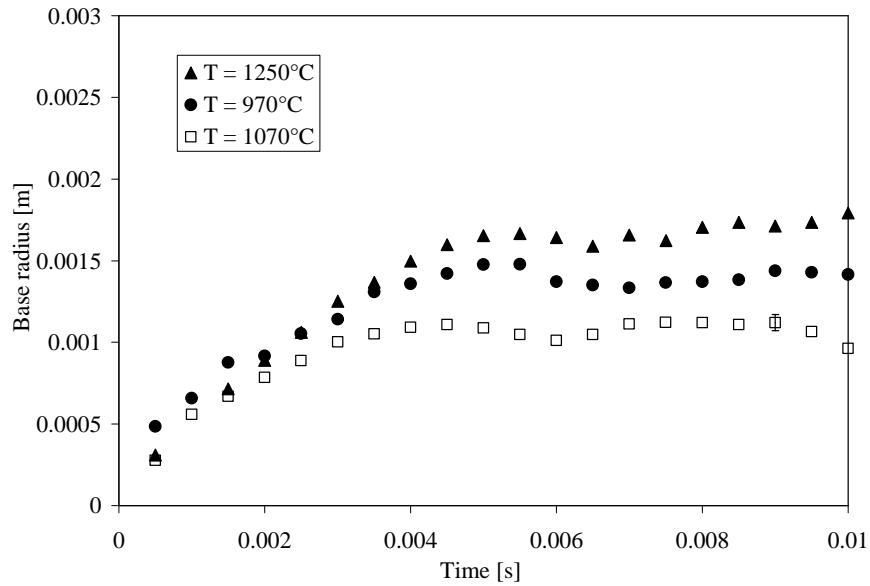


Figure 9.2: Dependency of the base radius of the liquid Ag versus time on Mo(110) is illustrated. Out of the derivation of these radii versus time the capillary numbers in figure 6.10A could be determined.

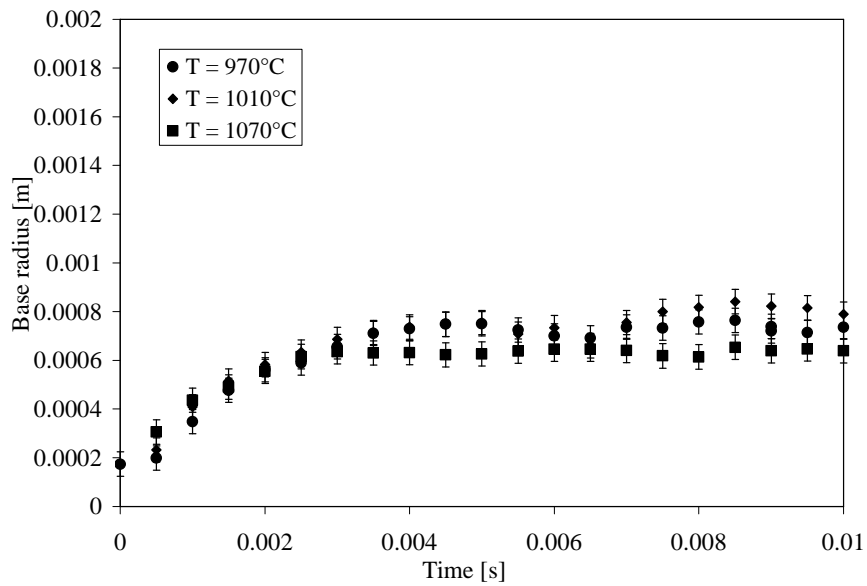


Figure 9.3: The base radius of the liquid Ag versus time on single crystalline Mo(100) is shown in this figure. The capillary numbers in figure 6.10B were determined out of the derivative of the radius regarding the time.

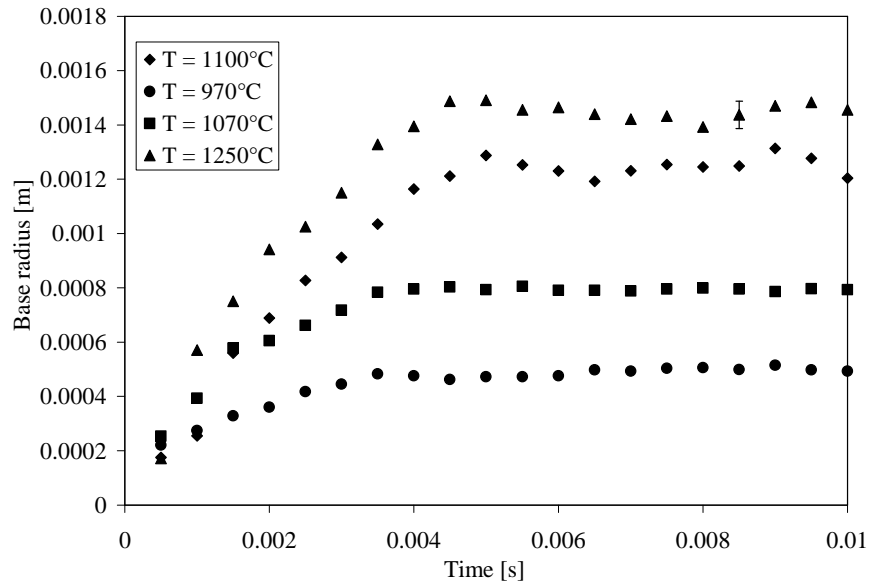


Figure 9.4: Presentation of the base radius of the liquid Ag versus time on polycrystalline Mo in case of the non-equilibration condition. The Capillary number for the non-equilibrated data in figures 6.14-6.17 are determined out of the derivation of these base radii versus time data

Bibliography

- {Allen, B.C., 1972} B.C. Allen, J. of the Less-Common metals, 1972, 29: 263
- {Antonov, V.E, 2004} V.E. Antonov, A.I. Latynin, M. Tkacz, J. Phys.: Condens. Matter, 2004, 16: 8387
- {Ausserré, D, 1986} D. Ausserré, A.M. Picard, L.Léger, Physical Review Letters, 1986, 57, [21]: 2671
- {Blake, T.D., 1993} J.C.Berg, Wettability, surface science series 1993, 49: 251
- {Blake, T.D., 1968} T.D. Blake, PhD-theses, University Bristol 1968
- {Borchard-Wyart, F., 1991} F. Borchard-Wyart, J.M. de Meglio, D. Quéré, P.G. de Gennes, Langmuir, 1991, 7: 335
- {Brandon D., Kaplan,W. 1999} D. Brandon and W.D. Kaplan, Microstructural Characterisation of Materials, Wiley, 1999
- {Burley, R. 1976, A} R. Burley and B.S. Kennedy, Brit. Polym., 1976, 8: 140
- {Burley, R. 1976, B} R. Burley and B.S. Kennedy, Chem. Eng. Sci., 1976 31: 901
- {Butt, H.J., 2003} Physics and chemistry of interfaces, Wiley-VHC Gmbh&Co.KGaA, 2003
- {Cannon, R.M., 1995} R.M. Cannon, E. Saiz, A.P. Tomsia, W.C. Carter, Mater. Res. Soc. Symp. Proc., 1995, 357: 279
- {Carnahan, R.D, 1958} R.D. Carnahan, T.L. Johnston, C.H. Li, J.Am. Ceram. Soc., 41: 343

Bibliography

- {Carré, A., 1995} A.Carré, M.E.R. Shanahan, Langmuir, 1995, 11: 3572
- {Carré, A., 1996} A. Carre, J.C. Gastel, M.E.R. Shanahan, Nature, 1996, 379: 432
- {Chatain, D, 1994} D , Chatain, F. Chabert, V. Ghetta, J. Am. Ceram. Soc., 1994, 77 [1]: 197
- {Che J.G., 1998} J.G. Che, C.T. Chan, W-E. Jian, T.C. Leung, Physical Review B, 1998, 57, [3]: 1875
- {Chen, J.D, 1987} J.D. Chen, Journal of Colloid Interface Science, 1988, 122, [1]: 60
- {Cox, R.G., 1986} R.G. Cox, J. Fluid. Mech., 1986, 168: 169
- {Davis, S.H., 1983} Davis, S.H., J.Appl. Mech., 1983, 50: 977
- {De Boer, J.H., 1953} J.H. de Boer, The dynamical Character of adsorption, Clarendon Press, Oxford, 1953
- {De Coninck, J. 2001} J. De Coninck, M.J.de Ruijter, M. Voué, Journal of Colloid and Interface Science, 2001, 2: 49
- {Derby B., 2001} B. Derby, J.R.P. Webster, Trans. JWRI, 2001, 30: 233
- {De Ruijter, M.1988} M. de Ruijter, T.D.Blake, A.Clarke, J. De Coninck, Journal of Petroleum Science and Engineering 1999, 24: 189
- {De Ruijter, M., 1998} M. de Ruijter, P. Kölsch, M.Voué, J. De Coninck, J.P. Rabe, Colloids and Surfaces A, 1998,144: 235
- {De Ruijter M.J.,2000} Michel J. De Ruijter, Magali Chalot, Michael Voué, Joël De Coninck, Langmuir 2000, 16: 2363
- {Dodge, FT. 1988} FT. Dodge, Journal of Colloid Interface Science, 1988, 121: 155
- {Douglas L.J., 1991} L.J. Douglas, S.F. Kistler, N.K. Nelson, IS&T 44th Annual Conference, St. Paul, MN, 1991

Bibliography

- {Ehrlich, G., 1980} G. Ehrlich, K. Stolt, *Ann. Rev. Phys. Chem.*, 1980
31: 603
- {Eick et al., 1975} J.D. Eick, R.J. Good, A.W. Neumann, *Journal of
Colloid and Interface Science*, 1975, 53, [2]: 235
- {Eustathopoulos N., 1998} N. Eustathopoulos, *Acta Mater.*, 1998, 46: 2319
- {Eustathopoulos, N., 1999} N. Eustathopoulos, M.G. Nicholas, B. Drevet,
Wettability at High Temperatures, Pergamon
Materials Series, Editor R.W. Cahn, 1999
- {Fermigier, M., 1988} M. Fermigier, P. Jenffer, *Ann Physique*, 1988, 13:
37
- {Fukai Y., 2003} Y. Fukai, M. Mizutani, *Mater. Trans.*, 2003, 44:
1359
- {Gennes de, P.G., 1985} P.G. de Gennes, *Reviews of Modern Physics*,
1985, (57), [3]: 827
- {Gibbs, W., 1928} W. Gibbs, *The collected works of J. Willard
Gibbs*, Yale University press, New Haven, 1928
- {Gjostein, 1963} N.A. Gjostein, *Metal surfaces*, 1963: 99
- {Glasstone, S., 1941} S. Glasstone, K.J. Laidler, H.J. Eyring, *The theory
of Rate Processes*, McGraw-Hill, New York 1941
- {Gremillard, L., 2004 A} Gremillard L., *DropAngle* software, Lawrence
Berkeley National Laboratory, USA
- {Gremillard L., 2004 B} L. Gremillard, E. Saiz, J. Chevalier, A.P. Tomsia,
Zeitschrift für Metallkunde 2004, 95, [4]: 261
- {Guttoff, E.G., 1982} E.B. Guttoff, C.E. Kendrick, *AIChE J.*, 1982, 28:
459
- {Hansen, R.J., 1971} R.J. Hansen, T.Y. Toong, *Journal of Colloid
Interface Science*, 1971, 37: 196
- {Heimendahl, M., 1970} M. Heimendahl, *Einführung in die
Elektronenmikroskopie* Viehweg-Verlag,
Braunschweig, 1970

Bibliography

- {Hocking, L.M., 1982} L.M. Hocking, A.D. Rivers, *Journal of Fluid Mech.*, 1982, 121: 425
- {Hoffmann, R.L., 1975} R.L. Hoffmann, *J. Coll. Inter. Sci.* 1975,50: 228
- {Huh, C., 1971} C. Huh, L.E. Scriven, *Journal of Colloid Interface Science*, 1971, 35: 85
- {Johnson, R.E., 1993} J.C. Berg, *Wettability, surface science series*, 1993,49: 2
- {Keene, B.J., 1993} B.J. Keene, *International Materials Reviews*, 1993, 38, [2] :157
- {Kistler, S.F. 1993} S.F. Kistler, *Wettability, surface science series*, 1993,49: 311
- {Levi G., 2003} G. Levi, W.D. Kaplan, *Acta Materialia* 2003, 51: 2793
- {Loehman, R.E., 1994} R.E. Loehman, A.P. Tomsia, *J. Amer. Ceram. Soc.*, 1994, 77:271
- {Lopez-Esteban S., 2004} to be published in *Langmuir*
- {Marmur, A., 1983} A. Marmur, *Advanced Colloid Interface Science*, 1983, 19: 75
- {Massalski, T.B., 1990} T.B. Massalski (Editor in Chief): *Binary Alloy Phase Diagrams*, ASM International, Materials Park, Ohio, 1990
- {Mullins, W.W., 1956} W.W. Mullins, *Journal of applied physics*, 1956, 28, [3]: 333
- {Naidich, Y., 1972} Y.V. Naidich, V. Perevertailo, G. Nevodnik, *Poroshkovaya Metallurgiya*, 1972, 7:51
- {Naidich, Y., 1981} Y.V. Naidich, N.F. Grigorenko, V.M. Perevertailo, *J. of Crystal Growth*, 1981,53: 261
- {Naidich, Y., 1992} Y.V. Naidich, W. Sabuga, V. Perevertailo, *Adgeziya Raspl. Pajka Mater.*, 1992, 27:23

Bibliography

- {Neumann, A.W., 1971} A.W. Neumann, R.J. Good, *Journal of Colloid and Interface Science*, 1971, 38, [2]: 341
- {Ngan, C.G.,1982} C.G. Ngan, E.B. Dussan V, *J. Fluid Mech.*, 1982 118: 27
- {Pique D, 1981} D. Pique, R. Sangiori, N. Eustathopoulos, *Ann. Chim. (Sci. Mater.)*, 1981, 6: 443
- {Prybyla, J.A., 1991} J.A. Prybyla, P.J. Estrup, Y.J. Chabal, *J. Chem. Phys.* 94 (9), 1991, 6274
- {Richter, G., 2000} G. Richter, PhD thesis, Univesität Stuttgart, Stuttgart 2000
- {Saiz, E., 2000} E. Saiz, R.M. Cannon, A.P. Tomsia, *Acta materialia*, 2000, 48: 4449
- {Saiz, E 1998} E. Saiz, A.P. Tomsia, R.M. Canon, *Acta mater*, 1998, 46 [7]: 2349
- {Saiz, E., 2001,A} E.Saiz, R.M. Cannon, A.P.Tomsia, *Oil Gas Sci. Technol.* 2001, 56: 89
- {Saiz, E., 2001} E. Saiz, A.P. Tomsia, R.M. Cannon, *Scripta.mater*, 2001, 44: 159
- {Saiz E., 2003} E Saiz, C.-W. Hwang, K. Suganuma, A.P Tomsia, *Acta Materialia*, 2003, 51: 3185
- {Schmidt P.F, 1994} P.F. Schmidt et al., *Praxis der Rasterelektronenmikroskopie und Mikrobereichsanalyse*, Expert Verlag, 1994
- {Schneemilch, M., 1998} M. Schneemilch, R.A. Hayes, J.G. Petrov, J. Ralston, *Langmuir*, 1998, 14: 7047
- {Schöllhammer J.,1998} Jochen Schöllhammer, Diplomarbeit ,Institut für Metallkunde, Universität Stuttgart, 1998
- {Seah, M.P., 1988} M.P. Seah and D. Briggs, *Practical Surface Analysis*, JohnWiley&Sons Ltd, Chichester, 1988

Bibliography

- {Seebauer E.G, 1995} E.G. Seebauer , C.E. Allen, Progress in Surface science, 1995, 49,3)
- {Shanahan, M., 1988} M. Shanahan, J. Phys. D: Appl. Phys., 1988, 21:981
- {Sharps, P.R., 1981} P.R. Sharps, A.P. Tomsia, J.A. Pask, Acta Metall., 1981, 29: 855
- {Smithells, C.J., 1976} C.J. Smithells, E.A. Brandes, Metal Reference Book, Butterworth, London, Boston, 1976
- {Ström, G., 1990} G. Ström, M. Fredriksson, P.Stenius, P. Radoev, J. Coll. Inter. Sci., 1990, 134: 107
- {Staumal, B., 2005} B. Staumal, private communication, 2005
- {Sugita, T., 1970} T. Sugita, S. Ebsiawa, K. Kawasaki, Surface Science 1970, 20: 417
- {Tanner, L.H., 1979} Tanner, L.H., J.Phys. D:Appl. Phys, 1979, 12: 1473
- {TMX 2000, Users Manual} TMX 2000, Users Manual, Version 3.04, Topomatrix
- {Tomsia, A.P.,1982} A.P. Tomsia, Z.Feipeng, Pask J.A., Act Metall, 1982, 30: 1203
- {Voinov, O.V., 1976} O.V. Voinov, Izv. Akad. Nauk SSSR Mekh. Zhidk. Gaza (USSR), 1976:76
- {Wilhelmy L., 1863} Wilhelmy L., Annalen der Physik und Chemie, 1863,119: 177
- {Williams D., Carter, C. 1996} D.B. Williams and C.B. Carter, Transmission Electron Microscopy, Plenum Press, New York, 1996
- {Wiesendanger, R., 1994} Wiesendanger, R, Scanning Probe Microscopy and Spectroscopy: Metods and Applications, Cambridge University Press ,1994

Bibliography

- {Yeh, E.K., 1999} E.K. Yeh, J. Newman, C.J. Radke,
Colloids&Surfaces A 1999, 156: 525
- {Young, T., 1805} T. Young, Phil. Trans., 1805, 95: 65
- {Yupko, V.L., 1991} V.L. Yupko, V.V. Garbuz, N.I. Kryuchkova,
1991, 10: 72
- {Yupko, V.L., 1986} V.L. Yupko, G.V. Levchenko, R.B. Luban,
R.I.Kryhanovskaya, Translated from
Poroshkovaya Metallurgiya 1986, 287, [11]: 64

Acknowledgement

- I gratefully thank Prof. Dr. Dr. h. c. M. Rühle for giving me the opportunity to work in his department and for his constant support and interest in the forthcoming of this thesis.
- A special thanks to Prof. Dr. A.P. Tomsia for his great help and support during the time of performing the wetting experiments at LBNL in Berkeley and also throughout the rest of my PhD-time.
- Thanks to Prof. Dr. F. Aldinger for taking over the Mitbericht.
- I specially acknowledge my supervisors Dr. Eduardo Saiz, Dr. Christina Scheu and Dr. Wilfried Sigle for their continuous guidance and support throughout the project, many fruitful scientific discussions and their patience with me and of proofreading the manuscript.
- I thank Dr. Laurent Gremillard, Dr. Peter Nalbach, Dr. Rowland Cannon, and Dr. Gunther Richter for all the scientific discussions.
- Thanks to : Ulrike Täffner, and Margit Kapp for their great help in polishing the Mo substrates, Ute Salzberger for her patience and help to prepare the TEM specimens, Albrecht Meyer for performing the ICP investigations, Sabine Kühnemann for the SEM investigations, Thomas Meisner for his help in performing the annealing experiments as well as Peter Kopold, Steffen Schmidt and Gunther Richter for their help during the TEM experiments, Birgit Heiland for performing the FIB experiments, Bernhard Siegle for the Auger measurements, Ulrike Täffner for helping me in doing the AFM investigations and Rolf Henes for cutting the Mo single crystals.

Acknowledgement

- Dr. Eduardo Saiz is acknowledged for performing the Mo (100) single crystal experiments at LBNL in Berkeley.
- Thanks to all the colleagues here in Stuttgart and as well in Berkeley especially to Dr. Elena Tchernychova, and Guillermo Menendez, Dr. Sonia Lopez-Esteban, Dr. Laurent Gremillard for the excellent working conditions.
- Thanks also to my friend Dr. Pravesh Patel for correcting my English.
- I would like to especially thank my family and my husband Peter Nalbach for their strong support.
- Last a special thanks to my friend Alexandra Naumann for her continuous encouragement and kind words during the last past three years.

Curriculum vitae

Name	:	Nicole Rauch
Date of birth	:	19.03.1972
Place of birth	:	Saarbrücken
Nationality	:	german
Marital status	:	married
1978-1982	:	Grundschule Bruchwiese Saarbrücken
1982-1988	:	Realgymnasium Sulzbach
1988-1991	:	Wirtschaftsgymnasium Saarbrücken
1991-1999	:	Study of Material Science at the Universität Saarbrücken
1997-1999	:	Diplomarbeit in the group of Prof. Dr. Breme with the Title : “Dispersionhardening of copper”
1999	:	Diploma (Dipl. Ing.)
2000-2001	:	Trainee for R&D (Saarstahl AG, Völklingen)
2001-2003	:	Research in material science at Lawrence Berkeley National Laboratory (LBNL), Berkeley, CA, USA
2003-2005	:	PhD student at the Max–Planck–Institut für Metallforschung in Stuttgart in the group of Pro. Dr. Dr. h.c. M. Rühle